

IMAGE RECONSTRUCTION METHOD TO SEPARATE SIMULTANEOUS
ENCODED SLICES WITH IN-PLANE AND THROUGH-PLANE
ACCELERATION IN FMRI

by

Ke Xu, M.S.

A Dissertation submitted to the faculty of the Graduate School,
Marquette University,
in Partial Fulfillment of the Requirements for
the Degree of Doctor of Philosophy

Milwaukee, Wisconsin

May 2025

ABSTRACT
IMAGE RECONSTRUCTION METHOD TO SEPARATE SIMULTANEOUS
ENCODED SLICES WITH IN-PLANE AND THROUGH-PLANE
ACCELERATION IN FMRI

Ke Xu, M.S.

Marquette University, 2025

FMRI has been a safe medical imaging tool to study brain function by observing the spatial and temporal changes in brain metabolism in recent decades. To capture brain functionality more efficiently, efforts have been made to accelerate the number of images acquired per unit of time that create each volume image, without losing full anatomical structure. The Simultaneous Multi-Slice (SMS) technique provides a reconstruction method where multiple slices are aliased and acquired concurrently. The Through-Plane Acceleration (TPA) method is one of the SMS techniques that can reduce data acquisition time in proportion to the number of aliased images acquired per unit of time. Other image acquisition acceleration techniques, such as the In-Plane Acceleration (IPA) method, focus on reducing the total image scan time by skipping partial lines in the frequency domain (k -space), resulting in a “fold-up” artifact after inverse Fourier transform. To un-alias and un-fold the acquired images, the Sensitivity Encoding (SENSE) and the GeneRalized Autocalibrating Partial Parallel Acquisition (GRAPPA) techniques can be utilized but still have their drawbacks. Due to the short physical distance and high similarity in coil sensitivity information between the aliased voxels, a singular matrix problem arises in the design matrix, and the influence of the geometry factor (g -factor) increases. To manually increase the distance and the difference in coil sensitivity information between the aliased images, the Controlled Aliasing in Parallel Imaging (CAIPI) and view angle tilting (VAT) techniques achieve slice-wise image shift by applying different radiofrequency pulse sequences. In this dissertation, multi-direction image shift techniques are incorporated with the multi-coil separation of parallel encoded complex-valued slices (mSPECS) technique in a Bayesian approach. The TPA and IPA techniques are integrated with Hadamard phase encoding and a novel 2D Hadamard phase encoding technique. A bootstrapping technique and an artificial aliasing of calibration images are applied to enhance the condition of the design matrix. Through the investigation of the novel SMS techniques on both simulation and experimental fMRI dataset, our model significantly reduces total image scan time while preserving and detecting task signal effectively.

ACKNOWLEDGMENT

Ke Xu, M.S.

I would like to express my deepest appreciation to my advisor, Dr. Daniel B. Rowe, for being an exceptional mentor. Your guidance and expertise have provided me with invaluable knowledge and resources that will greatly benefit my future academic career. More importantly, you have shown me what exemplary research looks like—emphasizing lifelong learning, maintaining passion for new knowledge, and continuously sharing ideas with others. The invaluable lessons I have learned from you will remain fundamental to my growth as a researcher, and for that, I am profoundly grateful.

I would like to express my sincere appreciation to Dr. Andrew S. Nencka for his guidance and invaluable mentorship, which have provided me with a profound learning experience and introduced me to the field of fMRI research, where I have discovered my true passion. I am also deeply grateful to Dr. Neveen Bansal, who was my mentor during my master's degree, as well as to my committee member, Dr. Cheng-Han Yu, for their continued support and encouragement, which have always inspired me to pursue my academic aspirations.

I would like to thank my parents for their endless support and understanding. I am also deeply grateful to my lab partners, Dr. Chase J. Sakitis and John Bodenschatz, for their unwavering support and collaboration. Additionally, I would like to extend my heartfelt gratitude to all the professors and faculty in the Computational Mathematical and Statistical Sciences Department for their invaluable guidance and assistance, which have made my experience studying abroad much smoother and more fulfilling.

TABLE OF CONTENTS

LIST OF TABLES	v
LIST OF FIGURES	vi
CHAPTER 1: INTRODUCTION	1
1.1 FMRI Background	1
1.2 Image Shift Techniques	5
1.3 Complex-valued Bayesian Model	6
CHAPTER 2: A BAYESIAN APPROACH OF MSPECS-CAIPIVAT	10
2.1 The Data Acquiring Process in mSPECS-CAIPIVAT	10
2.1.1 Image Shift Techniques in mSPECS-CAIPIVAT	10
2.1.2 The Hadamard Phase Encoding	14
2.1.3 A Single Aliased Voxel	16
2.2 The Bootstrap Sampling and Artificial Aliasing of Calibration Images	20
2.3 The Prior Distribution	22
2.4 The Hyperparameters Assessment	23
2.5 The Posterior Estimation	24
CHAPTER 3: A BAYESIAN APPROACH OF MSPECS-IPA-CAIPIVAT	26
3.1 The Data Acquiring Process in mSPECS-IPA-CAIPIVAT	26
3.1.1 Image Shift Techniques in mSPECS-IPA-CAIPIVAT	26
3.1.2 The 2D Hadamard Phase Encoding	27
3.1.3 The Combination of Image Shift Techniques and 2D Hadamard Phase Encoding	29
3.1.4 A Single Aliased Voxel	32
3.2 The Bootstrap Sampling and Artificial Aliasing of Calibration Images	35

3.3	The Likelihood, Prior, and Joint Distribution	38
3.4	The Hyperparameters Assessment	39
3.5	The Posterior Estimation	40
CHAPTER 4: A GRAPPA APPROACH OF MSPECS-IPA-CAIPIVAT		43
4.1	The GRAPPA Technique	43
4.2	The GRAPPA Approach for mSPECS-IPA-CAIPIVAT	46
CHAPTER 5: SIMULATED RECONSTRUCTION RESULTS		48
5.1	Simulated FMRI Data	48
5.2	mSPECS-CAIPIVAT	50
5.2.1	Non-Task Simulated Reconstruction Results	50
5.2.2	Task Simulated Reconstruction Results	61
5.3	mSPECS-IPA-CAIPIVAT	67
5.3.1	Non-Task Simulated Reconstruction Results	67
5.3.2	Task Simulated Reconstruction Results	76
5.4	GRAPPA Approach for mSPECS-IPA-CAIPIVAT	80
5.4.1	Non-Task Simulated Reconstruction Results	80
5.4.2	Task Simulated Reconstruction Results	87
CHAPTER 6: EXPERIMENTAL RECONSTRUCTION RESULTS		92
6.1	Experimental FMRI Data	92
6.2	mSPECS-CAIPIVAT	93
6.2.1	Non-Task Experimental Reconstruction Results	93
6.2.2	Task Experimental Reconstruction Results	97
6.3	mSPECS-IPA-CAIPIVAT	101
6.3.1	Non-Task Experimental Reconstruction Results	101
6.3.2	Task Experimental Reconstruction Results	107
6.4	GRAPPA Approach for mSPECS-IPA-CAIPIVAT	112

6.4.1	Non-Task Experimental Reconstruction Results	112
6.4.2	Task Experimental Reconstruction Results	117
CHAPTER 7: DISCUSSION		123
7.1	mSPECS-CAIPIVAT	123
7.2	mSPECS-IPA-CAIPIVAT	125
7.3	The GRAPPA Approach for mSPECS-IPA-CAIPIVAT	128
7.4	Future Work	129
BIBLIOGRAPHY		131

LIST OF TABLES

- | | | |
|---|--------------------------------------------------------------------------------------------------------------------------------------------------------------------------------------------------------------------------------------------------------------------------------------------------------------------------------------------------------------------------------------------------------|----|
| 1 | <p>The comparison of total scan time among the mSPECS-CAIPIVAT, mSPECS-IPA-CAIPIVAT, and GRAPPA for mSPECS-IPA-CAIPIVAT approaches is presented with respect to different acceleration factors. Note that $TPA = 1$ represents the non-accelerated case.</p> | 51 |
| 2 | <p>The average SNR value for cerebrospinal fluid (CSF), gray matter (GM), and white matter (WM) with the average g-factor value of the whole brain with respect to SENSE, mSPECS, mSPECS-VAT, mSPECS-CAIPIRINHA, and mSPECS-CAIPIVAT methods with through-plane acceleration factors $TPA=2$, $TPA=4$, and $TPA=8$ for slice 3.</p> | 60 |

LIST OF FIGURES

1.1	A. The subsampled spatial frequency domain incorporated with IPA approach and the acceleration factor equal to 2. B. The acquired subsampled k -space acquired from four receiver coils.	3
1.2	The 3D view (left) and 2D view (right) of an example for SMS technique with four slices and four coils.	4
1.3	Top row: the image shift process corresponding to the CAIPIRINHA technique (shifted vertically). Middle row: the image shift process corresponding to the VAT technique (shifted horizontally). Bottom row: the image shift process corresponding to the CAIPIVAT technique (shifted vertically and horizontally).	7
2.1	A. An example of in-excitation and through-excitation image shift process with $N_s = 4$ by applying the CAIPIRINHA technique. B. An example of in-excitation and through-excitation image shift process with $N_s = 4$ by applying the VAT technique. C. An example of in-excitation and through-excitation image shift process with $N_s = 4$ by applying the CAIPIVAT technique.	13
2.2	An illustration of Hadamard phase-encoding aliasing pattern when $N_s = 4$. A. shows the H_4 matrix with plus sign denotes as 1 and minus sign demotes as -1. B. shows sequential Hadamard aliasing coefficient for each slice in the fMRI time series. C. shows the phantom brain images are multiplied by the Hadamard aliasing coefficients at the first 4 TRs.	16

2.3	The data-acquiring process of the mSPECS technique (without any image shifts), the mSPECS-CAIPIRINHA technique (shift vertically), the mSPECS-VAT technique (shift horizontally), and the mSPECS-CAIPIVAT technique (shift vertically and horizontally).	19
3.1	A. The 2D Hadamard phase encoding coefficient for $N_s = 2$. B. The 2D Hadamard phase encoding coefficient for $N_s = 4$	29
3.2	The voxel aliasing situation for the first 4 TRs with $N_s = 4$ circumstance incorporating with A. mSPECS-IPA image shift technique, B. mSPECS-IPA-CAIPIRINHA technique, C. mSPECS-IPA-VAT technique, and D. mSPECS-IPA-CAIPIVAT technique.	31
3.3	The voxel aliasing situation with $N_s = 4$ for mSPECS-IPA, mSPECS-IPA-CAIPIRINHA, mSPECS-IPA-VAT and mSPECS-IPA-CAIPIVAT technique.	32
3.4	The the 2D Hadamard aliasing coefficients for acquired aliased slices (red box) and the artificial aliased calibration slices (blue box) for the first 4 TRs with $N_s = 4$	37
4.1	The linear combination of the acquired data in the neighborhood of kernel size equal to 2×3 with in-plane acceleration of $IPA = 2$. The black dots are acquired data, white dots are missing data, and the red dot is the known data from the calibration images.	45
4.2	The flowchart of the GRAPPA approach of the mSPECS-IPA-CAIPIVAT model.	47
5.1	A. The magnitude and phase for the true noiseless simulated axial brain images with $N_s = 8$. B. The magnitude of the simulated sensitivity coils for slice 3 with $N_c = 8$	49

5.2	The true noiseless simulated magnitude of the axial brain images compared with the temporal mean magnitude and temporal mean phase from SENSE, mSPECS, mSPECS-VAT, mSPECS-CAIPIRINHA and mSPECS-CAIPIVAT model for odd slices with TPA=2.	52
5.3	The true noiseless simulated phase of the axial brain images compared with the temporal mean magnitude and temporal mean phase from SENSE, mSPECS, mSPECS-VAT, mSPECS-CAIPIRINHA and mSPECS-CAIPIVAT model for odd slices with TPA=2.	53
5.4	The temporal mean of baseline signal variance of the voxel value for slice 3 from SENSE, mSPECS, mSPECS-VAT, mSPECS-CAIPIRINHA, and the mSPECS-CAIPIVAT model with TPA=2, TPA=4, and TPA=8.	54
5.5	The temporal variance of the task signal of SENSE, mSPECS, mSPECS-VAT, mSPECS-CAIPIRINHA, and mSPECS-CAIPIVAT model with different acceleration factors of slice 3.	55
5.6	The temporal mean of the residual variance for slice 3 from SENSE, mSPECS, mSPECS-CAIPIRINHA, mSPECS-VAT, and mSPECS-CAIPIVAT model with TPA=2.	56
5.7	The temporal mean of the residual variance for slice 3 from SENSE, mSPECS, mSPECS-CAIPIRINHA, mSPECS-VAT, and mSPECS-CAIPIVAT model with acceleration factor TPA=4 and TPA=8.	57
5.8	The Temporal variance of the residual variance for slice 3 from SENSE, mSPECS, mSPECS-CAIPIRINHA, mSPECS-VAT, and mSPECS-CAIPIVAT model with TPA=2.	58
5.9	The Temporal variance of the residual variance for slice 3 from SENSE, mSPECS, mSPECS-CAIPIRINHA, mSPECS-VAT, and mSPECS-CAIPIVAT model with TPA=4 and TPA=8.	59

5.10	A. The <i>SNR</i> maps for SENSE, mSPECS, mSPECS-VAT, mSPECS-CAIPIRINHA and mSPECS-CAIPIVAT model with TPA=2, TPA=4, and TPA=8. The higher <i>SNR</i> , the better model performs. B. The <i>g</i> -factor maps for SENSE, mSPECS, mSPECS-VAT, mSPECS-CAIPIRINHA and mSPECS-CAIPIVAT model with TPA=2, TPA=4, and TPA=8. The closer <i>g</i> -factor is to 1, the better model performs.	62
5.11	The <i>CNR</i> map and the average <i>CNR</i> value and standard deviation of <i>CNR</i> of ROI for SENSE, mSPECS, mSPECS-VAT, mSPECS-CAIPIRINHA and mSPECS-CAIPIVAT model for odd slices with TPA=2.	64
5.12	A. The <i>CNR</i> maps and average ROI <i>CNR</i> value from SENSE, mSPECS, mSPECS-VAT, mSPECS-CAIPIRINHA and mSPECS-CAIPIVAT model with respect to different acceleration factors TPA=2, TPA=4, and TPA=8 for slice 3. B. The task activation detection maps and average ROI z-score from SENSE, mSPECS, mSPECS-CAIPIRINHA and mSPECS-CAIPIVAT model with respect to acceleration factor TPA=2, TPA=4 and TPA=8 for slice 3. The higher <i>CNR</i> and z-score, the better model performs.	65
5.13	The activation detection map and the average and standard deviation of z-score of ROI for SENSE, mSPECS, mSPECS-VAT, mSPECS-CAIPIRINHA and mSPECS-CAIPIVAT model for odd slices with TPA=2 situation.	66
5.14	The magnitude of the reconstructed images from mSPECS-IPA, mSPECS-IPA-CAIPIRINHA, mSPECS-IPA-VAT, and mSPECS-IPA-CAIPIVAT, compared with the magnitude and phase from true noiseless simulated images with TPA=2.	68

5.15	The phase of the reconstructed images from mSPECS-IPA, mSPECS-IPA-CAIPIRINHA, mSPECS-IPA-VAT, and mSPECS-IPA-CAIPIVAT, compared with the magnitude and phase from true noiseless simulated images odd slices with TPA=2.	69
5.16	The variance of the baseline regression coefficient of slice 3 from reconstructed images from mSPECS-IPA, mSPECS-IPA-CAIPIRINHA, mSPECS-IPA-VAT, and mSPECS-IPA-CAIPIVAT model with different through-plane acceleration factors. The top right corner is the slices aliasing situation for slice 3 with different acceleration factors.	70
5.17	The task regression coefficient variance of slices 3 from reconstructed images from mSPECS-IPA, mSPECS-IPA-CAIPIRINHA, mSPECS-IPA-VAT, and mSPECS-IPA-CAIPIVAT model with different through-plane acceleration factors. The top right corner is the slices aliasing situation for slice 3 with different acceleration factors.	71
5.18	The temporal mean of residual variance of brain images reconstructed from mSPECS-IPA, mSPECS-IPA-CAIPIRINHA, mSPECS-IPA-VAT and mSPECS-IPA-CAIPIVAT model with IPA = 2 and TPA = 2.	72
5.19	The temporal mean of residual variance of brain images reconstructed from mSPECS-IPA, mSPECS-IPA-CAIPIRINHA, mSPECS-IPA-VAT and mSPECS-IPA-CAIPIVAT model with IPA = 2 and TPA = 4 and 8.	73
5.20	The variance of the baseline regression coefficient of slice 3 from reconstructed images from mSPECS-IPA, mSPECS-IPA-CAIPIRINHA, mSPECS-IPA-VAT, and mSPECS-IPA-CAIPIVAT model with different through-plane acceleration factors.	74

5.21	The variance of the baseline regression coefficient of slice 3 from reconstructed images from mSPECS-IPA, mSPECS-IPA-CAIPIRINHA, mSPECS-IPA-VAT, and mSPECS-IPA-CAIPIVAT model with different through-plane acceleration factors.	74
5.22	A. The <i>SNR</i> value of slice 3 from reconstructed images for mSPECS-IPA, mSPECS-IPA-CAIPIRINHA, mSPECS-IPA-VAT, and mSPECS-IPA-CAIPIVAT model with different TPA factor. B. The <i>g</i> -factor value of slice 3 from reconstructed images for mSPECS-IPA, mSPECS-IPA-CAIPIRINHA, mSPECS-IPA-VAT, and mSPECS-IPA-CAIPIVAT model with different TPA factor.	75
5.23	The average <i>CNR</i> value of ROI for with acceleration factor TPA=2 from mSPECS-IPA, mSPECS-IPA-CAIPIRINHA, mSPECS-IPA-VAT, and mSPECS-IPA-CAIPIVAT model.	78
5.24	The average task activation rate (z-score) of ROI for with acceleration factor TPA=2 from mSPECS-IPA, mSPECS-IPA-CAIPIRINHA, mSPECS-IPA-VAT, and mSPECS-IPA-CAIPIVAT model.	79
5.25	A. The average <i>CNR</i> value of ROI for slice 3 from mSPECS-IPA, mSPECS-IPA-CAIPIRINHA, mSPECS-IPA-VAT, and mSPECS-IPA-CAIPIVAT model with acceleration factor TPA=2, TPA=4, and TPA=8. B. The average activation detection rate (z-score) of ROI for slice 3 from mSPECS-IPA, mSPECS-IPA-CAIPIRINHA, mSPECS-IPA-VAT, and mSPECS-IPA-CAIPIVAT model with acceleration factor TPA=2, TPA=4, and TPA=8.	81

5.26	The magnitude of the reconstructed images from GRAPPA approach for mSPECS-IPA, GRAPPA approach for mSPECS-IPA-CAIPIRINHA, GRAPPA approach for mSPECS-IPA-VAT, and GRAPPA approach for mSPECS-IPA-CAIPIVAT, compared with the magnitude from true noiseless simulated images with TPA=2.	82
5.27	The phase of the reconstructed images from GRAPPA approach for mSPECS-IPA, GRAPPA approach for mSPECS-IPA-CAIPIRINHA, GRAPPA approach for mSPECS-IPA-VAT, and GRAPPA approach for mSPECS-IPA-CAIPIVAT, compared with the phase from true noiseless simulated images with TPA=2.	83
5.28	The task regression coefficient variance of slices 3 from reconstructed images from GRAPPA for mSPECS-IPA, GRAPPA for mSPECS-IPA-CAIPIRINHA, GRAPPA for mSPECS-IPA-VAT, and GRAPPA for mSPECS-IPA-CAIPIVAT model with different through-plane acceleration factors.	84
5.29	A. The <i>SNR</i> value of slice 3 from reconstructed images for GRAPPA for mSPECS-IPA, GRAPPA for mSPECS-IPA-CAIPIRINHA, GRAPPA for mSPECS-IPA-VAT, and GRAPPA for mSPECS-IPA-CAIPIVAT model with different TPA factor. B. The <i>g</i> -factor value of slice 3 from reconstructed images for GRAPPA for mSPECS-IPA, GRAPPA for mSPECS-IPA-CAIPIRINHA, GRAPPA for mSPECS-IPA-VAT, and GRAPPA for mSPECS-IPA-CAIPIVAT model with different TPA factor.	85
5.30	The average <i>CNR</i> value of ROI for with acceleration factor TPA=2 situation from GRAPPA for mSPECS-IPA, GRAPPA for mSPECS-IPA-CAIPIRINHA, GRAPPA for mSPECS-IPA-VAT, and GRAPPA for mSPECS-IPA-CAIPIVAT model.	89

5.31	The average task activation rate (z-score) of ROI for with acceleration factor $TPA=2$ from GRAPPA for mSPECS-IPA, GRAPPA for mSPECS-IPA-CAIPIRINHA, GRAPPA for mSPECS-IPA-VAT, and GRAPPA for mSPECS-IPA-CAIPIVAT model.	90
5.32	A. The average <i>CNR</i> value of ROI for slice 3 from GRAPPA for mSPECS-IPA, GRAPPA for mSPECS-IPA-CAIPIRINHA, GRAPPA for mSPECS-IPA-VAT, and GRAPPA for mSPECS-IPA-CAIPIVAT model with acceleration factor $TPA = 2$, $TPA = 4$, and $TPA = 8$. B. The average activation detection rate (z-score) of ROI for slice 3 from GRAPPA for mSPECS-IPA, GRAPPA for mSPECS-IPA-CAIPIRINHA, GRAPPA for mSPECS-IPA-VAT, and GRAPPA for mSPECS-IPA-CAIPIVAT model with acceleration factor $TPA = 2$, $TPA = 4$, and $TPA = 8$	91
6.1	The temporal mean magnitude of the axial brain images from the reference, SENSE, mSPECS, mSPECS-VAT, mSPECS-CAIPIRINHA, and mSPECS-CAIPIVAT with acceleration factor $TPA=2$	94
6.2	The temporal mean phase of the axial brain images from the reference, SENSE, mSPECS, mSPECS-VAT, mSPECS-CAIPIRINHA, and mSPECS-CAIPIVAT with acceleration factor $TPA=2$	95
6.3	The temporal variance of SENSE, mSPECS, mSPECS-VAT, mSPECS-CAIPIRINHA, and mSEPCS-CAIPIVAT model with different acceleration factors of slice 3.	96
6.4	A. The <i>SNR</i> maps for SENSE, mSPECS, mSPECS-VAT, mSPECS-CAIPIRINHA and mSPECS-CAIPIVAT model with $TPA=2$, $TPA=4$, and $TPA=8$. B. The <i>g</i> -factor maps for SENSE, mSPECS, mSPECS-VAT, mSPECS-CAIPIRINHA and mSPECS-CAIPIVAT model with $TPA=2$, $TPA=4$, and $TPA=8$	98

6.5	The <i>CNR</i> map and the average <i>CNR</i> value and standard deviation of <i>CNR</i> of ROI for SENSE, mSPECS, mSPECS-CAIPIRINHA and mSPECS-CAIPIVAT model with TPA=2.	99
6.6	The activation detection map and the average and standard deviation of z-score of ROI for SENSE, mSPECS, mSPECS-CAIPIRINHA and mSPECS-CAIPIVAT model with TPA=2.	100
6.7	A. The <i>CNR</i> maps and average ROI <i>CNR</i> value from SENSE, mSPECS, mSPECS-VAT, mSPECS-CAIPIRINHA and mSPECS-CAIPIVAT model with respect to different acceleration factors TPA=2, TPA=4, and TPA=8 for slice 3. B. The task activation detection maps and the average ROI z-score from SENSE, mSPECS, mSPECS-VAT, mSPECS-CAIPIRINHA and mSPECS-CAIPIVAT model with respect to acceleration factor TPA=2, TPA=4 and TPA=8 for slice 3. The higher <i>CNR</i> and z-score, the better model performs.	102
6.8	The mean magnitude from reconstructed image with through-plane acceleration factor TPA=2 corresponding to mSPECS-IPA, mSPECS-IPA-CAIPIRINHA, mSPECS-IPA-VAT and mSPECS-IPA-CAIPIVAT model.	104
6.9	The mean phase from reconstructed image with through-plane acceleration factor TPA=2 corresponding to mSPECS-IPA, mSPECS-IPA-CAIPIRINHA, mSPECS-IPA-VAT and mSPECS-IPA-CAIPIVAT model.	105
6.10	The temporal variance of reconstructed image for slice 3 from mSPECS-IPA, mSPECS-IPA-CAIPIRINHA, mSPECS-IPA-VAT and mSPECS-IPA-CAIPIVAT model with different acceleration factor TPA=2, TPA=4, and TPA=8.	106

6.11	A. The SNR value of reconstructed brain images slice 3 from mSPECS-IPA, mSPECS-IPA-CAIPIRINHA, mSPECS-IPA-VAT and mSPECS-IPA-CAIPIVAT model with different acceleration factors. B. The g -factor value of reconstructed brain images slice 3 from mSPECS-IPA, mSPECS-IPA-CAIPIRINHA, mSPECS-IPA-VAT and mSPECS-IPA-CAIPIVAT model with different acceleration factors.	107
6.12	The average CNR value of ROI for odd slices of reconstructed images from mSPECS-IPA, mSPECS-IPA-CAIPIRINHA, mSPECS-IPA-VAT and mSPECS-IPA-CAIPIVAT model with TPA=2.	109
6.13	The task activation detection (z-score) map of ROI for odd slices of reconstructed images from mSPECS-IPA, mSPECS-IPA-CAIPIRINHA, mSPECS-IPA-VAT and mSPECS-IPA-CAIPIVAT model with TPA=2.	110
6.14	A. The average CNR value of ROI for slice 3 from mSPECS-IPA, mSPECS-IPA-CAIPIRINHA, mSPECS-IPA-VAT, and mSPECS-IPA-CAIPIVAT model with acceleration factor TPA=2, TPA=4, and TPA=8. B. The average activation detection rate (z-score) of ROI for slice 3 from mSPECS-IPA, mSPECS-IPA-CAIPIRINHA, mSPECS-IPA-VAT, and mSPECS-IPA-CAIPIVAT model with acceleration factor TPA=2, TPA=4, and TPA=8.	111
6.15	The mean magnitude from reconstructed image with in-plane acceleration factor $IPA = 2$ through-plane acceleration factor $TPA = 2$ corresponding to GRAPPA for mSPECS-IPA, GRAPPA for mSPECS-IPA-CAIPIRINHA, GRAPPA for mSPECS-IPA-VAT and GRAPPA for mSPECS-IPA-CAIPIVAT model.	113

6.16	The mean phase from reconstructed image with in-plane acceleration factor $IPA = 2$ through-plane acceleration factor $TPA = 2$ corresponding to GRAPPA for mSPECS-IPA, GRAPPA for mSPECS-IPA-CAIPIRINHA, GRAPPA for mSPECS-IPA-VAT and GRAPPA for mSPECS-IPA-CAIPIVAT model.	114
6.17	The temporal variance of task signal from reconstructed image for slice 3 from GRAPPA for mSPECS-IPA, GRAPPA for mSPECS-IPA-CAIPIRINHA, GRAPPA for mSPECS-IPA-VAT and GRAPPA for mSPECS-IPA-CAIPIVAT model with in-plane acceleration factor $IPA = 2$ different acceleration factor $TPA = 2$, $TPA = 4$, and $TPA = 8$. . .	116
6.18	A. The SNR value of reconstructed brain images slice 3 from GRAPPA for mSPECS-IPA, GRAPPA for mSPECS-IPA-CAIPIRINHA, GRAPPA for mSPECS-IPA-VAT and GRAPPA for mSPECS-IPA-CAIPIVAT model with in-plane acceleration factor $IPA = 2$ and different through-plane acceleration factors, $TPA = 2$, $TPA = 4$, and $TPA = 8$. B. The g -factor value of reconstructed brain images slice 3 from GRAPPA for mSPECS-IPA, GRAPPA for mSPECS-IPA-CAIPIRINHA, GRAPPA for mSPECS-IPA-VAT and GRAPPA for mSPECS-IPA-CAIPIVAT model with in-plane acceleration factor $IPA = 2$ and different through-plane acceleration factors, $TPA = 2$, $TPA = 4$, and $TPA = 8$	117
6.19	The average CNR value of ROI of reconstructed images from GRAPPA for mSPECS-IPA, GRAPPA for mSPECS-IPA-CAIPIRINHA, GRAPPA for mSPECS-IPA-VAT and GRAPPA for mSPECS-IPA-CAIPIVAT model with $IPA = 2$ and $TPA = 2$	118

- 6.20 The task activation detection (z-score) map of ROI of reconstructed images from the GRAPPA for mSPECS-IPA, GRAPPA for mSPECS-IPA-CAIPIRINHA, GRAPPA for mSPECS-IPA-VAT, and GRAPPA for mSPECS-IPA-CAIPIVAT models with $IPA = 2$ and $TPA = 2$ 119
- 6.21 A. The average *CNR* value of ROI for slice 3 from GRAPPA for mSPECS-IPA, GRAPPA for mSPECS-IPA-CAIPIRINHA, GRAPPA for mSPECS-IPA-VAT, and GRAPPA for mSPECS-IPA-CAIPIVAT model with in-plane acceleration factor $IPA = 2$ and through-plane acceleration factor $TPA = 2$, $TPA = 4$, and $TPA = 8$. B. The average activation detection rate (z-score) of ROI for slice 3 from GRAPPA for mSPECS-IPA, GRAPPA for mSPECS-IPA-CAIPIRINHA, GRAPPA for mSPECS-IPA-VAT, and GRAPPA for mSPECS-IPA-CAIPIVAT model with in-plane acceleration factor $IPA = 2$ and through-plane acceleration factor $TPA = 2$, $TPA = 4$, and $TPA = 8$ 121

CHAPTER 1: INTRODUCTION

1.1 fMRI Background

As a powerful and non-invasive medical imaging tool, functional Magnetic Resonance Imaging (fMRI) has played a predominant role in brain imaging studies. The activity of neurons cannot be directly detected but is correlated to the Blood Oxygen Level Dependence (BOLD) contrast signal which is used as a proxy (Ogawa et al. (1990)). When the task-related neuronal region transitions from the resting state to the task state, the blood flow to the active area of the brain increases, leading to a higher ratio of oxyhemoglobin to deoxyhemoglobin (Glover (2011)). By detecting task-related changes in the BOLD signal inside our brain, the magnetic resonance (MR) scanner can map our brain with a unique radio frequency (RF) pulse sequence (Ogawa et al. (1990), Glover (2011)). The Gradient Echo Echo-Planer Imaging (GE-EPI) pulse sequence is widely used in fMRI studies to shorten the scan time and decrease the influence of the motion of subjects by acquiring full k -space spatial information within a single excitation (Mansfield (1977); Rzedzian et al. (1983); Stehling et al. (1991); Poustchi-Amin et al. (2001)). For each excitation of the GRE-EPI pulse sequence, a zig-zag data collection pattern is followed sequentially to form the full k -space with each data point represents complex-valued spatial frequency information for the corresponding image. However, conducting an fMRI experiment requires acquiring multiple brain images at different positions, forming what is known as a volume-image. As a result, acquiring a volume-image fMRI time series takes a relatively long time to ensure a steady and reliable task-related activation signal.

In-Plane Acceleration

In 1986, Hyde introduced a parallel image acquisition technique that incorporated coil combination by utilizing spatially variable receive coil sensitivities for parallel imaging (Hyde et al. (1986)). The full brain image can be reconstructed by applying the Sensitivity Encoding (SENSE) approach to combine weighted spatial frequencies from each coil into one single k -space array (Pruessmann et al. (1999)). In structural and functional MRI studies, the time to measure a volume image is dependent upon how rapidly the amount of data necessary to reconstruct an image can be measured. In order to accelerate the number of images measured per unit time, a topic of study has been to measure less data but still be able to reconstruct a high-quality image with clear anatomical information. To reconstruct images using less data, multiple receiver coils are used where each coil measures sensitivity-weighted images (Sodickson and Manning (1997); Nencka and Jesmanowicz (2013)). Initially, accelerated imaging was aimed at In-Plane Acceleration (IPA) where spatial frequency data are partially skipped, and each coil measured fewer lines of the spatial frequency array. Figure 1.1A shows the acquisition of spatial frequency data with an acceleration factor of $IPA = 2$. The data are acquired sequentially following a zig-zag pattern (black dots), with every other line in k -space (white dots) skipped. Figure 1.1B shows the acquired subsampled k -space from four receiver coils. The dimension of the acquired subsampled k -space is half of the full k -space due to $IPA = 2$. In parallel imaging techniques, like Generalized Autocalibrating Partially Parallel Acquisitions (GRAPPA) (Griswold et al. (2002)), a single slice has been excited, and partial lines of k -space skipped, resulting in a sensitivity weighted aliased image for each coil, that is combined into a single complete image. Bayesian techniques have been applied to improve the resolution of the reconstructed images by incorporating the anatomical information from prior distributions into the k -space (Kornak et al. (2010); Kornak et al. (2020)). Other in-plane imaging acceleration techniques like partial Fourier

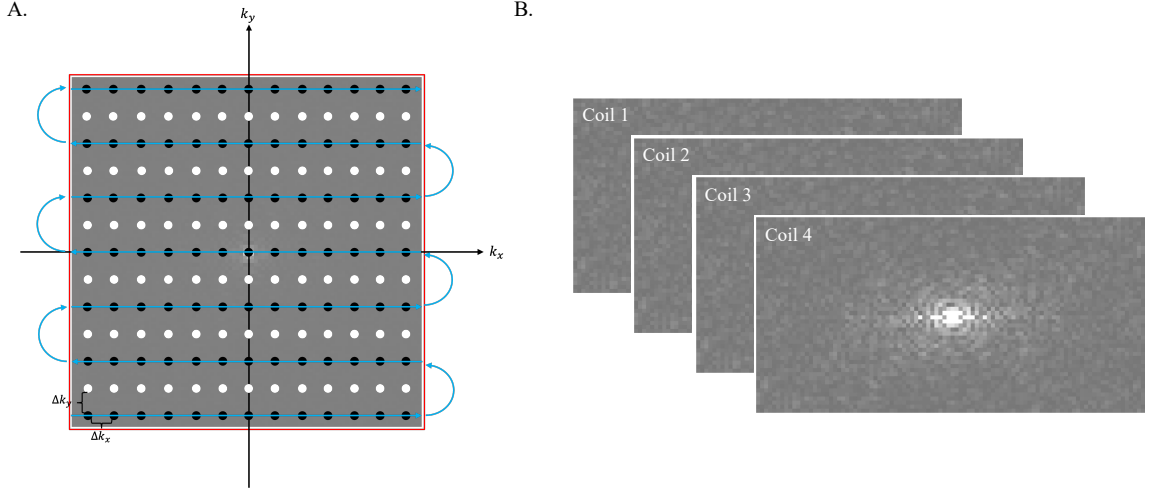


Figure 1.1: A. The subsampled spatial frequency domain incorporated with IPA approach and the acceleration factor equal to 2. B. The acquired subsampled k -space acquired from four receiver coils.

imaging technique (Feinberg et al. (1986); Noll et al. (1991)) can acquire half of the lines in the k -space. The unacquired spatial frequency data can be determined due to the Hermitian symmetry property of the k -space to reconstruct real-valued images. Moreover, a rapid three dimensional volume-image method has been established to sample the k -space (Lindquist et al. (2008)). However, considering some fixed time blocks in the data-acquiring process, for instance, imaging encoding and the proper time for T_2^* contrast in one excitation, the scan time will not decrease significantly in IPA techniques.

Through-Plane Acceleration

More recently, Simultaneous Multi-Slice (SMS) techniques were developed and discussed (Souza et al. (1988); Rowe et al. (2013); Barth et al. (2016)). Figure 1.2 shows the 3D and 2D view of an example for SMS technique with four images are acquired concurrently and four receiver coils. The SMS technique is extensively used in fMRI studies, and it allows for acquiring fMRI data with high resolution by using a multiband (MB) radiofrequency (RF) within a reduced repetition time (TR). Com-

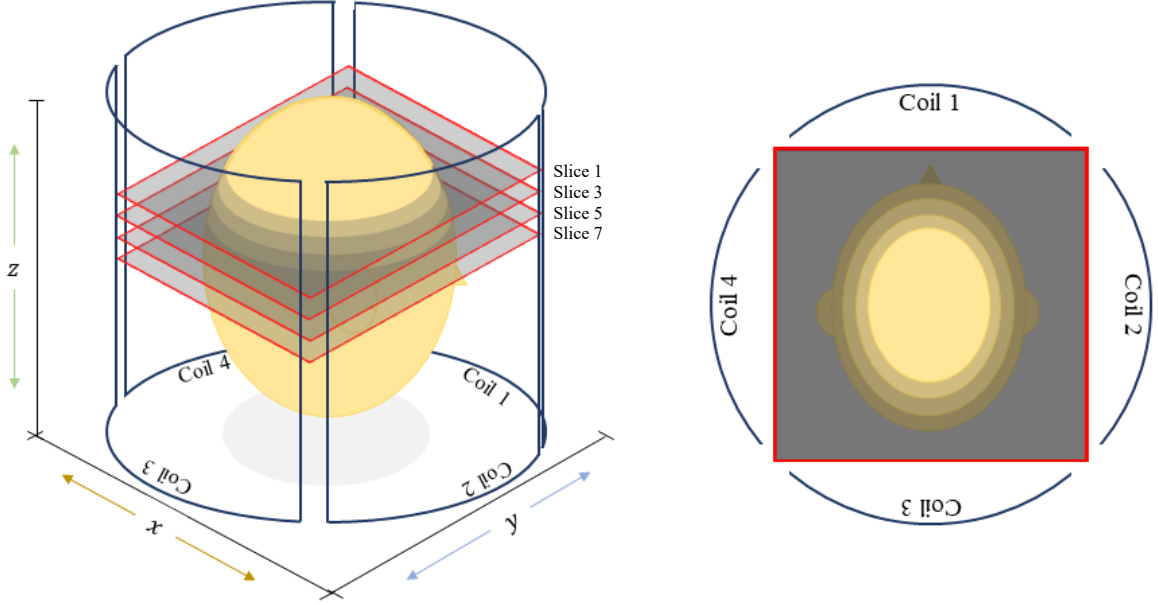


Figure 1.2: The 3D view (left) and 2D view (right) of an example for SMS technique with four slices and four coils.

pared with conventional parallel imaging techniques, in SMS techniques, multiple slices are acquired concurrently and aliased together in one excitation, and hence, the image-acquiring time will decrease with a factor of the total number of aliased slices. Thus, Through-Plane Acceleration (TPA) is achieved using SMS techniques, offering a more efficient approach to image acquisition compared to In-Plane Acceleration (IPA) methods.

In this dissertation, we present three novel SMS imaging reconstruction techniques with high acceleration factors. The first technique incorporates only the TPA acceleration method. The second technique combines both IPA and TPA acceleration methods. The third technique also combines IPA and TPA acceleration methods, but additionally utilizes the GRAPPA technique to estimate the missing spatial frequencies in k -space.

1.2 Image Shift Techniques

Since multiple slices are acquired at the same time for one excitation of the TPA technique, a short distance between aliased slices will lead to a high similarity of voxel and coil sensitivity information. When applying the standard SENSE method, this may cause a singular matrix problem and strong inter-slice signal leakage will appear on the reconstructed images. As a result, incorrect anatomical information from other brain slices may appear, making the interpretation of the reconstructed images more difficult. In fMRI studies, the brain image can be shifted along three directions: the phase-encoding (PE) direction (vertically in this dissertation), the readout (RO) direction (horizontally in this dissertation), and PE and RO direction concurrently (vertically and horizontally at the same time in this dissertation). To decrease the influence of the geometry properties of the coil sensitivity maps, techniques like “controlled aliasing in parallel imaging results in higher acceleration” (CAIPIRINHA), “blipped-CAIPIRINHA” (Blipped-CAIPI), and Hadamard phase-encoding provide other possible ways to minimize the influence of the geometric factor (g -factor) and increase the conditioning of the slices aliasing matrix (Breuer et al. (2005); Jesmanowicz et al. (2011); Setsompop et al. (2012)). By modulating the phase for each line in k -space and imparting each line with a specific angle, the field-of-view (FOV) is moved in the phase-encoding direction. Applying a unique phase modulation amount to each slice in the aliased image-acquiring process increases the physical distance between the aliased voxels. Therefore, the difference of coil sensitivity for each slice will increase and the influence of the g -factor for each excitation is minimized. Moreover, to shift the brain image along the RO direction, a technique like the view angle tilting (VAT) approach applies compensation gradients to the slice selection direction to correct the chemical-shift artifacts in the image scanning process (Cho et al. (1988); Kim et al. (2012)). The distance shifted along the RO direction is relate to the view angle θ in the data acquisition process. Furthermore, to further increase the physical

distance between two aliased voxels and expose more information beneath the coil sensitivities, the FOV can not only be moved along the vertical PE direction but also the horizontal RO direction. The study “multislice CAIPRINHA using view angle tilting technique” (CAIPIVAT) (Jungmann et al. (2015), Kim et al. (2016)) proposes a method combining the CAIPRINHA technique and View Angle Tilting (VAT) (Kim et al. (2012)) technique together by applying a unique compensation gradient of VAT. Figure 1.3 shows the k -space representations for the CAIPRINHA, VAT, and CAIPIVAT techniques, along with the reconstructed brain images after applying the inverse Fourier transform. In Figure 1.3, white dots represent spatial frequency data points with a phase modulation of π , while black dots indicate spatial frequency data points without phase modulation. The star in Figure 1.3 denotes the application of an additional global phase modulation along the readout (RO) direction to produce horizontal image shift artifacts.

1.3 Complex-valued Bayesian Model

The future can be predicted based on past data. As a dominant methodology in statistical studies, the Bayesian approach can be integrated into other research areas by incorporating prior knowledge. Functional magnetic resonance imaging (fMRI) studies can be interpreted following the Bayesian methodology but with complex-valued observations. To set up a complex-valued Bayesian linear model, the complex-valued observation can be written as equation 1.1:

$$a_C = X_C \beta_C + \varepsilon_C. \quad (1.1)$$

In equation 1.1, a_C is a $p \times 1$ complex-valued observed vector, X_C is a $p \times q$ complex-valued design known matrix, β_C is a $q \times 1$ complex-valued unobserved regression coefficient vector, and ε_C is a complex-valued measurement error vector with same dimension as vector a_C , where p is the number of observations, and q is the number of

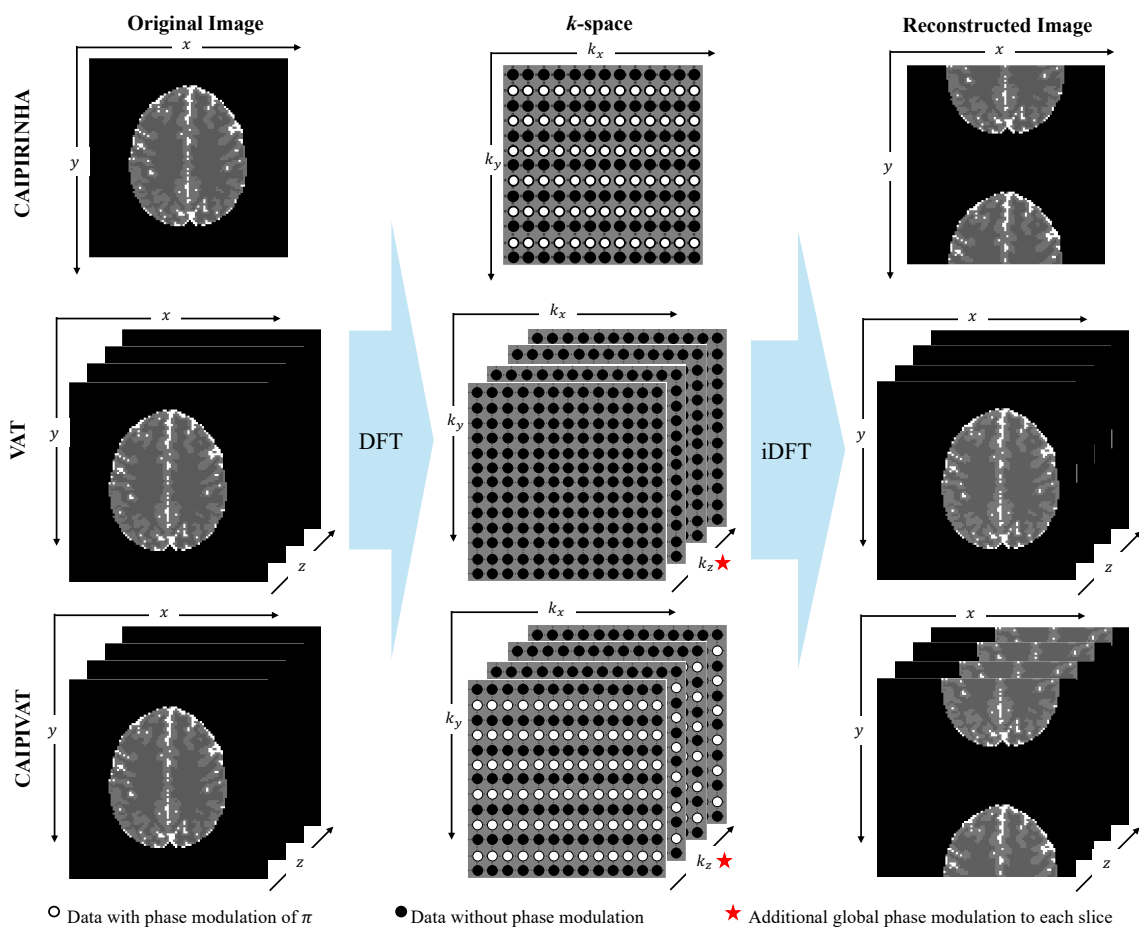


Figure 1.3: Top row: the image shift process corresponding to the CAIPIRINHA technique (shifted vertically). Middle row: the image shift process corresponding to the VAT technique (shifted horizontally). Bottom row: the image shift process corresponding to the CAPIVAT technique (shifted vertically and horizontally).

regression coefficients. Moreover, the real and imaginary component of the measurement error ε_C follow normal distribution with $\varepsilon_R, \varepsilon_I \sim N(0, \sigma^2 I_p)$. Equation 1.1 can be reformulated through a real-valued isomorphism to transform the complex-valued model into a real-valued model:

$$\begin{bmatrix} a_R \\ a_I \end{bmatrix} = \begin{bmatrix} X_R & -X_I \\ X_I & X_R \end{bmatrix} \begin{bmatrix} \beta_R \\ \beta_I \end{bmatrix} + \begin{bmatrix} \varepsilon_R \\ \varepsilon_I \end{bmatrix}. \quad (1.2)$$

In equation 1.2, the dimension of observation vector $a = [a_R; a_I]$ is $2p \times 1$, the dimension of design matrix $X = [X_R, -X_I; X_I, X_R]$ is $2p \times 2q$, the dimension of regression coefficient vector $\beta = [\beta_R; \beta_I]$ is $2q \times 1$, and the dimension of measurement error vector $\varepsilon = [\varepsilon_R; \varepsilon_I]$ is $2p \times 1$. Thus, the likelihood distribution of the multivariate observation is:

$$P(a | X, \beta, \sigma^2) \propto (\sigma^2)^{-\frac{2p}{2}} \exp \left[-\frac{1}{2\sigma^2} (a - X\beta)' (a - X\beta) \right], \quad (1.3)$$

with independent and identical noise variance for a_1, \dots, a_p . The coil measurements, assuming there is not a coil covariance follow a normal distribution, $a \sim N(X\beta, \sigma^2 I_{2p})$. In the linear regression model, the regression coefficients can be estimated through maximum likelihood estimation (MLE):

$$\hat{\beta}_{MLE} = (X'X)^{-1} X'a. \quad (1.4)$$

And the estimated variance through MLE is:

$$\hat{\sigma}_{MLE}^2 = \frac{1}{2p} (a - X\hat{\beta})' (a - X\hat{\beta}). \quad (1.5)$$

Based on prior knowledge and experience, the regression coefficient β is specified to have a normal prior distribution $P(\beta | \sigma^2)$, and the variance of the measurement

error σ^2 is specified to have an inverse gamma prior distribution $P(\sigma^2 | \cdot)$. Thus, the posterior distribution of regression coefficient β and variance σ^2 is proportional to the joint distribution of the likelihood and the prior distributions:

$$P(\beta, \sigma^2 | \cdot) \propto P(a | X, \beta, \sigma^2)P(\beta | \sigma^2)P(\sigma^2 | \cdot). \quad (1.6)$$

The joint posterior distribution of the regression coefficient β and variance of measurement error σ^2 can be integrated to obtain their marginal distributions and hence their marginal posterior mean (MPM) and variance. More details are provided in following chapters.

CHAPTER 2: A BAYESIAN APPROACH OF MSPECS-CAIPIVAT

In this Chapter, we introduce the mSPECS-CAIPIVAT model in a Bayesian manner. We incorporate different slice-wise image shift techniques and the Hadamard phase-encoding technique together in which different voxel combinations is acquired for each excitation. In the unaliasing process, calibration reference images are artificially aliased, and the artificial aliasing matrix used to assess hyperparameters of prior distributions in the separation process. The artificial aliased calibration imaging technique and bootstrap sampling approach is combined and applied into the model to eliminate inter-slice signal leakage in the reconstruction images at the cost of a slightly increased variance of the calibration images forming the prior variance. The marginal posterior distribution can be obtained by integration to calculate the marginal posterior mean and variance of the estimated reconstruction voxel. The mSPECS-CAIPIVAT model provides a solution to significantly reduce the scan time with a high acceleration factor, meanwhile providing high-resolution and high-quality reconstruction images.

2.1 The Data Acquiring Process in mSPECS-CAIPIVAT

2.1.1 Image Shift Techniques in mSPECS-CAIPIVAT

As mentioned in Chapter 1.2, the physical distance between two aliased voxels can be increased by applying the CAIPIRINHA, the VAT, and the CAIPIVAT techniques to achieve slice-wise image shifts, thus reducing the dependence on the geometry of the coil array. The CAIPIRINHA technique can move the FOV along the PE direction (vertical) by modulating the phase for each line in k -space. The VAT technique can move the FOV along the RO direction (horizontal) by modulating the phase along the RO direction. Whereas the CAIPIVAT technique can shift the FOV along two directions, PE (vertical) and RO (horizontal), by applying a unique

compensation gradient of VAT. Through these three image shift techniques along with the Hadamard slice encoding technique, the g -factor of the reconstructed images can be reduced. Since the g -factor is related to the signal-to-noise ratio (SNR), in SMS studies, giving the definition of the SNR (Pruessmann (2004)):

$$SNR_{SMS} = SNR_{full}/(g\sqrt{R}), \quad (2.1)$$

where R is the IPA factor. From equation 2.1, the SNR_{SMS} is strongly influenced by the geometric properties of the coil array, g -factor. It depends on the number and location of the coils, the phase-encoding direction, the voxel location. Thus, the g -factor is not a constant value but varies across each voxel within the images (Preibisch et al. (2015)). A short physical distance between two aliased voxels increases the g -factor due to the high similarity in their coil sensitivity profiles, thereby reducing the SNR_{SMS} as described in equation 2.1. Therefore, increasing the physical distance between two aliased voxels is one of our strategies. The CAIPIRINHA technique, the VAT technique, and the CAPIVAT technique can reduce the influence of the g -factor by applying a partial in-plane image shift. Considering the 1D inverse discrete Fourier transform, a periodic time series $y(t)$ sampled at n time points Δt apart is described as below:

$$y(p\Delta t) = \sum_{q=-\frac{n}{2}}^{\frac{n}{2}-1} f(q\Delta\nu) e^{i\frac{2\pi}{n}pq}, \quad (2.2)$$

where $\Delta\nu$ is the temporal frequency resolution and $\Delta\nu = 1/(n\Delta t)$. It is the summation of the Fourier amplitude coefficients at multiple various frequencies. In equation 2.2, $y(p\Delta t)$ and $f(q\Delta\nu)$ are complex-valued quantities with real and imaginary components. When we shift the whole time series from $p\Delta t$ to $p'\Delta t$, where $y(p'\Delta t)$ is same as $y(p\Delta t)$ sampled at n time points Δt apart with a different order from $y(p\Delta t)$,

a field-of-view shift Δy occurs and is:

$$\Delta y = y((p - p')\Delta t) = \sum_{q=-\frac{n}{2}}^{\frac{n}{2}-1} f(q\Delta\nu)e^{i\frac{2\pi}{n}pq}e^{-i\frac{2\pi}{n}p'q}, \quad (2.3)$$

for $p = 1, \dots, n$. The FOV shift only depends on the phase change in k -space, which equals $-2\pi p'q/n$. If $p' = 1$, which means the image moves one voxel distance in the PE direction, the modulation quantity of phase is $-2\pi q/n$. If half of the image is shifted in the PE direction (FOV/2), $p' = n/2$, the modulation of phase should be $-\pi q$. Therefore, the phase of even lines in k -space should impart π and the phase of odd lines should impart 0. If the FOV/4 shift of the image needs to be achieved, the modulation of the phase for each line in the k -space needs to be adjusted to different amount.

In this chapter, the principal idea of the CAIPIRINHA technique is applied first. For each slice within each excitation, we imply $\Delta y = (l - 1)FOV/N_s$ in-plane image shift, where $l = 1, \dots, N_s$ and N_s is the total number of aliased slices. On the TR dimension, we also imply the CAIPIRINHA technique for each excitation by $\Delta y = (m - 1)FOV/N_s$ in-plane image shift, where $m = 1, \dots, N_s$. Thus, with the in-excitation and through-excitation image shift, at the $TR = N_s + 1$ excitation time point, the aliased artifacts should be the same as the $TR = 1$ excitation time point. Figure 2.1A shows an example of an in-excitation and through-excitation image shift process with $N_s = 4$ incorporating with the CAIPIRINHA technique. When $TR = 5$, the image shift pattern for each slice should be the same as the time point $TR = 1$. The VAT technique is also applied in this chapter. For each excitation, each slice is shifted horizontally with a amount of image shift distance is related to the view angle (Kim et al. (2016)). There is no image shift along the phase-encoding (PE) direction. Figure 2.1B shows an example of an in-excitation and through-excitation image shift process with $N_s = 4$ incorporating with the VAT technique. When $TR = N_s + 1$,

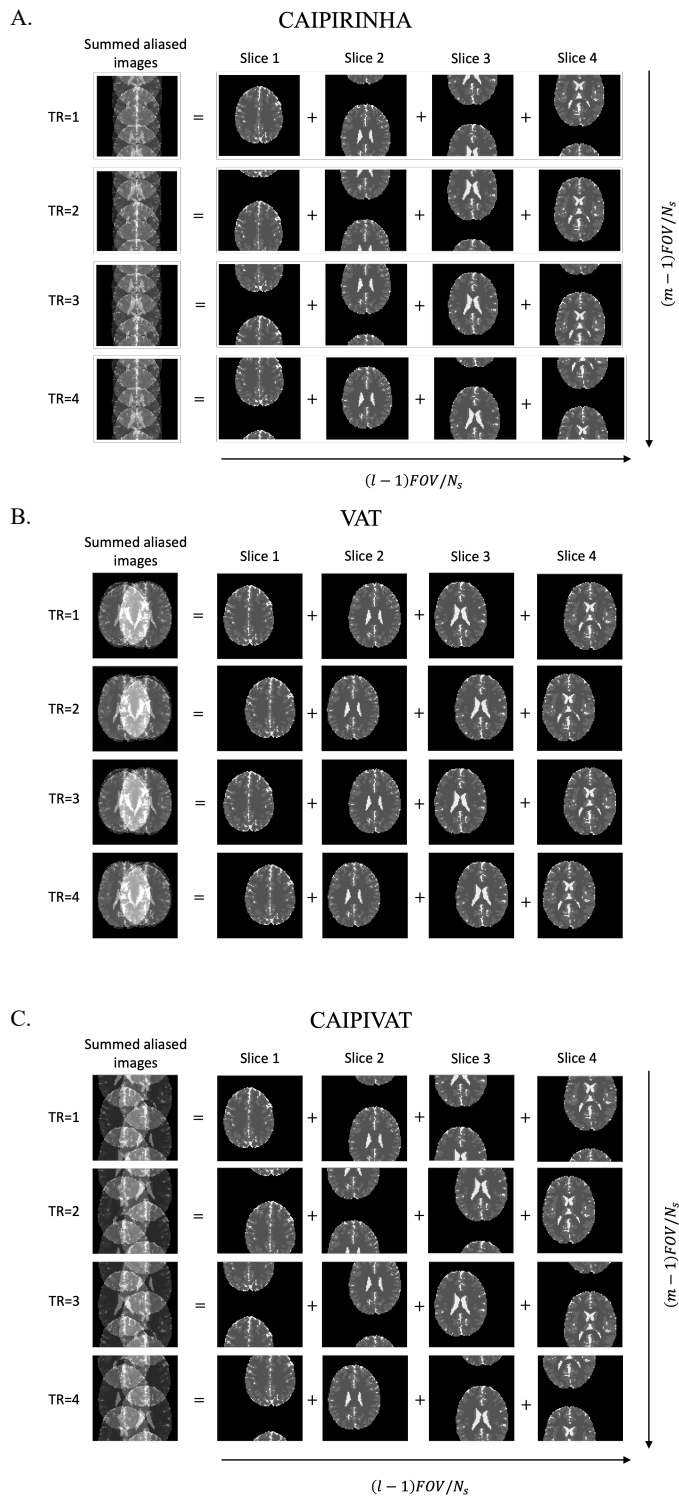


Figure 2.1: A. An example of in-excitation and through-excitation image shift process with $N_s = 4$ by applying the CAIPIRINHA technique. B. An example of in-excitation and through-excitation image shift process with $N_s = 4$ by applying the VAT technique. C. An example of in-excitation and through-excitation image shift process with $N_s = 4$ by applying the CAIPIVAT technique.

the image shift pattern for each slice should be the same as the time point $TR = 1$. Furthermore, the principal idea of the CAIPIVAT technique will also be applied. Similar to the CAIPIRINHA technique, $\Delta y = (l - 1)FOV/N_s$ for the in-plane image shift and $\Delta y = (m - 1)FOV/N_s$ for the through-plane image shift is applied to each excitation along the PE direction. For each slice within each excitation, a unique image shift will appear horizontally on the RO direction with the support of the CAIPIVAT technique. The shift distance for each slice along the RO direction can be calculated and depends on the distance between the desired aliased slices, the compensation gradient, and the RO gradient. A modest slice-wise shift is applied for each excitation to ensure the brain image is not outside the FOV. Figure 2.1C displays an example of in-excitation and through-excitation image shift process of $N_s = 4$ incorporating with the CAIPIVAT technique. Besides the same amount of the FOV shift in- and through-excitation on the PE direction as CAIPIRINHA technique, slice 1 and slice 3 will have a FOV shift to the left and slice 2 and slice 4 will have a FOV shift to the right on the RO direction according to the CAIPIVAT technique. Thus, comparing with the CAIPIRINHA technique approach, the overlapping area between two desired aliased images will decrease and the independence of the sensitivity for each coil will increase.

2.1.2 The Hadamard Phase Encoding

The Hadamard encoding technique is a well-developed volume excitation method. The conventional MR imaging techniques have been limited by the size of the matrix for the acquired aliased images. The Hadamard phase-encoding method allows the increment of the size of the acquired aliased image matrix by aliasing in both frequency and phase encoding dimensions. With the support of this simultaneous binary-encoded technique, the TR will decrease, and the SNR ratio will improve.

The Hadamard matrix is given by:

$$H_{2^n} = \begin{bmatrix} H_{2^{n-1}} & H_{2^{n-1}} \\ H_{2^{n-1}} & -H_{2^{n-1}} \end{bmatrix} = H_2 \otimes H_{2^{n-1}}, \text{ and } H_1 = \begin{bmatrix} 1 \end{bmatrix}, H_2 = \begin{bmatrix} 1 & 1 \\ 1 & -1 \end{bmatrix}, \quad (2.4)$$

where \otimes denotes the Kronecker product. It is an orthogonal and full rank matrix with elements of either +1 or -1. In the mSPECS-CAPIVAT study, each excitation is sequentially coordinated with a unique Hadamard aliasing pattern. To improve the computational efficiency, we select the size of the Hadamard phase-encoding matrix to be the same as the number of the aliased slices. Thus, the size of the Hadamard phase-encoding matrix is $N_s \times N_s$. In this aim, $H_{\delta,z}$ is the δ th row and z th column element of Hadamard matrix corresponding to z th slice in δ th TR. Due to the characteristics of the Hadamard aliasing coefficient matrix, the number of aliased slices must be a power of two, which may represent a potential limitation of this approach. Alternative techniques, such as orthogonal contrast, may offer a potential solution for handling aliasing scenarios involving an odd number of slices. Same as the sequential properties of image shifts, the Hadamard phase-encoding aliasing pattern will cycle through along the TR dimension. For example, the Hadamard aliasing pattern of $TR = N_s + 1$ should be the same as $TR = 1$. Figure 2.2 shows an example of the Hadamard aliasing pattern when $N_s = 4$. Figure 2.2A shows a 4×4 Hadamard matrix, Figure 2.2B shows the Hadamard coefficients for each slice in the fMRI time series, Figure 2.2C shows the phantom brain images multiplied by Hadamard aliasing coefficients at the first 4 TRs. In order to increase the distance between two aliased voxels and reduce the influence of the g -factor, we introduce the term ‘‘packet’’ to indicate the slice aliasing circumstance. For example, under a circumstance with $N_s = 8$ and $N_\alpha = 2$, we put odd number slices into one packet (i.e., slice 1, slice 3, slice 5, and slice 7), and even number slices into another packet (i.e., slice 2, slice 4, slice 6, and slice 8). For each excitation, all slices in one packet are measured simultaneously as one single array.

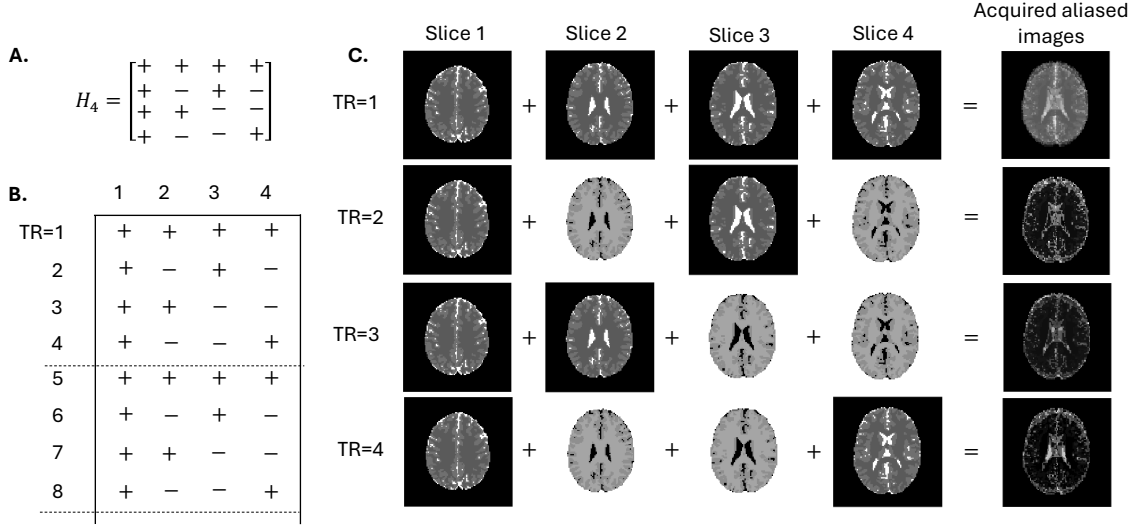


Figure 2.2: An illustration of Hadamard phase-encoding aliasing pattern when $N_s = 4$. A. shows the H_4 matrix with plus sign denotes as 1 and minus sign demotes as -1. B. shows sequential Hadamard aliasing coefficient for each slice in the fMRI time series. C. shows the phantom brain images are multiplied by the Hadamard aliasing coefficients at the first 4 TRs.

Therefore, we will have 2 packets in this situation, and both packets will coordinate with the same Hadamard phase-encoding aliasing pattern. With the help of the packet technique, the slice-to-slice signal leakage artifacts will diminish.

2.1.3 A Single Aliased Voxel

Given a single aliased voxel, $a_{j,\gamma,\delta}$, at the location (x, y) of aliased images, with δ th Hadamard aliasing pattern and γ th matrix rotation operation, measured at coil j , is defined as the summation equation:

$$a_{j,\gamma,\delta} = \sum_{z=1}^{N_s} H_{\delta,z} R_{\gamma,z} S_{j,z} \beta_z + \varepsilon_j. \quad (2.5)$$

In equation 2.5, $a_{j,\gamma,\delta}$ is a 2×1 complex-valued vector with the real and imaginary components of the acquired aliased voxel value measured at coil j , with rotating operation γ and Hadamard phase-encoding aliasing pattern δ . The Hadamard phase-encoding aliasing pattern, $H_{\delta,z}$, is the same as the definition in Chapter 2.1.2, where

parameter δ corresponds to the order of Hadamard coefficients pattern, and parameter z corresponds to the slice number. The coefficients of $H_{\delta,z}$ is either +1 or -1. The matrix rotation operator, $R_{\gamma,z}$, is closely related to the definition of Chapter 2.1.1. Subscript γ denotes the order of the matrix rotation operation for each TR, and parameter z corresponds to the number of slices. The coil sensitivity matrix, $S_{j,z}$, is a 2×2 skew symmetric matrix with the real and imaginary components at coil j for slice z , $S(j,z) = [S_R, -S_I; S_I, S_R]_{j,z}$. The true voxel value, $\beta_z = [\beta_{zR}; \beta_{zI}]$, is a 2×1 vector with the real and imaginary parts of the aliased voxel in slice z , and the real part is stacked on the top of the imaginary part. The measurement noise, $\varepsilon_j = [\varepsilon_R; \varepsilon_I]$, is a 2×1 vector with real and imaginary parts stacked. The mean of measurement noise is $E(\varepsilon_j) = 0$, and the covariance of error is $cov(\varepsilon_j) = \sigma^2 I_2$, where I_2 is a 2×2 identity matrix.

Considering the measured aliased voxel in equation 2.5 across the N_c coils for N_s aliased slices with N_α time-points in the fMRI time series, equation 2.5 can be expressed as:

$$a = X_A \beta + \varepsilon. \quad (2.6)$$

N_α denotes the number of sequential time-points of the Hadamard encoded pattern, and it is an integer between 1 and N_s . Therefore, the net acceleration of the fMRI time series acquisition is defined as $A = N_s/N_\alpha$. In equation 2.6, the dimension of a is $2N_c N_\alpha \times 1$ including the real and imaginary components. The measurement error, ε , has the same dimension as a with the mean $E(\varepsilon) = 0$ and covariance $cov(\varepsilon) = \sigma^2 I_{2N_c N_\alpha}$. The dimension of the aliasing matrix, X_A , is $2N_c N_\alpha \times 2N_s N_r$, where N_r is an indicator of the number of matrix rotation operations. In this study, we generally assign $N_r = N_s$ to improve the computational efficiency. The true voxel value, β , has the dimension of $2N_s N_r \times 1$, including the real and imaginary value for each voxel. For the δ th Hadamard aliasing pattern and γ th matrix rotating operation, the aliasing

matrix $(X_A)_{\gamma,\delta}$ across N_c coils is defined as:

$$(X_A)_{\gamma,\delta} = \left[H_{\delta,1} R_{\gamma,1} \begin{pmatrix} S_{1,1} \\ \vdots \\ S_{N_c,1} \end{pmatrix}, \dots, H_{\delta,N_c} R_{\gamma,N_c} \begin{pmatrix} S_{1,N_c} \\ \vdots \\ S_{N_c,N_c} \end{pmatrix} \right]. \quad (2.7)$$

$R_{\gamma,z}$ is the image shift indicator which operates on coil sensitivity maps for each slice, and not matrix multiplication. Across the N_α excitations, the aliasing matrix X_A is written as:

$$X_A = \left[(X_A)_1, \dots, (X_A)_{N_\alpha} \right]'. \quad (2.8)$$

Since the measurement error has a Gaussian distribution, the likelihood of the acquired aliased voxel for the N_c coils and the N_α excitations is:

$$P(a | X_A, \beta, \sigma^2) \propto (\sigma^2)^{-\frac{2N_c N_\alpha}{2}} \exp \left[-(a - X_A \beta)' (a - X_A \beta) / (2\sigma^2) \right]. \quad (2.9)$$

To separate the aliased images and estimate the voxel value for each slice, the least square estimation method is used. The estimated separate voxel value, $\hat{\beta}$, can be calculated by:

$$\hat{\beta}_{MLE} = (X_A' X_A)^{-1} X_A' a. \quad (2.10)$$

Equation 2.10 also can be used to calculate the reconstructed brain images in the SENSE model. In general, the determinant of X_A is close to zero, $\det(X_A) \approx 0$, which leads to failure in calculating the inverse of $X_A' X_A$. Thus, a bootstrap sampling method incorporated with artificial aliasing of reference calibration images technique are combined with the mSPECS-CAPIVAT model. This combined technique can reduce the inter-slice signal leakage artifacts by quantifying prior information in calibration images in a Bayesian model. More details is shown in the following section. Figure 2.3 illustrates the data-acquiring process of the mSPECS technique (without

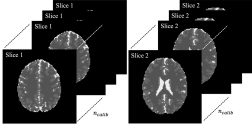
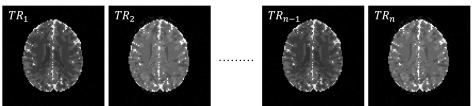
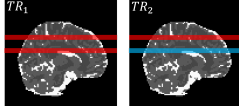
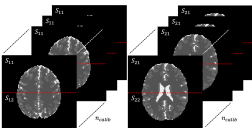
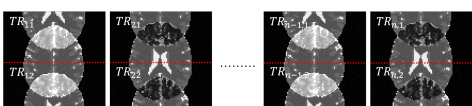
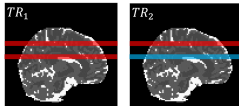
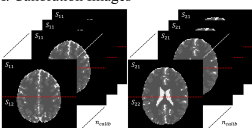
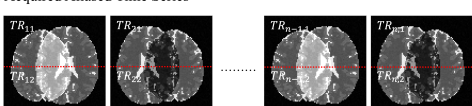
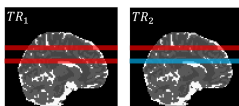
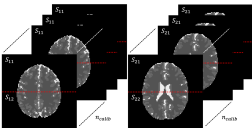
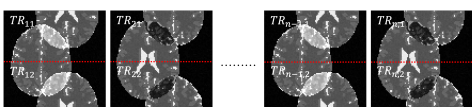
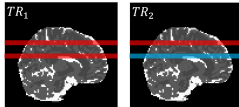
mSPECS	A. Calibration Images 	B. Acquired Aliased Time Series 
	C. Sagittal View of Time Series  $TR_1 = Slice_1 + Slice_2 + \epsilon$ $TR_2 = Slice_1 - Slice_2 + \epsilon$	D. Separation Process $\widehat{Slice}_1 = \frac{TR_1 + \overline{TR}_2}{2} = \frac{(Slice_1 + Slice_2) + (\widehat{Slice}_1 - \widehat{Slice}_2)}{2}$ $\widehat{Slice}_2 = \frac{\overline{TR}_1 - TR_2}{2} = \frac{(\widehat{Slice}_1 + \widehat{Slice}_2) - (Slice_1 - Slice_2)}{2}$ TR_1 and TR_2 are acquired aliased images from time series. \overline{TR}_1 and \overline{TR}_2 are artificial aliased calibration images.
	A. Calibration Images 	B. Acquired Aliased Time Series 
	C. Sagittal View of Time Series  $TR_1 = Slice_1 + Slice_2 + \epsilon$ $TR_2 = Slice_1 - Slice_2 + \epsilon$	D. Separation Process $\begin{bmatrix} \widehat{S}_{11} \\ \widehat{TR}_{12} \\ \widehat{S}_{12} \end{bmatrix} = \frac{\begin{bmatrix} TR_{11} \\ TR_{12} \end{bmatrix} + \begin{bmatrix} \overline{TR}_{11} \\ \overline{TR}_{12} \end{bmatrix}}{2} = \frac{\begin{bmatrix} S_{11} + S_{22} \\ S_{12} + S_{21} \end{bmatrix} + \begin{bmatrix} S_{11} - S_{22} \\ S_{12} - S_{21} \end{bmatrix}}{2}$ $\begin{bmatrix} \widehat{S}_{21} \\ \widehat{TR}_{22} \\ \widehat{S}_{22} \end{bmatrix} = \frac{\begin{bmatrix} \overline{TR}_{21} \\ \overline{TR}_{22} \end{bmatrix} - \begin{bmatrix} TR_{21} \\ TR_{22} \end{bmatrix}}{2} = \frac{\begin{bmatrix} S_{12} + S_{21} \\ S_{11} + S_{22} \end{bmatrix} - \begin{bmatrix} S_{12} - S_{21} \\ S_{11} - S_{22} \end{bmatrix}}{2}$ \overline{TR}_{11} and \overline{TR}_{21} are acquired aliased images from time series. \overline{TR}_{12} and \overline{TR}_{22} are artificial aliased calibration images.
mSPECS-VAT	A. Calibration Images 	B. Acquired Aliased Time Series 
	C. Sagittal View of Time Series  $TR_1 = Slice_1 + Slice_2 + \epsilon$ $TR_2 = Slice_1 - Slice_2 + \epsilon$	D. Separation Process $\begin{bmatrix} \widehat{S}_{11} \\ \widehat{TR}_{12} \\ \widehat{S}_{12} \end{bmatrix} = \frac{\begin{bmatrix} TR_{11} \\ TR_{12} \end{bmatrix} + \begin{bmatrix} \overline{TR}_{11} \\ \overline{TR}_{12} \end{bmatrix}}{2} = \frac{\begin{bmatrix} S_{11L} + S_{21R} \\ S_{12L} + S_{22R} \end{bmatrix} + \begin{bmatrix} S_{11L} - S_{21R} \\ S_{12L} - S_{22R} \end{bmatrix}}{2}$ $\begin{bmatrix} \widehat{S}_{21} \\ \widehat{TR}_{22} \\ \widehat{S}_{22} \end{bmatrix} = \frac{\begin{bmatrix} \overline{TR}_{21} \\ \overline{TR}_{22} \end{bmatrix} - \begin{bmatrix} TR_{21} \\ TR_{22} \end{bmatrix}}{2} = \frac{\begin{bmatrix} S_{11R} + S_{21L} \\ S_{12R} + S_{22L} \end{bmatrix} - \begin{bmatrix} S_{11R} - S_{21L} \\ S_{12R} - S_{22L} \end{bmatrix}}{2}$ \overline{TR}_{11} and \overline{TR}_{21} are acquired aliased images from time series. \overline{TR}_{12} and \overline{TR}_{22} are artificial aliased calibration images. The $S_{i,j,k}$ denotes the i^{th} slice, j^{th} part, and k denotes the direction of horizontal image shift (Left or Right).
	A. Calibration Images 	B. Acquired Aliased Time Series 
	C. Sagittal View of Time Series  $TR_1 = Slice_1 + Slice_2 + \epsilon$ $TR_2 = Slice_1 - Slice_2 + \epsilon$	D. Separation Process $\begin{bmatrix} \widehat{S}_{11} \\ \widehat{TR}_{12} \\ \widehat{S}_{12} \end{bmatrix} = \frac{\begin{bmatrix} TR_{11} \\ TR_{12} \end{bmatrix} + \begin{bmatrix} \overline{TR}_{11} \\ \overline{TR}_{12} \end{bmatrix}}{2} = \frac{\begin{bmatrix} S_{11L} + S_{22R} \\ S_{12L} + S_{21R} \end{bmatrix} + \begin{bmatrix} S_{11L} - S_{22R} \\ S_{12L} - S_{21R} \end{bmatrix}}{2}$ $\begin{bmatrix} \widehat{S}_{21} \\ \widehat{TR}_{22} \\ \widehat{S}_{22} \end{bmatrix} = \frac{\begin{bmatrix} \overline{TR}_{21} \\ \overline{TR}_{22} \end{bmatrix} - \begin{bmatrix} TR_{21} \\ TR_{22} \end{bmatrix}}{2} = \frac{\begin{bmatrix} S_{12R} + S_{21L} \\ S_{11R} + S_{22L} \end{bmatrix} - \begin{bmatrix} S_{12R} - S_{21L} \\ S_{11R} - S_{22L} \end{bmatrix}}{2}$ \overline{TR}_{11} and \overline{TR}_{21} are acquired aliased images from time series. \overline{TR}_{12} and \overline{TR}_{22} are artificial aliased calibration images. The $S_{i,j,k}$ denotes the i^{th} slice, j^{th} part, and k denotes the direction of horizontal image shift (Left or Right).

Figure 2.3: The data-acquiring process of the mSPECS technique (without any image shifts), the mSPECS-CAIPIRINHA technique (shift vertically), the mSPECS-VAT technique (shift horizontally), and the mSPECS-CAIPIVAT technique (shift vertically and horizontally).

any image shifts), the mSPECS-CAIPIRINHA technique, the mSPECS-VAT technique and the mSPECS-CAIPIVAT technique.

2.2 The Bootstrap Sampling and Artificial Aliasing of Calibration Images

In the previous simultaneous multi-slice (SMS) study, bootstrap sampling and artificial aliasing of calibration reference image techniques have been proven as powerful tools to support the separation and reconstruction process of aliased images. By increasing the size of the aliasing matrix and adding a regularizer into the least square estimation function, the correlation induced by the separation process will decrease and the slice-to-slice signal leakage eliminated. In the fMRI time series, for each excitation, N_s bootstrap sampled coil slice images are randomly chosen from fully sampled calibration reference images. The mean calibration image is calculated for each slice and is artificially aliased, which is then repeated for each TR.

Given a single TR, the calibration images will have the same shift pattern as acquired images, thus, the total number of different combinations for different voxels should be N_s , which is equal to the rank of the chosen Hadamard matrix. After removing the combination of the acquired aliasing pattern from the full voxel combination pattern, $N_s - 1$ different combinations remain. Therefore, for a single excitation, a voxel across N_s slices, measured through N_c coils, ν , can be represented as a vector with the dimension of $2N_s N_c (N_s - 1) \times 1$ with the real component stacked on the top of the imaginary component, corresponding to the remaining combinations without the acquired aliasing combination. The mean bootstrap sampled voxel, $\bar{\nu}$, is the same dimension as ν for each time point. The artificial aliasing calibration images, ν , across N_s slices measured through N_c coils at N_α sequential time point can be expressed as:

$$\nu = C\bar{\nu} = C_A\mu + C\eta. \quad (2.11)$$

The dimension of the measurement error vector, η , is the same size as the vector

ν . The mean of the measurement error for the calibration images is $E(\eta) = 0$, and the covariance is $cov(C\eta) = \tau^2 I_{2N_c N_\alpha (N_s - 1)}$, where $I_{2N_c N_\alpha (N_s - 1)}$ is the identity matrix. It is assumed that there is no correlation between the real and imaginary components of the calibration images, and no correlation between coils. The true voxel value vector, μ , is constructed with the real and imaginary components of the calibration voxel with the dimension $2N_s \times 1$. The artificial aliasing matrix, C_A , is following the same aliasing rules as acquired images do, rotating by the matrix rotation operation and multiplying the Hadamard encoding aliasing coefficients. Due to the combination of acquired aliasing voxel removed from the full combinations, the dimension of the artificial aliasing matrix is $2N_c N_\alpha (N_s - 1) \times 2N_s$. Same as the assumption in the acquired aliasing images, we assign $N_r = N_s$ to improve the computational efficiency. For example, considering a situation with $N_s = 4$ and $N_r = 4$, for each time point, $N_s - 1 = 3$ combinations should be applied for the calibration images. Thus, for a given excitation, the δ th Hadamard aliasing pattern and γ th matrix rotating operation, the aliasing matrix $(C_A)_{\gamma,\delta}$ across N_c coils is:

$$(C_A)_{\gamma,\delta} = \left[\overline{H_{\delta,1} R_{\gamma,1}} \begin{pmatrix} S_{1,1} \\ \vdots \\ S_{N_c,1} \end{pmatrix}, \dots, \overline{H_{\delta,N_c} R_{\gamma,N_c}} \begin{pmatrix} S_{1,N_s} \\ \vdots \\ S_{N_c,N_s} \end{pmatrix} \right]. \quad (2.12)$$

The notation \overline{HR} denotes the remaining combination for the Hadamard encoding aliasing pattern with the matrix rotation pattern after removing the combination of the acquired aliasing pattern. Incorporating N_α sequential time points, the artificial aliasing matrix, C_A , is:

$$C_A = \left[(C_A)_1, \dots, (C_A)_{N_\alpha} \right]'. \quad (2.13)$$

Thus, the prior distribution of the artificial aliased calibration voxel is:

$$P(\nu \mid C_A, \mu, \tau^2) \propto (\tau^2)^{-\frac{2N_c N_\alpha (N_s - 1)}{2}} \exp \left[-(\nu - C_A \mu)' (\nu - C_A \mu) / (2\tau^2) \right]. \quad (2.14)$$

The Equation 2.6 and Equation 2.11 can be combined together, which will generate:

$$y = \begin{bmatrix} a \\ \nu \end{bmatrix} = \begin{bmatrix} X_A \beta \\ C_A \mu \end{bmatrix} + \begin{bmatrix} \varepsilon \\ C \eta \end{bmatrix}. \quad (2.15)$$

Based on the previous section, the covariance for the acquired aliasing measurement error is $cov(\varepsilon) = \sigma^2 I_{2N_c N_\alpha}$, and the covariance for the artificial aliasing measurement error is $cov(C\eta) = \tau^2 I_{2N_s N_c (N_s - 1)}$, the covariance for vector, y , consisting of the acquired aliasing voxel value and the artificial aliasing voxel value is:

$$cov(y) = \begin{bmatrix} \sigma^2 I_{2N_c N_\alpha} & 0 \\ 0 & \tau^2 I_{2N_s N_c (N_s - 1)} \end{bmatrix}. \quad (2.16)$$

Without the support of the bootstrapping technique, there is no variation in the artificial aliasing calibration images, i.e. the same calibration reference images is artificially aliased for each TR, which will lead to $\tau^2 = 0$. However, by applying the bootstrapping technique, for each excitation, the N_s calibration images are randomly selected and averaged to obtain $\bar{\nu}$, and hence $\tau^2 = \sigma^2$. Thus, the covariance for vector, y , is:

$$cov(y) = \sigma^2 I_{2N_c N_\alpha N_s}. \quad (2.17)$$

2.3 The Prior Distribution

In Chapter 1.3, we discussed the prior distribution can be observed from the artificial aliasing of the calibration images. To estimate the reconstructed voxel value separated from the aliased slices, the voxels β are specified to have a normal prior distribution $\beta \sim N(\mu, \sigma^2 (C'_A C_A)^{-1})$, therefore:

$$P(\beta \mid \sigma^2, \mu, C_A) \propto (\sigma^2)^{-\frac{2N_s N_r}{2}} \exp \left[-(\beta - \mu)' (C'_A C_A) (\beta - \mu) / (2\sigma^2) \right]. \quad (2.18)$$

The measurement error variance σ^2 is specified to have an inverse gamma prior distribution:

$$P(\sigma^2 | \lambda, \delta) \propto (\sigma^2)^{-(\lambda+1)} \exp[-\delta/\sigma^2], \quad (2.19)$$

where hyperparameters μ , λ and δ are assessed from the pre-scan calibration images.

2.4 The Hyperparameters Assessment

Following the complex-valued Bayesian process discussed in Chapter 1.3, the unknown hyperparameters can be assessed using the prior calibration images. In the image acquisition process of the mSPECS-CAIPIVAT model, two series of brain images from two different fMRI experiments are acquired: the calibration images and the aliased images. The aliased images correspond to the mSPECS-CAIPIVAT model, whereas the calibration images, on the other hand, are obtained using the traditional method without any image shift techniques or acceleration factors. Thus, the calibration images can be treated as prior information, and hyperparameters can be estimated from them. According to our Bayesian mSPECS-CAIPIVAT model, to estimate the voxel value β , we need to estimate the hyperparameters μ , λ , and δ . In Equation 2.18, the artificial aliasing matrix C_A is known information and it strictly follows the artificial aliasing rules in Chapter 2.2. The hyperparameter μ represents the averaged voxel value after the bootstrap resampling process, and its estimation is described in detail in Chapter 2.2. The hyperparameters λ and δ are the shape parameter and the scale parameter of the inverse-gamma distribution and we can assess them from calibration images. As discussed in the Chapter 2.2, for each excitation, N_s brain images will be randomly chosen from the fully sampled calibration images and averaged to assess hyperparameter μ . Moreover, the calibration reference images can be utilized to estimate sample noise variance σ_0^2 . Therefore, the hyperparameters μ , λ and δ can be assessed by $\mu = \bar{\nu}$, $\lambda = n_0$ and $\delta = (n_0 - 1)\sigma_0^2$, where n_0 is the number of calibration images and σ_0^2 is sample noise variance.

2.5 The Posterior Estimation

Following Chapter 2.3 and Chapter 2.4, the joint posterior distribution for the voxel values β and the noise variance σ^2 can be obtained by combining the likelihood equation (Equation 2.9), the prior distribution of β (Equation 2.18) and the prior distribution of σ^2 (Equation 2.19) together along with algebra to become:

$$P(\beta, \sigma^2 | \cdot) \propto (\sigma^2)^{-\frac{p}{2}} \exp \left[-((\beta - \hat{\beta}_{MPM})'(X'_A X_A + C'_A C_A)(\beta - \hat{\beta}_{MPM}) + w)/(2\sigma^2) \right], \quad (2.20)$$

where $p = 2N_c N_\alpha + 2N_s N_r - 2\lambda - 2$, and $w = a'a + \mu' C'_A C_A \mu - (X'_A a + C'_A C_A \mu)' (X'_A X_A + C'_A C_A)^{-1} (X'_A a + C'_A C_A \mu) + 2\delta$. After integration, the marginal posterior distribution of estimate voxel value β is a student-t distribution $\beta \sim t(\nu^*)$:

$$f(\beta | \cdot) \propto \left\{ 1 + \frac{1}{\nu^*} (\beta - \hat{\beta}_{MPM})' \left[\frac{(X'_A X_A + C'_A C_A)}{\tau^2} \right] (\beta - \hat{\beta}_{MPM}) \right\}^{\frac{\nu^*+1}{2}}, \quad (2.21)$$

with $\nu^* = p - 1$ and $\tau^2 = w/\nu^*$. The marginal posterior mean (MPM) for $\hat{\beta}$ is:

$$E(\beta | \cdot) = \hat{\beta}_{MPM} = (X'_A X_A + C'_A C_A)^{-1} (X'_A a + C'_A C_A \mu). \quad (2.22)$$

The matrix $C'_A C_A$ acts as a regularizer for the matrix inverse to improve the condition of the equation. Since the true voxel value from calibration images is close to the true voxel value from acquired aliased images, Equation 2.22 leads to $E(\beta | \cdot) = \beta$. The marginal posterior covariance of the voxel value $\hat{\beta}$ is:

$$cov(\beta | \cdot) = \frac{\nu^*}{\nu^* - 2} \tau^2 (X'_A X_A + C'_A C_A)^{-1}. \quad (2.23)$$

The covariance of the voxel value $\hat{\beta}$ is diagonal due to the structure of the design matrix. As a results, the separated voxel values are uncorrelated, meaning that there will not be signal leakage between slices. Moreover, the marginal posterior distribution

of σ^2 is an inverse gamma distribution, $\sigma^2 \sim IG(\gamma, w/2)$:

$$f(\sigma^2 | \cdot) \propto (\sigma^2)^{-\frac{p}{2}-1} \exp[-w/(2\sigma^2)], \quad (2.24)$$

with $\gamma = (p - 1)/2$. The MPM of the noise variance σ^2 is:

$$E(\sigma^2 | \cdot) = \frac{w/2}{\gamma}, \quad (2.25)$$

and the marginal posterior variance of the noise variance is:

$$\text{var}(\sigma^2 | \cdot) = \frac{w/2}{(\gamma - 1)^2(\gamma - 2)}. \quad (2.26)$$

CHAPTER 3: A BAYESIAN APPROACH OF MSPECS-IPA-CAIPIVAT

In this chapter, to further reduce the total image scan time, we introduce a novel SMS image reconstruction technique called “a controlled aliasing in parallel imaging with view angle tilting approach and in-plane acceleration method for multi-coil separation of parallel encoded complex-valued slices” (mSPECS-IPA-CAIPIVAT) in a complex-valued Bayesian manner. This novel SMS technique combines in-plane acceleration technique and through-plane acceleration technique, hence the total image acquisition time further reduced compared with the mSPECS-CAIPIVAT model discussed in Chapter 2. This approach builds upon the mSPECS-IPA method by integrating both TPA and IPA acceleration techniques into a unified 2D acceleration technique (Kociuba (2016)). By leveraging 2D acceleration, a higher overall acceleration factor can be achieved, with the net acceleration equal to the product of the TPA and IPA factors. In this novel image reconstruction method, we incorporate an image shift technique into the model to reduce the similarity of coil sensitivity information for aliased voxels, thereby improving image reconstruction accuracy.

3.1 The Data Acquiring Process in mSPECS-IPA-CAIPIVAT

3.1.1 Image Shift Techniques in mSPECS-IPA-CAIPIVAT

As discussed in Chapter 1.1, the SMS technique enables the concurrent acquisition of multiple brain slice images, reducing the total volume scan time depending on the selected TPA factor. Unlike single-slice acquisition, multi-slice acquisition results in a short physical distance between aliased images. When applying the SENSE algorithm to reconstruct brain images and capture activity signals, an ill-conditioned matrix problem arises due to the high similarity of coil sensitivity information between closely spaced aliased voxels. Consequently, strong inter-slice signals and anatomical structures from other slices may appear as artifacts in the reconstructed images.

To eliminate those wrong anatomical artifacts from other slices on the reconstructed brain images, decreasing the similarity of the coil sensitivity information is the primary strategy. Therefore, we introduced the images shift techniques to artificially increase the physical distance between aliased images. To assess the performance of the image reconstruction method at high acceleration factors, we define the noise amplification factor, also known as the geometry factor (g -factor), as described in (Pruessmann (2004); Setsompop et al. (2012); Welvaert and Rosseel (2013)):

$$g_{SMS} = \frac{SNR_{full}}{SNR_{accelerate}\sqrt{R}}. \quad (3.1)$$

In equation 3.1, SNR_{full} is the signal-to-noise (SNR) ratio for the reconstructed images from techniques without acceleration factors and image shift techniques, and it can be assessed from the calibration images. $SNR_{accelerate}$ is the SNR value for the reconstructed images with acceleration factors, and the IPA acceleration factor R indicates the omission of spatial frequency data along the phase encoding direction. The closer the value of g_{SMS} is to 1, the better the reconstruction quality of the accelerated method. According to equation 3.1, high similarity of coil sensitivity information induces the high g_{SMS} value, which leads to a reduction of the $SNR_{accelerate}$ ratios for the reconstructed images. Thus, to increase the $SNR_{accelerate}$ value and improve the performance of the novel acceleration technique, three image shift techniques discussed in Chapter 1.2 have been incorporated.

3.1.2 The 2D Hadamard Phase Encoding

As discussed in Chapter 2.1.2 the traditional Hadamard encoding technique is a well-developed volume-image method and widely used in fMRI studies (Souza et al. (1988)). The conventional magnetic resonance (MR) imaging techniques have been limited by the size of the matrix for the acquired aliased images. The traditional Hadamard phase encoding method allows the increment of the size of the acquired

aliased image matrix by aliasing in both frequency and phase encoding dimensions. With the support of this simultaneous binary-encoded technique, multiple slices can be acquired concurrently for each excitation, enabling the implementation of SMS. As a result, the repetition time (TR) is reduced, and the *SNR* is improved. The Hadamard matrix is given by:

$$H_{2^n} = \begin{bmatrix} H_{2^{n-1}} & H_{2^{n-1}} \\ H_{2^{n-1}} & -H_{2^{n-1}} \end{bmatrix} = H_2 \otimes H_{2^{n-1}}, \text{ where } H_1 = \begin{bmatrix} 1 \end{bmatrix}, H_2 = \begin{bmatrix} 1 & 1 \\ 1 & -1 \end{bmatrix}, \quad (3.2)$$

where \otimes denotes the Kronecker product. It is an orthogonal and full rank matrix with elements of either +1 or -1. In this study, since the TPA approach and the IPA approach are combined to further decrease the total image scan time, and the image shift techniques are incorporated to decrease the influences of the geometry properties, we introduce a novel 2D Hadamard phase encoding technique to our approach. The novel 2D Hadamard phase encoding technique is developed and based upon the Hadamard phase encoding technique with elements of either +1 or -1. However, different from the traditional Hadamard phase encoding technique, in order to guarantee the orthogonality property for each aliased image, different 2D Hadamard coefficients will be assigned to different segments for different slices. Figure 3.1 shows the 2D Hadamard phase encoding aliasing coefficient for $N_s = 2$ and $N_s = 4$ situations, where N_s is the number of aliased slices for each excitation. First, for each excitation or each TR, the through-plane Hadamard coefficient will be assigned to different slices. Second, for each segment of each slice, the in-plane Hadamard coefficient will be assigned to a different excitation. To maintain the orthogonality property for each segment of each slice, the in-plane Hadamard coefficient starts from the second column of the Hadamard coefficient for the first excitation. At the last TR of the cycle, the in-plane Hadamard coefficient is the first column of the Hadamard matrix. Finally, the 2D Hadamard coefficient will be the product of the through-plane and

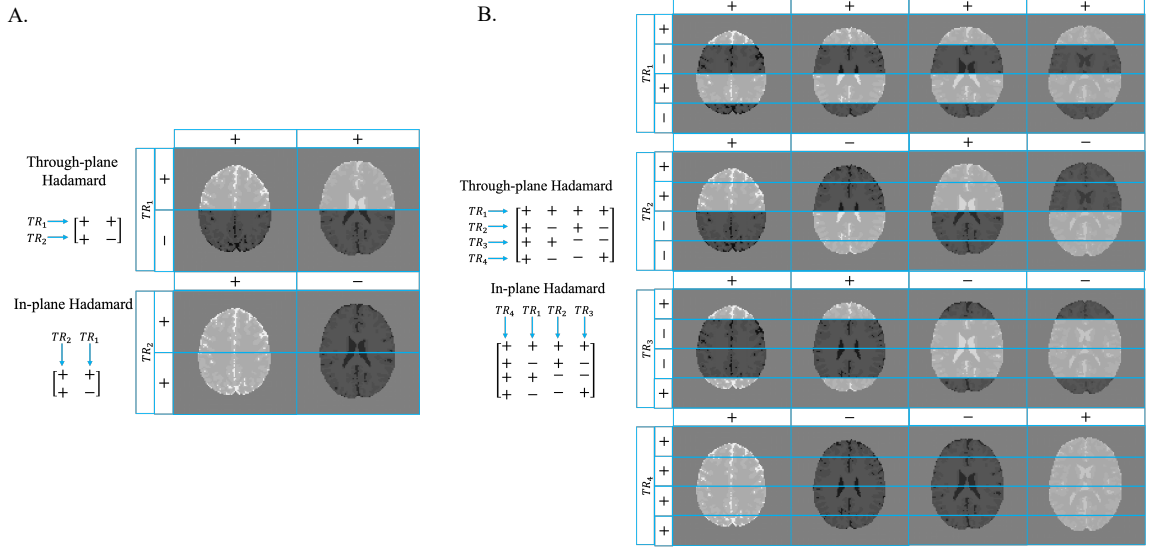


Figure 3.1: A. The 2D Hadamard phase encoding coefficient for $N_s = 2$. B. The 2D Hadamard phase encoding coefficient for $N_s = 4$.

in-plane Hadamard coefficient for each segment of each slice and each excitation. The size of the in-plane and through-plane Hadamard coefficient matrix is equal to the number of aliased slices, N_s , for each excitation.

3.1.3 The Combination of Image Shift Techniques and 2D Hadamard Phase Encoding

To accomplish the goal of decreasing the coil sensitivity information similarity of aliased voxels, and thus decreasing the influence of the g -factor, we combined the image shift techniques and the 2D Hadamard phase encoding technique together. Figure 3.2 shows the image shift situation corresponding to different SMS techniques for the first 4 TRs along with the 2D Hadamard coefficients for each segment of the slices under the circumstance with $N_s = 4$. Compared with the mSPECS-IPA method (Figure 3.2A), the other three methods are incorporating with different image shift directions and amount for each slices and each excitation. Figure 3.2B shows the image shift situation along with the 2D Hadamard coefficients incorporating with the mSPECS-IPA-CAIPIRINHA method. For each slice within each

TR, a $\Delta y = (l - 1)FOV/N_s$ of in-plane image shift on the vertical direction will be implied, where $l = 1, \dots, N_s$. For each excitation, a $\Delta y = (m - 1)FOV/N_s$ of in-plane image shift on the vertical direction will be implied, where $m = 1, \dots, N_s$. Thus, with the in-plane and the through-excitation CAIPIRINHA image shift, the voxel aliasing situation at $TR_{N_s} + 1$ will be identically same as aliasing situation at TR_1 . Figure 3.2C shows the image shift situation along with the two-dimensional Hadamard coefficients incorporating with the mSPECS-IPA-VAT method. Unlike the mSPECS-IPA-CAIPIRINHA method, the mSPECS-IPA-VAT method only shift the image along the horizontal direction. Thus, for each excitation and each slice, no image shift happens along the vertical direction, but a modest amount of image shift will be applied for each slice and each excitation along the horizontal direction. Furthermore, similar to the mSPECS-IPA-CAIPIRINHA method, the voxel aliasing situation at time point $TR_{N_s} + 1$ will be same as the voxel aliasing situation at time point TR_1 . Figure 3.2D shows voxel aliasing situation incorporated with the mSPECS-IPA-CAIPIVAT method. Since the mSPECS-IPA-CAIPIVAT method is combining the principle idea of mSPECS-IPA-CAIPIRINHA and mSPECS-IPA-VAT method together, the image shift will happen along the vertical and the horizontal direction. For each slice within each excitation, a $\Delta y = (l - 1)FOV/N_s$ amount of the image shift along the vertical direction, where $l = 1, \dots, N_s$, and the amount of the image shift technique corresponding to the VAT technique along the horizontal direction will be implied. Moreover, for each excitation, a $\Delta y = (m - 1)FOV/N_s$ of through-excitation image shift will be implied along the vertical direction, where $m = 1, \dots, N_s$. Same as the other three methods, at time point $TR_{N_s} + 1$, the voxel aliasing situation will be identical as time point TR_1 . Comparing these four image shift techniques, the overlapping area between summed slices are decreasing from the mSPECS-IPA method to the mSPECS-IPA-CAIPIVAT method. However, since the novel proposed SMS technique is aiming at combining TPA and IPA technique

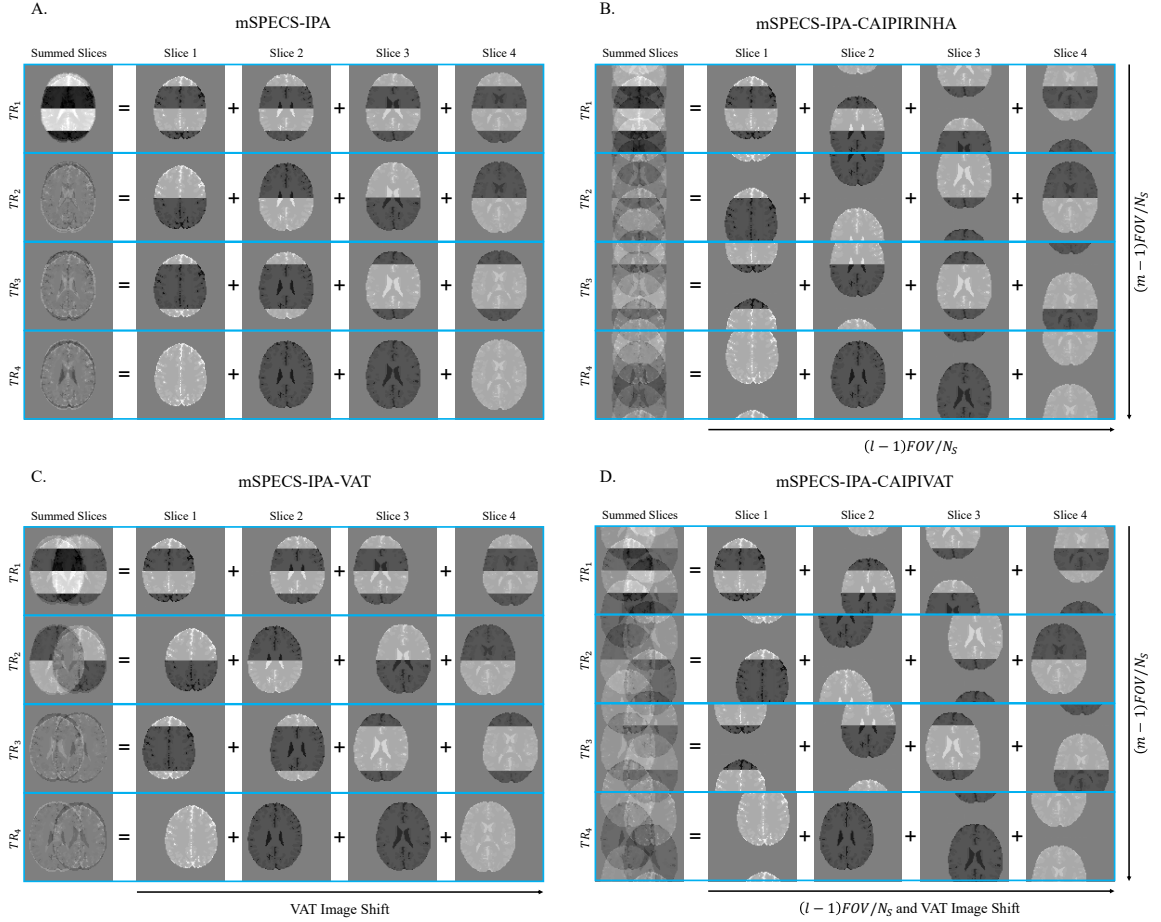


Figure 3.2: The voxel aliasing situation for the first 4 TRs with $N_s = 4$ circumstance incorporating with A. mSPECS-IPA image shift technique, B. mSPECS-IPA-CAIPIRINHA technique, C. mSPECS-IPA-VAT technique, and D. mSPECS-IPA-CAIPIVAT technique.

together, thus, making the voxel aliasing situation clear after the IPA technique is another vital process to discuss in this paper.

Figure 3.3 displays the voxel aliasing situation after the IPA aliasing technique for mSPECS-IPA, mSPECS-IPA-CAIPIRINHA, mSPECS-IPA-VAT, and mSPECS-IPA-CAIPIVAT technique under the circumstance with $N_s = 4$. In Figure 3.3, those dots in the same color indicating voxels are aliased together. From Figure 3.3, for the top two methods, mSPECS-IPA and mSPECS-IPA-CAIPIRINHA, four voxels at the same position are aliased together, whereas for the bottom two methods, only two

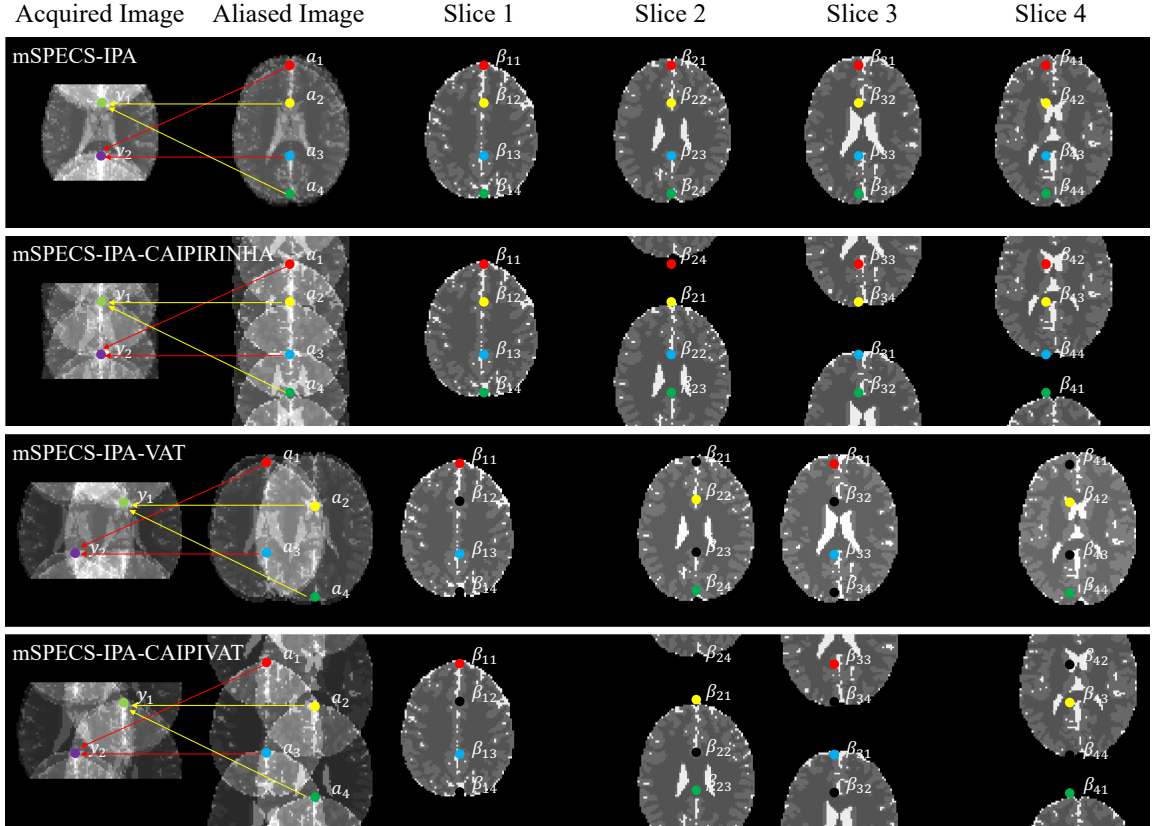


Figure 3.3: The voxel aliasing situation with $N_s = 4$ for mSPECS-IPA, mSPECS-IPA-CAIPIRINHA, mSPECS-IPA-VAT and mSPECS-IPA-CAIPIVAT technique.

voxels at the same position are aliased together. Moreover, comparing the mSPECS-IPA and the mSPECS-IPA-CAIPIRINHA method, after the IPA acceleration technique, the mSPECS-IPA-CAIPIRINHA has the more complex aliasing artifacts and the overlapping area is larger than the mSPECS-IPA method especially at the center part of the acquired images. Comparing the bottom two methods, mSPECS-IPA-VAT and the mSPECS-IPA-CAIPIVAT technique, the similar conclusion can be made.

3.1.4 A Single Aliased Voxel

Given an excitation δ in the fMRI time series, we define $IS_{\delta,z}$ notation indicating the image shift pattern for the z th slice and the δ th TR, corresponding to one of the mSPECS-IPA, mSPECS-IPA-CAIPIRINHA, mSPECS-IPA-VAT and the mSPECS-IPA-CAIPIVAT technique, and it follows the definition in Chapter 3.1.1. Thus, for

a single aliased voxel at the location (x, y) of the acquired aliased images with TPA and IPA acceleration techniques, corresponding to the 2D Hadamard coefficients at time point δ , measured at j th coil, is defined as the summation equation:

$$a_{j,\delta} = \sum_{k=1}^{IPA} \sum_{z=1}^{N_s} H_{\delta,z,k} S_{IS_{\delta,z,k}} \beta_{IS_{\delta,z,k}} + \varepsilon_{j,\delta}. \quad (3.3)$$

In equation 3.3, the acquired aliased voxel value $a_{j,\delta}$ is a complex-valued data with real and imaginary component, $a_C = a_R + ia_I$, and parameter k is the IPA indicator. The 2D Hadamard coefficient, $H_{\delta,z,k}$, is a real-valued orthogonal matrix corresponding to the δ th excitation, z th slice and the k th IPA process, and it strictly follows the definition of the 2D Hadamard phase encoding in Chapter 3.1.2. All of the element of the $H_{\delta,z,k}$ coefficient matrix is either +1 or -1. The coil sensitivity information matrix, $S_{IS_{\delta,z,k}}$, is a complex-valued data point with real and imaginary component, $S_C = S_R + iS_I$, corresponding to the k th IPA process and the image shift process at δ th excitation and z th slice. The true voxel value, $\beta_{IS_{\delta,z,k}}$, is a complex-valued data point with real and imaginary component, $\beta_C = \beta_R + i\beta_I$, corresponding to the k th IPA process and the image shift process at δ th excitation and z th slice. The measurement error, $\varepsilon_{j,\delta}$, is also a complex-valued data point with real and imaginary component, $\varepsilon_C = \varepsilon_R + i\varepsilon_I$, corresponding to the δ th time point and j th coil. Moreover, the real and imaginary component of measurement error is specified to be a normal distribution with mean $E(\varepsilon_R, \varepsilon_I) = 0$ and variance $var(\varepsilon_R, \varepsilon_I) = \sigma^2$.

Considering the acquired aliased voxel in equation 3.3 across total N_c coils, N_α time points and the N_s slices in the whole fMRI time series, the real-valued isomorphic representation of equation 3.3 can be expressed similar to equation 1.1:

$$a = X_A \beta + \varepsilon. \quad (3.4)$$

In equation 3.4, $a = [a_R; a_I]$ is a real-valued vector with dimension $2N_cN_\alpha \times 1$. The real-valued aliasing matrix $X_A = [(X_A)_R, -(X_A)_I; (X_A)_I, (X_A)_R]$ is known prior information including the 2D Hadamard coefficients and the coil sensitivity information across the N_c coils, N_α time points and the N_s slices. Thus, the dimension of the aliasing matrix X_A is $2N_cN_\alpha \times 2N_s$. For the δ th excitation, the known aliasing matrix $(X_A)_\delta$ across N_c coils and N_s slices is defined as:

$$(X_A)_\delta = \left[H_{\delta,1} \begin{pmatrix} S_{1,1} \\ \vdots \\ S_{N_c,1} \end{pmatrix}, \dots, H_{\delta,N_c} \begin{pmatrix} S_{1,N_s} \\ \vdots \\ S_{N_c,N_s} \end{pmatrix} \right]. \quad (3.5)$$

Across the N_α excitations, the equation 3.5 can be expressed as:

$$X'_A = \left[(X_A)'_1, \dots, (X_A)'_{N_\alpha} \right]. \quad (3.6)$$

The true voxel value in equation 3.4, $\beta = [\beta_R; \beta_I]$, is a vector we want to estimate, with dimension $2N_s \times 1$. The measurement error in equation 3.4, $\varepsilon = [\varepsilon_R; \varepsilon_I]$ has the same dimension as the a vector. The real and imaginary component of the measurement error is specified to be normal distributed with mean $E(\varepsilon) = 0$ and covariance $cov(\varepsilon) = \sigma^2 I_{2N_cN_\alpha}$, where $I_{2N_cN_\alpha}$ is the identity matrix.

Thus, in order to separate the aliased images and estimate the true voxel value for each slice, the maximum likelihood estimation in equation 1.4 can be applied and the estimated voxel value, $\hat{\beta}_{MLE}$, can be calculated by:

$$\hat{\beta}_{MLE} = \left(X'_A X_A \right)^{-1} X'_A a. \quad (3.7)$$

Moreover, the covariance of the voxel value $\hat{\beta}$, can be estimated by:

$$\text{cov}(\hat{\beta}_{MLE}) = \sigma^2 \left(X'_A X_A \right)^{-1}. \quad (3.8)$$

According to the methodology of the combination of image shift techniques and the 2D Hadamard phase encoding technique, the novel proposed SMS method accelerates the image acquiring process along the TPA and the IPA dimension. However, the relative short scan time leads to the less data information collected during the image acquiring process compared with the traditional imaging technique without acceleration techniques. Furthermore, it also leads to the ill-condition of the designed aliasing matrix which will cause failure to calculate the inverse of $X'_A X_A$. Thus, coming up with a technique that is capable to fix the ill-condition designed matrix problem and hence calculate the inverse problem is the next priority. In this study, we introduced the bootstrap sampling technique along with the artificial aliasing of the calibration images technique to solve this problem. By applying these two techniques into the novel image shift SMS technique, the designed aliasing matrix is made to be full rank and invertible and the inter-slice signal leakage can be eliminated.

3.2 The Bootstrap Sampling and Artificial Aliasing of Calibration Images

Based on the discussion in the previous chapters, to make the designed aliasing matrix to be full rank and invertible, slices information from the calibration images can be utilized as the reference information. The bootstrap sampling technique is a widely used tool which can decrease the correlation induced by the image separation process and eliminate the inter-slice signal leakage. In the image separation process, for each excitation, the bootstrap sampling technique will be applied to the calibration images. The bootstrapping size for each excitation is related to the TPA factor, which is equal to the number of aliased sliced for each excitation and the IPA factor. Thus, for each excitation in the fMRI time series, $N_s R$ bootstrapped sampled slices will be

randomly chosen from the fully sampled calibration image time series. The randomly chosen slices will be averaged and the mean calibration images will be utilized for the artificial aliasing process.

For each excitation, the same image shift pattern will be applied to both acquired aliased images and the artificial aliased calibration images. But different 2D Hadamard aliasing coefficient matrix will be applied to acquired aliased images and the artificial aliased calibration images. Figure 3.4 shows the 2D Hadamard aliasing coefficient for acquired aliased slices (red box) and the artificial aliased calibration slices (blue box) for the first 4 TRs with $N_s = 4$. For each segment of each slice, the white part means the Hadamard coefficient is +1, and the black part means the Hadamard coefficient is -1. Moreover, the 2D Hadamard aliasing coefficient for acquired aliased slices and artificial aliased calibration slices at time point TR_{N_s+1} will be identical as TR_1 . Based on the 2D Hadamard aliasing coefficients for acquired aliased slices and the artificial aliased calibration slices, for each excitation, $N_s - 1$ combinations of 2D Hadamard aliasing coefficient remain for the artificial aliasing process.

Similar to equation 3.4, for a single excitation, a single voxel, ν , from the artificial aliasing calibration aliased slices located at (x, y) across N_s slices, measured through N_c coils can be expressed as:

$$\nu = C\bar{\nu} = C_A\mu + C\eta. \quad (3.9)$$

In equation 3.9, the artificial aliased voxel value, $\nu = [\nu_R; \nu_I]$, is a vector with real and imaginary component and dimension $2N_s N_c (N_s - 1) \times 1$. The mean bootstrap sampled voxel, $\bar{\nu} = [\bar{\nu}_R; \bar{\nu}_I]$, is a vector with dimension $2N_s \times 1$. The true calibration voxel value, $\mu = [\mu_R; \mu_I]$, and the measurement error, $\eta = [\eta_R; \eta_I]$, have the same dimension with the mean bootstrap sampled voxel vector. Moreover, the mean of

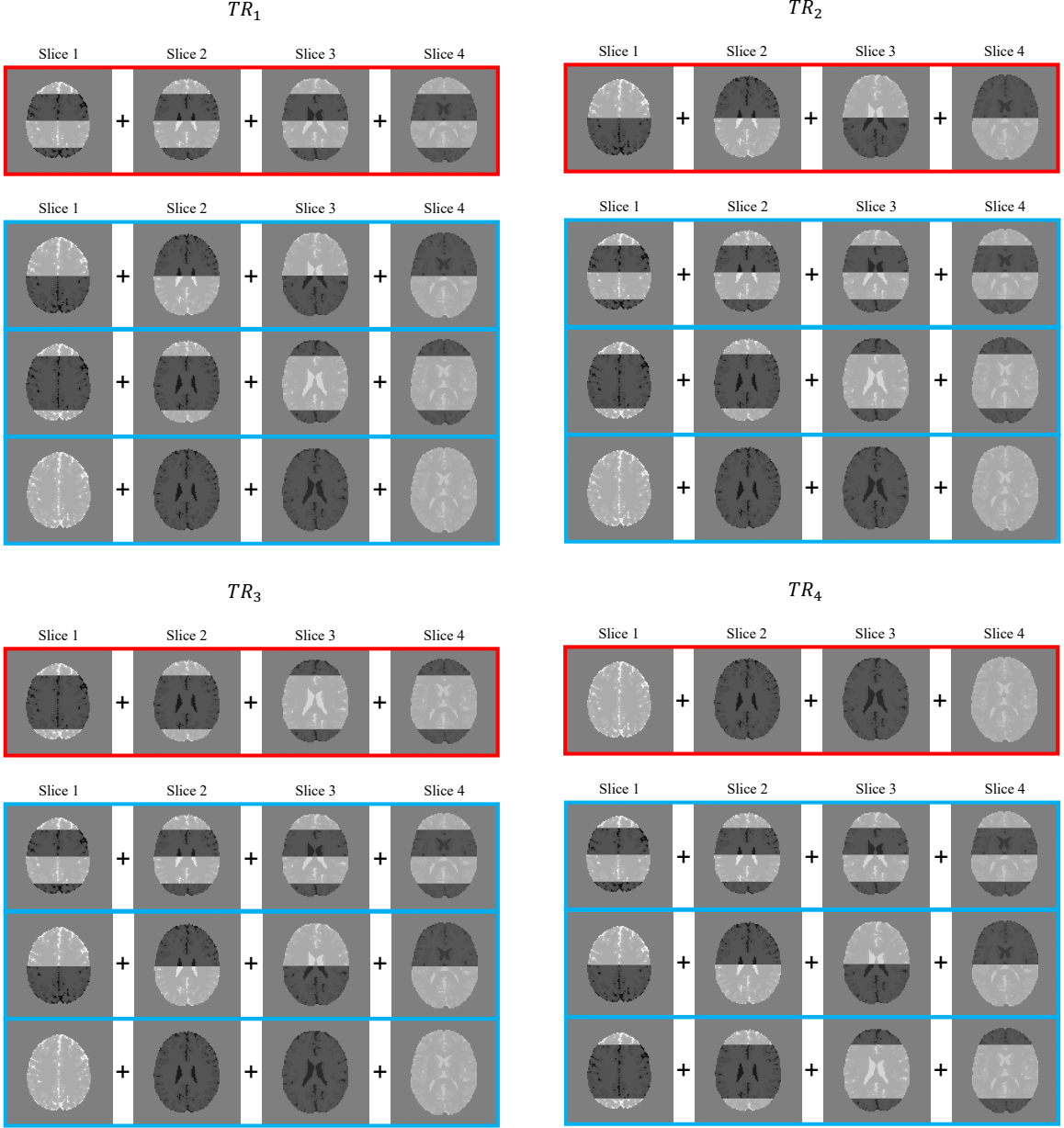


Figure 3.4: The the 2D Hadamard aliasing coefficients for acquired aliased slices (red box) and the artificial aliased calibration slices (blue box) for the first 4 TRs with $N_s = 4$.

the measurement error is $E(C\eta) = 0$ and covariance is $cov(C\eta) = \tau^2 I_{2N_s N_c (N_s - 1)}$ where $I_{2N_s N_c (N_s - 1)}$ is the identity matrix. If the bootstrap sampling technique does not incorporate, *i.e.* the same calibration images are keep using into the model, then the covariance of the measurement error is $\tau^2 = 0$, thus the correlation between the reconstructed slices is induced by the image separation process. However, under the

assistance of the bootstrap sampling technique, $\tau^2 = \sigma^2$, and the covariance of the measurement error of the calibration image is $cov(C\eta) = \sigma^2 I_{2N_s N_c (N_s - 1)}$.

The artificial aliasing matrix, C_A in equation 3.9, is a known prior information including the 2D Hadamard coefficients for the artificial aliasing slices and the coil sensitivity information across N_c coils, N_α time points and N_s slices. Thus, the dimension of the artificial aliasing matrix, C_A , is $2N_s N_c (N_s - 1) \times 2N_s$. For the δ th excitation, the known artificial aliasing matrix $(C_A)_\delta$ across N_c coils and N_s slices is defined as:

$$(C_A)_\delta = \left[\overline{H_{\delta,1}} \begin{pmatrix} S_{1,1} \\ \vdots \\ S_{N_c,1} \end{pmatrix}, \dots, \overline{H_{\delta,N_c}} \begin{pmatrix} S_{1,N_s} \\ \vdots \\ S_{N_c,N_s} \end{pmatrix} \right]. \quad (3.10)$$

The notation \overline{H} indicates the remaining 2D Hadamard aliasing coefficient for each excitation after removing the 2D Hadamard aliasing coefficient for the acquired aliased images. Across the N_α excitations, the equation 3.10 can be expressed as:

$$C'_A = \left[(C_A)'_1, \dots, (C_A)'_{N_\alpha} \right]. \quad (3.11)$$

3.3 The Likelihood, Prior, and Joint Distribution

As discussed in Chapter 1.3, the acquired aliased voxel values across the whole brain image are independent and identically distributed and the measurement error for each acquired aliased voxel is specified to be Gaussian distributed. Thus, the likelihood distribution (equation 1.3) of the acquired aliased voxel is:

$$P(a | X_A, \beta, \sigma^2) \propto (\sigma^2)^{-\frac{2N_c N_\alpha}{2}} \exp \left[-\frac{1}{2\sigma^2} (a - X_A \beta)' (a - X_A \beta) \right]. \quad (3.12)$$

Following the methodology of the Bayesian approach, the voxel value from calibration images can be utilized as prior information. Moreover, in Chapter 1.3 the voxel value, β , is specified to have a normal prior distribution. Therefore, the prior distribution of the voxel value $\beta \sim N(\mu, \sigma^2(C'_A C_A)^{-1})$:

$$P(\beta | C_A, \mu, \sigma^2) \propto (\sigma^2)^{-\frac{2N_s N_r}{2}} \exp \left[-\frac{1}{2\sigma^2} (\beta - \mu)' (C'_A C_A) (\beta - \mu) \right]. \quad (3.13)$$

Moreover, in Chapter 1.3, the variance of the measurement error, σ^2 is specified to have an inverse gamma prior distribution:

$$P(\sigma^2 | \lambda, \delta) \propto (\sigma^2)^{-(\lambda+1)} \exp \left[-\frac{\delta}{\sigma^2} \right], \quad (3.14)$$

where hyperparameters μ , λ and δ are assessed from the calibration images. The posterior distribution of the voxel value, β , and the variance of the measurement error, σ^2 , follows the joint distribution as equation 1.6:

$$P(\beta, \sigma^2 | \cdot) \propto P(a | X_A, \beta, \sigma^2) P(\beta | C_A, \mu, \sigma^2) P(\sigma^2 | \lambda, \delta). \quad (3.15)$$

3.4 The Hyperparameters Assessment

Before the image acquisition process of the novel proposed SMS model, a time series of calibration images will be collected first. The calibration image time series will be acquired through the traditional fMRI technique, and unlike the novel SMS model incorporating with different image shift techniques and 2D Hadamard aliasing coefficient. The calibration image time series is acquired without any image shift techniques or aliasing coefficient, no task experiment will be executed during this time series. As discussed in Chapter 3.3, the calibration images can be utilized as prior information, hence the unknown hyperparameters can be assessed from calibration

time series. In equation 3.15, the acquired aliasing matrix X_A and the artificial aliasing matrix C_A are known prior information that we do not need to assess from the calibration image time series. The hyperparameters μ , λ , and δ , on the other hand, need to be assessed from the calibration image time series. As discussed in Chapter 3.2, the hyperparameter μ is the averaged voxel value after the bootstrap resampling process. For each excitation in the time series, N_s brain images will be randomly chosen from the fully sampled calibration images and averaged to assess the hyperparameter averaged voxel value $\mu = \bar{\nu}$. The shape parameter λ and the scale parameter δ from inverse gamma distribution in equation 3.14, also need to be assessed from the calibration image time series. After the bootstrap resampling process, the sample noise variance σ_0^2 can be estimated from the calibration image time series. Thus, the shape parameter can be assessed by $\lambda = n_0$, and the scale parameter can be assessed by $\delta = (n_0 - 1)\sigma_0^2$, where n_0 is the number of calibration images and σ_0^2 is sample noise variance.

3.5 The Posterior Estimation

According to the discussion in Chapter 1.3, Chapter 3.3, and Chapter 3.4, the joint distribution (equation 3.15) of the likelihood distribution of acquired aliased (equation 3.12), the prior distribution of the voxel value β (equation 3.13), and the prior distribution of the noise variance σ^2 (equation 3.14) can be calculated after algebra:

$$P(\beta, \sigma^2 | \cdot) \propto (\sigma^2)^{-\frac{p}{2}} \exp \left[-\frac{1}{2\sigma^2} ((\beta - \hat{\beta}_{MPM})'(X_A'X_A + C_A'C_A)(\beta - \hat{\beta}_{MPM}) + w) \right], \quad (3.16)$$

where $p = 2N_cN_\alpha + 2N_sN_r - 2\lambda - 2$, and $w = a'a + \mu'C_A'C_A\mu - (X_A'a + C_A'C_A\mu)'(X_A'X_A + C_A'C_A)^{-1}(X_A'a + C_A'C_A\mu) + 2\delta$. Moreover, as discussed in Chapter 1.3, the posterior distribution of the voxel value, β , and the noise variance, σ^2 can be integrated through the MPM technique. Therefore, the marginal posterior distribution of estimate voxel

value β after integration is a student-t distribution $\beta \sim t(\nu^*)$:

$$f(\beta | \cdot) \propto \left\{ 1 + \frac{1}{\nu^*} (\beta - \hat{\beta}_{MPM})' \left[\frac{(X'_A X_A + C'_A C_A)}{\tau^2} \right] (\beta - \hat{\beta}_{MPM}) \right\}^{\frac{\nu^*+1}{2}}, \quad (3.17)$$

with $\nu^* = p - 1$ and $\tau^2 = w/\nu^*$. The marginal posterior mean (MPM) for $\hat{\beta}$ after integration is:

$$E(\beta | \cdot) = \hat{\beta}_{MPM} = (X'_A X_A + C'_A C_A)^{-1} (X'_A a + C'_A C_A \mu). \quad (3.18)$$

In equation 3.18, the matrix $C'_A C_A$ acts as a regularizer for the matrix inverse to improve the condition of the equation. Since the true voxel value from calibration images is close to the true voxel value from acquired aliased images, equation 3.18 leads to $E(\beta | \cdot) = \beta$. The marginal posterior covariance of the voxel value $\hat{\beta}$ is:

$$cov(\beta | \cdot) = \frac{\nu^*}{\nu^* - 2} \tau^2 (X'_A X_A + C'_A C_A)^{-1}, \quad (3.19)$$

the separated voxel values are uncorrelated, meaning that there will not be signal leakage between slices.

Moreover, the marginal posterior distribution of σ^2 after integration is an inverse gamma distribution, $\sigma^2 \sim IG(\gamma, w/2)$:

$$f(\sigma^2 | \cdot) \propto (\sigma^2)^{-\frac{\gamma}{2}-1} \exp[-w/(2\sigma^2)], \quad (3.20)$$

with $\gamma = (p - 1)/2$. The MPM of the noise variance σ^2 is:

$$E(\sigma^2 | \cdot) = \frac{w/2}{\gamma}, \quad (3.21)$$

and the marginal posterior variance of the noise variance is:

$$\text{var}(\sigma^2 | \cdot) = \frac{w/2}{(\gamma - 1)^2(\gamma - 2)}. \quad (3.22)$$

CHAPTER 4: A GRAPPA APPROACH OF MSPECS-IPA-CAIPIVAT

In the previous two chapters, we discussed the mSPECS-CAIPIVAT model in a Bayesian manner, incorporating the TPA acceleration technique and three image shift techniques to reduce the total scan time in Chapter 2. The reconstructed image results from the mSPECS-CAIPIVAT model outperform traditional image reconstruction methods, as will be presented in Chapter 5.2. We also discussed the mSPECS-IPA-CAIPIVAT model in a Bayesian manner, integrating the IPA and TPA combined acceleration technique to further decrease the total image acquisition time in Chapter 3. This model applies image shift techniques corresponding to different shifting directions. However, due to the further reduction in scan time, the dimension of the acquired aliased image decreases, requiring greater consideration of the variety of aliased voxel information. Moreover, as will be discussed in Chapter 5.3, the reconstruction results from the mSPECS-IPA-CAIPIVAT model are sensitive to several factors, including brain image size and the location of the task signal. Therefore, careful experimental design is necessary when applying the mSPECS-IPA-CAIPIVAT model. In this chapter, we present the mSPECS-IPA-CAIPIVAT model in a GRAPPA framework. This approach leverages the advantage of the mSPECS-CAIPIVAT model, which does not require careful experimental design, while also benefiting from the mSPECS-IPA-CAIPIVAT model's reduced image acquisition time.

4.1 The GRAPPA Technique

As we briefly discussed in Chapter 1.1, the Generalized Autocalibrating Partially Parallel Acquisitions (GRAPPA) method has been provided as a powerful technique in the parallel MRI and functional MRI studies and is widely used among different areas (Griswold et al. (2002)). Unlike the SENSitivity Encoding (SENSE) technique mainly focus on the image domain by using the information of the coil sensitivities,

the GRAPPA technique puts more attention to the k -space. Since the in-plane sub-sampling technique is applied, partial lines in the k -space will be skipped and omitted in the k -space to reduce the image scan time. The main purpose of the GRAPPA algorithm is to estimate the missing k -space signals by linearly combining the information from the undersampled k -space signals. The conventional GRAPPA method fills the k -space by a linear combination of the acquired data, and the coefficients for combination are estimated using some auto-calibration signal (ACS) lines usually acquired in the central k -space. A specific size of the kernel will be designed around the target missing data. Based on the local kernels in k -space, the GRAPPA algorithm exploits the learned correlation between multiple channels in neighboring points in k -space. Another GRAPPA technique filling the k -space matrix by combining the spatial frequency information of the calibration reference images with full FOV. In this chapter, the second approach will be the potential technique to estimate the missing points in the k -space.

In order to estimate the coil weighting factors for each point from the calibration images, the first step is to determine the kernel size and chose a neighborhood. Traditionally, the kernel size would be 2×1 , 2×3 , 4×1 , 4×5 , etc.. The size of the kernel will influence the coil weight. After the kernel size is determined, the coil weight matrix can be expressed as:

$$S_{Calib,\delta} = \sum w_{i,j,\delta} S_{i,j,\delta}. \quad (4.1)$$

In equation 4.1, $S_{Calib,\delta}$ is the signal of the k -space of calibration images from δ th coil. It is equal to the summation of the product of the coil weight, $w_{i,j,\delta}$, for the i th row, j th column and δ th coil, and the acquired signal on the same position, $S_{i,j,\delta}$. $S_{Calib,\delta}$ and $S_{i,j,\delta}$ are complex value including the real and the imaginary components, and can be known in the data acquiring process. The wight matrix for each coil, $w_{i,j,\delta}$, is

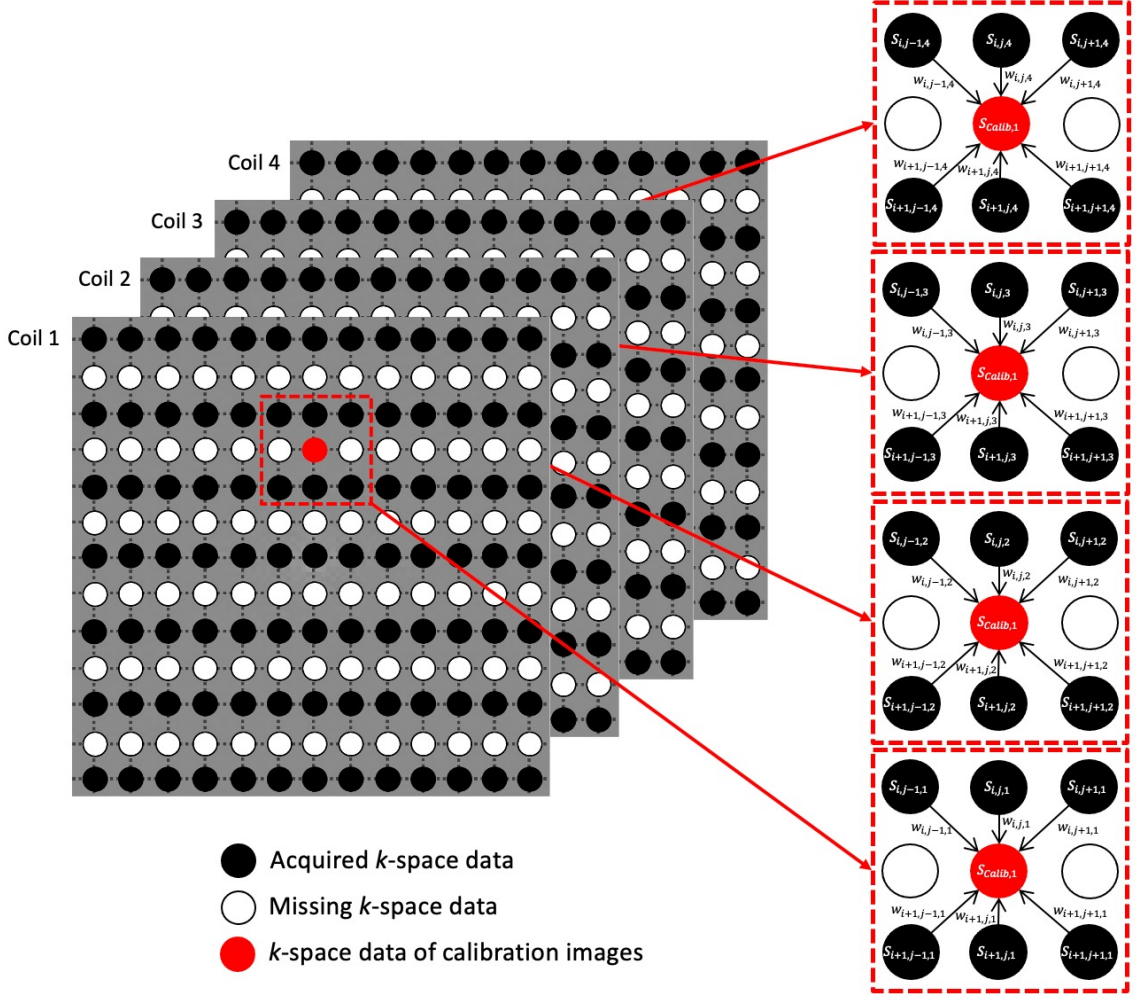


Figure 4.1: The linear combination of the acquired data in the neighborhood of kernel size equal to 2×3 with in-plane acceleration of $IPA = 2$. The black dots are acquired data, white dots are missing data, and the red dot is the known data from the calibration images.

what we want to estimate from the calibration images and can be calculated as:

$$W = S_{Calib} S' (S' S)^{-1}. \quad (4.2)$$

In equation 4.2, vector W contains signal from all coils and matrix S contains frequency information for the surrounding points in the neighborhood. Figure 4.1 is example to show linear combination of the acquired signals in the neighborhood of kernel size equal to 2×3 with the in-plane acceleration of $IPA = 2$. The black points

in Figure 4.1 are acquired data, the white points are missing data, and the red dot is the signal from the calibration images. This process will be repeated for all coils to construct the vector W in equation 4.2. After the coil weighting factors collected from the full FOV calibration reference images, the missing data in the subsampled k -space can be estimated by a linear combination of the neighborhood from all coils. This process can be mathematically expressed as:

$$S_{Target,\delta} = WS. \quad (4.3)$$

In equation 4.3, $S_{Target,\delta}$ is the target missing signal we are trying to estimate, and it equals to the summation of the weight matrix estimated from equation 4.2 times the signal of the acquired data in the kernel. After the missing points are estimated and the k -space was filled, the inverse Fourier transform is applied to acquire the image of full FOV.

4.2 The GRAPPA Approach for mSPECS-IPA-CAIPIVAT

To properly combine the mSPECS-CAIPIVAT and mSPECS-IPA-CAIPIVAT models while incorporating the GRAPPA technique, multiple steps are required. Figure 4.2 presents the flowchart of the mSPECS-IPA-CAIPIVAT model integrated with the GRAPPA approach. The first two steps involve pre-scan calibration image acquisition and hyperparameter assessment. During these steps, neither in-plane nor through-plane acceleration techniques are applied, and image shift techniques are also not incorporated. The reference reconstructed image can be estimated from the calibration images using the SENSE model. Additionally, the coil sensitivity matrix $S_{Calib,\delta}$ in Equation 4.1 is assessed at this stage. Step 3 of the flowchart involves acquiring aliased images based on the mSPECS-IPA-CAIPIVAT model, where the coil sensitivity information of neighboring voxels, $S_{i,j,\delta}$ in Equation 4.1, is determined. In Step 4, the weight matrix, W , is estimated according to Equation 4.2, and the

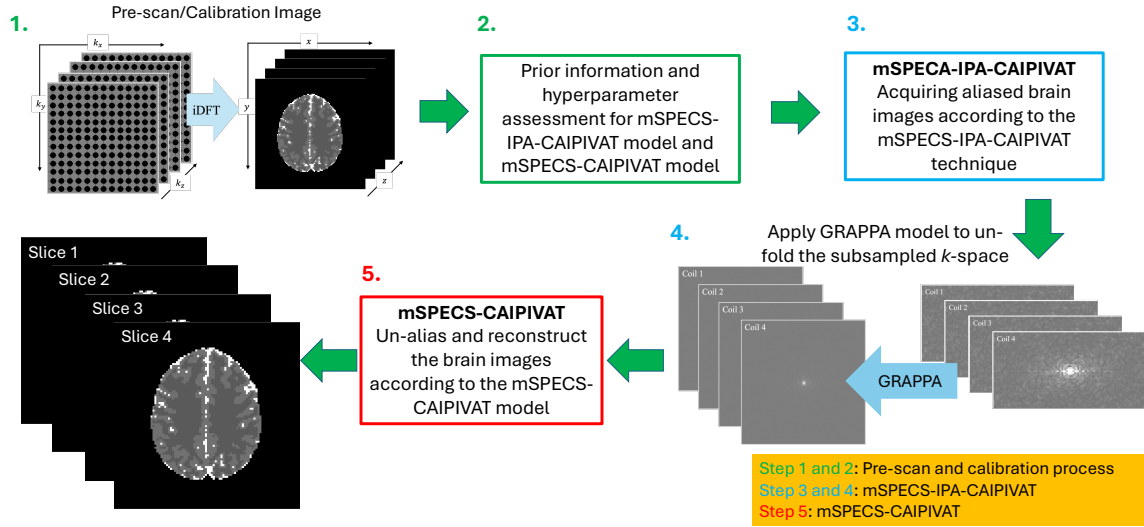


Figure 4.2: The flowchart of the GRAPPA approach of the mSPECS-IPA-CAIPIVAT model.

missing frequency values in k -space are reconstructed following Equation 4.3. During this step, the subsampled k -space is unfolded. The final step in the flowchart applies the mSPECS-CAIPIVAT model to un-alias reconstruct the brain images.

CHAPTER 5: SIMULATED RECONSTRUCTION RESULTS

In order to investigate performance and compare the reconstructed results of the three approaches, we first apply the mSPECS-CAIPIVAT, mSPECS-IPA-CAIPIVAT, and the GRAPPA approach for the mSPECS-IPA-CAIPIVAT model to simulated fMRI data.

5.1 Simulated fMRI Data

The simulated fMRI time series is mimicking the real-world right hand finger tapping experiment with the total time point of the 510 time series. According to the methodology of the image shifted SMS technique, two separate fMRI time series need to be simulated: the acquired fMRI time series and the calibration fMRI time series. The acquired fMRI time series was simulated using the mSPECS-CAIPIVAT, mSPECS-IPA-CAIPIVAT, GRAPPA approach for mSPECS-IPA-CAIPIVAT, as different image shift directions were applied. The calibration fMRI time series, however, was simulated without any image shift technique or acceleration techniques. The calibration images were reconstructed by applying SENSE model. Since the simulated fMRI time series mimics an *in vivo* experiment, the first 20 repetition times are omitted to achieve a steady magnetic field, leaving a total time point of 490 time series. In the simulated fMRI time series, total $N_s = 8$ axial brain images were included in the acquired simulated fMRI time series and the calibration simulated fMRI time series. In the calibration simulated time series, no simulated task block were added to the brain images. On the other hand, the simulated task blocks were added to the left motor cortex of the top 4 brain images. The simulated task blocks were added according to the real-world right hand finger tapping experiment with 15 TRs off and 15 TRs on for 16 epochs, and the first 20 TRs and last 10 TRs off. The contrast-to-noise ratio and the signal-to-noise ratio we choose also mimic the real-world fMRI

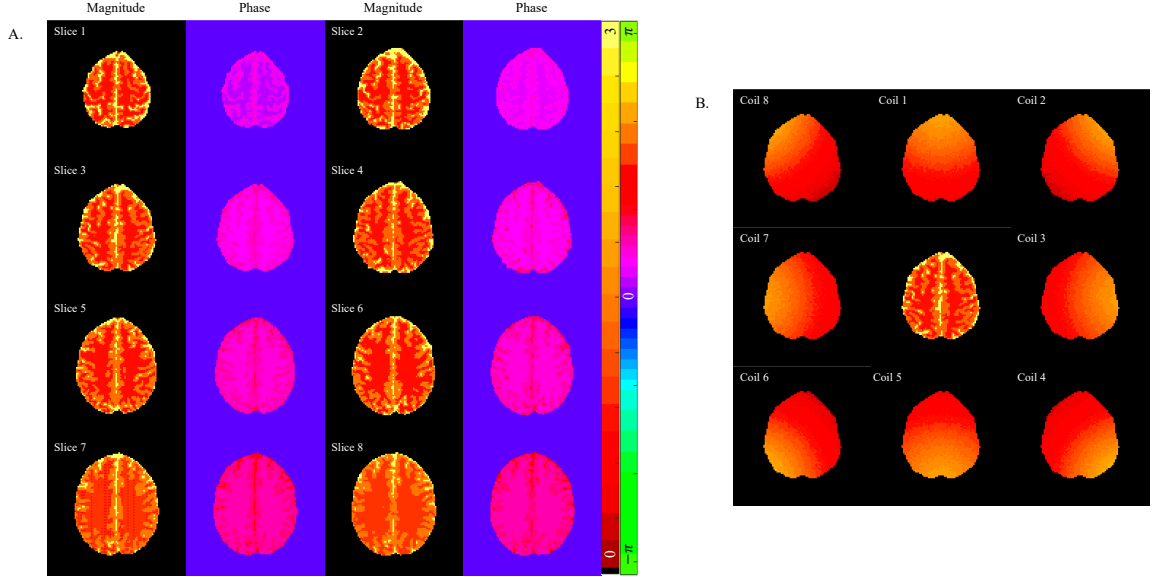


Figure 5.1: A. The magnitude and phase for the true noiseless simulated axial brain images with $N_s = 8$. B. The magnitude of the simulated sensitivity coils for slice 3 with $N_c = 8$.

experiment and $SNR = 50$ and $CNR = 0.5$. Thus, the mean magnitude added to each simulated slice is 4 and the mean magnitude added to the simulated task blocks is 0.04. Moreover, a Gaussian distributed noise $N(0, 0.0064)$ was added to each slice of the simulated acquired fMRI time series and the simulated calibration fMRI time series. In order to increase the difference between each simulated slices, different phase angles from 5° to 40° with 5° intervals were added to each slice. Different phase angles were also added to different brain tissue with 7.5° for white matter (WM), 15° for gray matter (GM), and 22.5° for cerebral spinal fluid (CSF).

In order to investigate the performance of different model with different acceleration factor, the IPA factor we used in the simulated acquired fMRI dataset is $R = 2$, and different TPA factors were incorporated in the experiment with $TPA = 2$, $TPA = 4$, and $TPA = 8$. Thus, the net acceleration factor is the product of the IPA factor and the TPA factor with $NET = 4$, $NET = 8$, and $NET = 16$. For $TPA = 2$ situation, the slices aliasing situation is: packet 1: slice 1 and slice 5, packet 2: slice 2 and slice 6, packet 3: slice 3 and slice 7, packet 4: slice 4 and slice 8. For $TPA = 4$

situation, the slices aliasing situation is: packet 1: even slices, packet 2: odd slices. For $TPA = 8$ situation, all slices are aliased in one packet.

Figure 5.1A shows the true noiseless magnitude and phase for each slice of simulated axial brain images with $N_s = 8$. A total number of $N_c = 8$ channel sensitivity coils were simulated and applied according to the real right hand finger tapping experiment. Figure 5.1B shows the magnitude and position for each coil corresponding to slice 3. The mean magnitude for each simulated coil is 0.95, and to increase the difference between each coil, different phase angles were added to the simulated coils from 0° to 17.5° with 2.5° intervals.

Image Acquisition Time Comparison

To assess the efficiency improvements of the novel approaches, we compared the image acquisition times of mSPECS-CAIPIVAT, mSPECS-IPA-CAIPIVAT, and GRAPPA for mSPECS-IPA-CAIPIVAT approaches. Table 1 presents a comparison of the total scan time across these methods with different acceleration factors. In Table 1, $TPA = 1$ represents the non-accelerated case. For the mSPECS-CAIPIVAT approach, the time repetition for each acceleration factor is the total time repetition divided by the TPA factor. For the mSPECS-IPA-CAIPIVAT and GRAPPA for mSPECS-IPA-CAIPIVAT approaches, the time repetition is calculated by dividing the total time repetition by the NET factor, which is the product of the IPA and TPA factors.

5.2 mSPECS-CAIPIVAT

5.2.1 Non-Task Simulated Reconstruction Results

Following the methodology of the novel slice-wise image shift SMS technique, we conducted the simulated experiment using different through-plane acceleration factors: $TPA=2$, $TPA=4$, and $TPA=8$. We compared the reconstruction results under

Method	Acceleration			
	TPA=1	TPA=2	TPA=4	TPA=8
mSPECS-CAIPIVAT	510	255	127.5	63.75
mSPECS-IPA-CAIPIVAT	510	127.5	63.75	31.875
GRAPPA for mSPECS-IPA-CAIPIVAT	510	127.5	63.75	31.875

Table 1: The comparison of total scan time among the mSPECS-CAIPIVAT, mSPECS-IPA-CAIPIVAT, and GRAPPA for mSPECS-IPA-CAIPIVAT approaches is presented with respect to different acceleration factors. Note that $TPA = 1$ represents the non-accelerated case.

the same acceleration factors from the mSPECS model and the standard SENSE model. Figure 5.2 and Figure 5.3 shows the temporal mean magnitude and phase of the 490 time points reconstructed images from SENSE, mSPECS, mSPECS-VAT, mSPECS-CAIPIRINHA and mSPECS-CAIPIVAT model compared with the true magnitude and the phase of the brain images for odd slices with acceleration factor $TPA=2$. The temporal mean magnitude and phase were estimated according to Equation 2.22. To avoid the error from averaging temporal mean phase at $(\pi, -\pi)$ boundary, the temporal mean is calculated by $\bar{\phi} = \text{angle}(\sum \hat{\beta}_{MPM} / |\hat{\beta}_{MPM}|)$. As shown in Figure 5.2 and Figure 5.3, the mean magnitude and phase of the reconstructed images from the mSPECS, mSPECS-VAT, mSPECS-CAIPIRINHA, and mSPECS-CAIPIVAT models closely match the true values, indicating that these three models produce more accurate reconstructions. In contrast, the SENSE model yields the poorest reconstructions, with noticeable signal leakage from other aliased slices. As the acceleration factor increases to $TPA=4$ and $TPA=8$, the mSPECS, mSPECS-VAT, mSPECS-CAIPIRINHA, and mSPECS-CAIPIVAT models continue to provide reconstructions that closely resemble the true images. However, the reconstruction quality from the SENSE model significantly deteriorates, showing the worst performance.

Figure 5.4 shows the temporal mean of the baseline signal variance of the reconstructed voxel value for slice 3 from SENSE, mSPECS, mSPECS-VAT, mSPECS-

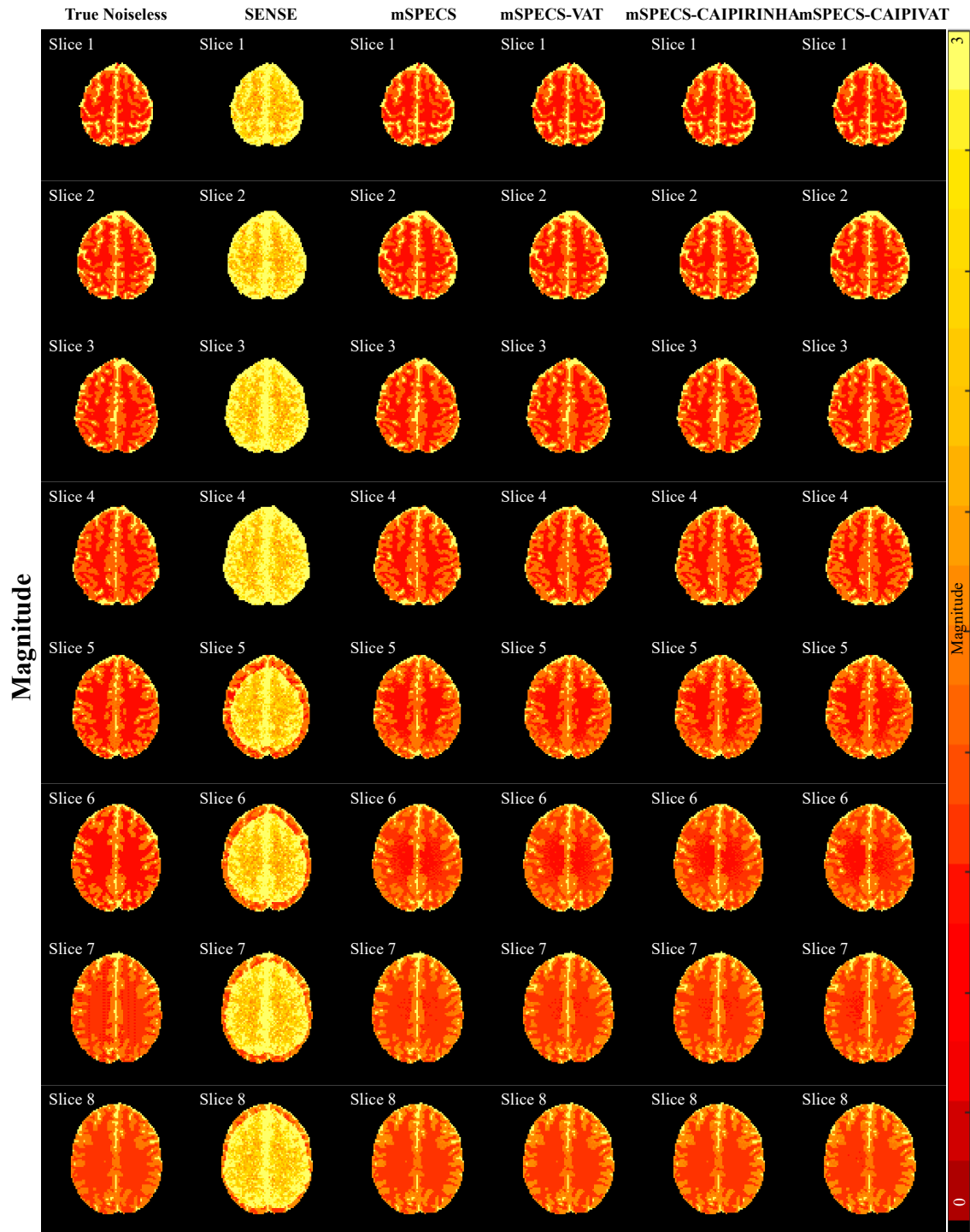


Figure 5.2: The true noiseless simulated magnitude of the axial brain images compared with the temporal mean magnitude and temporal mean phase from SENSE, mSPECS, mSPECS-VAT, mSPECS-CAIPIRINHA and mSPECS-CAIPIVAT model for odd slices with $TPA=2$.

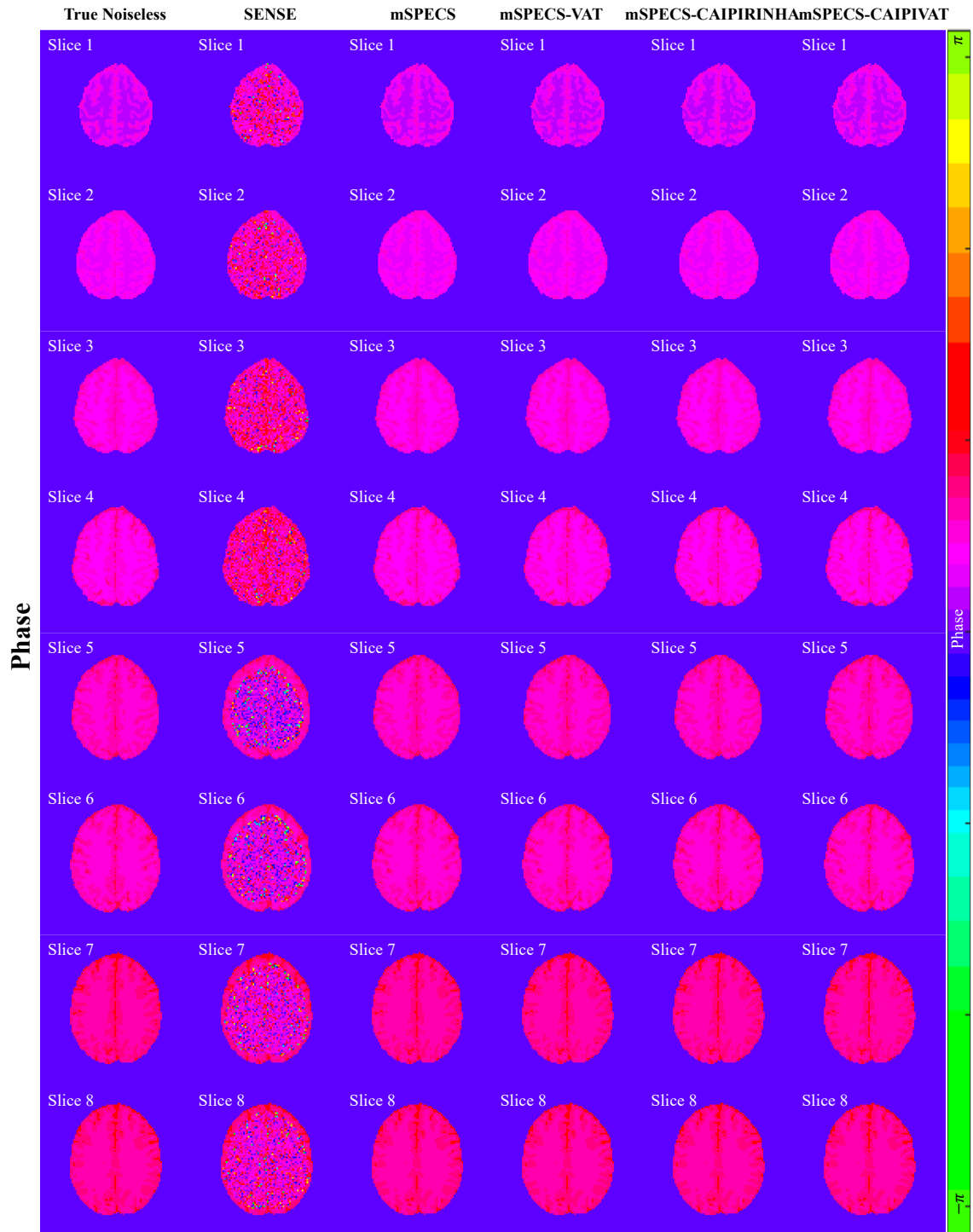


Figure 5.3: The true noiseless simulated phase of the axial brain images compared with the temporal mean magnitude and temporal mean phase from SENSE, mSPECS, mSPECS-VAT, mSPECS-CAIPIRINHA and mSPECS-CAIPIVAT model for odd slices with TPA=2.

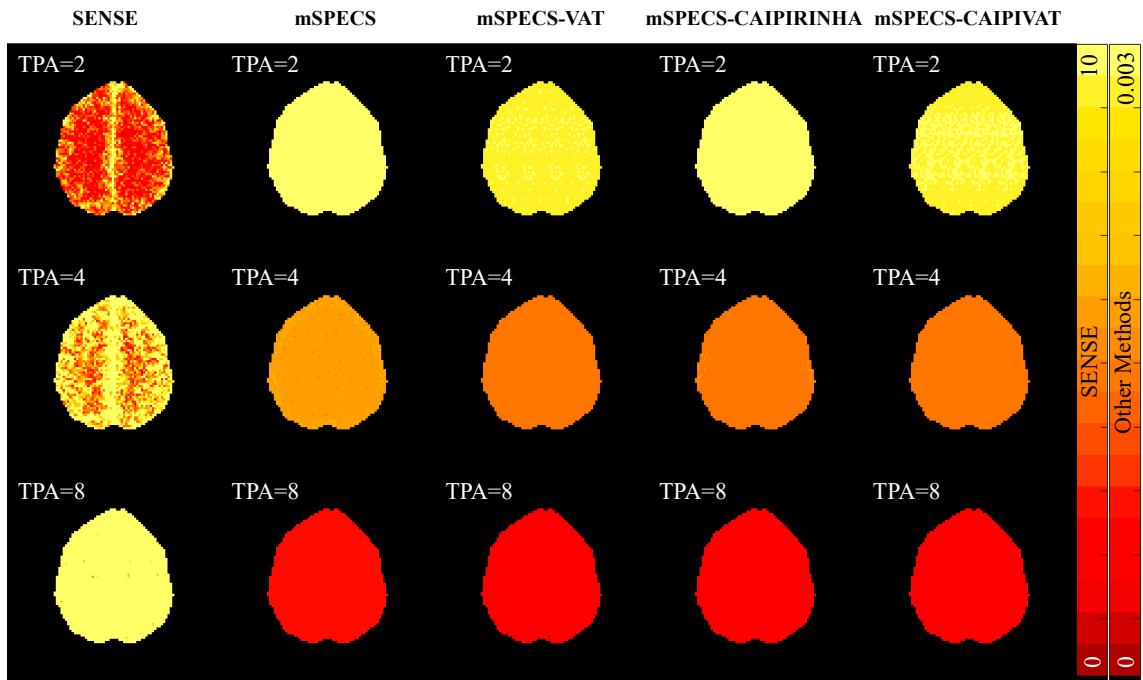


Figure 5.4: The temporal mean of baseline signal variance of the voxel value for slice 3 from SENSE, mSPECS, mSPECS-VAT, mSPECS-CAIPIRINHA, and the mSPECS-CAIPIVAT model with TPA=2, TPA=4, and TPA=8.

CAIPIRINHA, and the mSPECS-CAIPIVAT model with different acceleration factors. The variance of the reconstructed voxel value is calculated according to Equation 2.23. It also can be interpreted as the temporal mean of the variance of the baseline signal. In Figure 5.4, the SENSE model generates a higher temporal variance of the baseline signal compared to mSPECS, mSPECS-VAT, mSPECS-CAIPIRINHA, and the mSPECS-CAIPIVAT model for each acceleration factor. The temporal variance of the reconstructed voxel from the SENSE model increases as the acceleration factor increases, whereas the temporal variance of the reconstructed voxel from the other four models decreases with increasing acceleration factors. Compared to the mSPECS model, the models incorporating image shift techniques generate lower temporal variance, with mSPECS-CAIPIVAT exhibiting the lowest temporal variance of the baseline signal.

To further analyze the performance of each model, Figure 5.5 illustrates the tem-

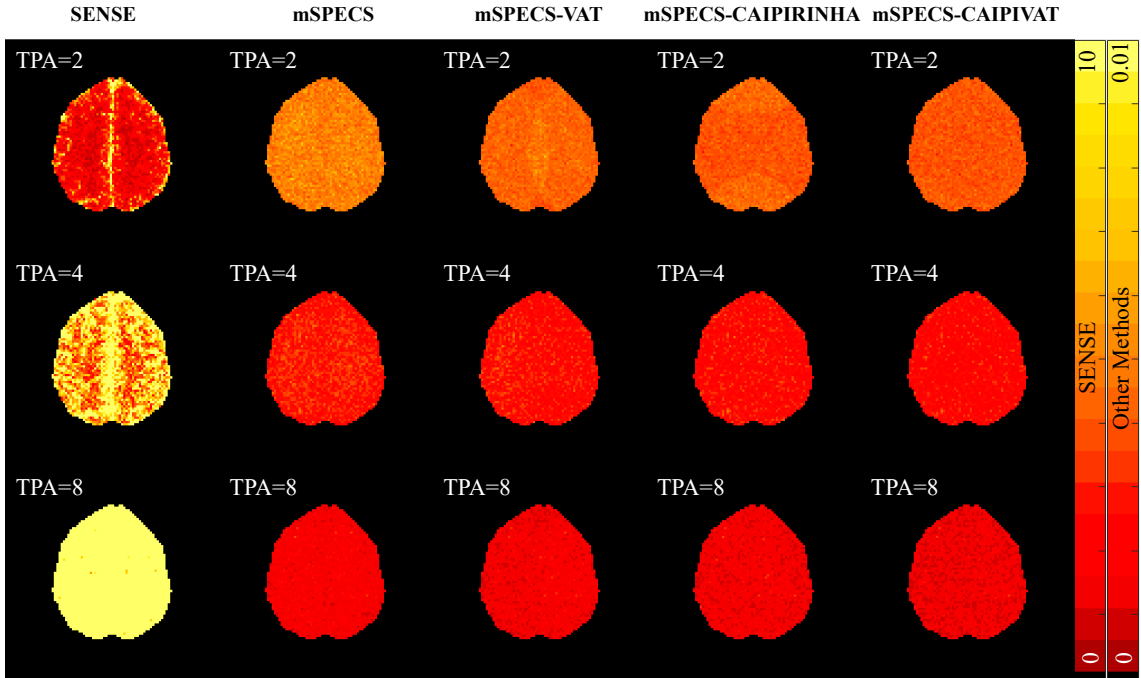


Figure 5.5: The temporal variance of the task signal of SENSE, mSPECS, mSPECS-VAT, mSPECS-CAIPIRINHA, and mSEPCS-CAIPIVAT model with different acceleration factors of slice 3.

poral variance of the task signal of reconstructed images from the SENSE, mSPECS, mSPECS-VAT, mSPECS-CAIPIRINHA, and mSPECS-CAIPIVAT models at different acceleration factors for slice 3. When comparing these four models, we observe a decreasing temporal variance from the SENSE model to the mSPECS-CAIPIVAT model at the same acceleration factor. As the acceleration factor increases, the temporal variance decreases for the mSPECS, mSPECS-VAT, mSPECS-CAIPIRINHA, and mSPECS-CAIPIVAT models, while it increases for the SENSE model. Among the three mSPECS-based models, the mSPECS-CAIPIVAT model achieves the lowest temporal variance.

Figure 5.6 shows the temporal mean of the residual variance from the SENSE, mSPECS, mSPECS-CAIPIRINHA, mSPECS-VAT, and mSPECS-CAIPIVAT model for slice 3 with TPA=2. The temporal mean of the residual variance is calculated according to Equation 2.25. The results show a decreasing trend in the temporal mean

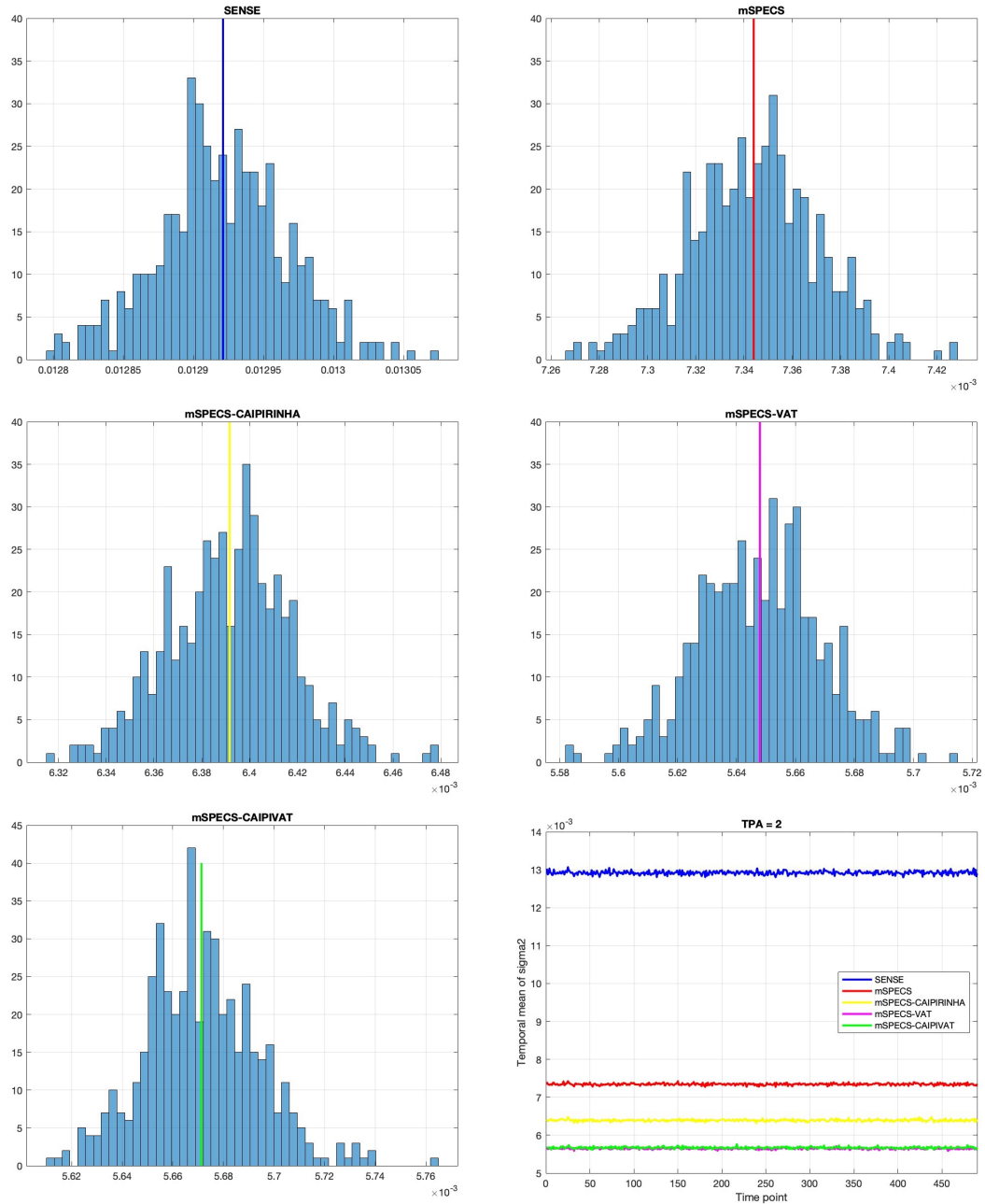


Figure 5.6: The temporal mean of the residual variance for slice 3 from SENSE, mSPECS, mSPECS-CAIPIRINHA, mSPECS-VAT, and mSPECS-CAIPIVAT model with TPA=2.

of the residual variance from SENSE to mSPECS-CAIPIVAT, with the mSPECS-CAIPIVAT model yielding the lowest residual variance. Figure 5.7 shows the temporal mean of the residual variance for slice 3 from SENSE, mSPECS, mSPECS-

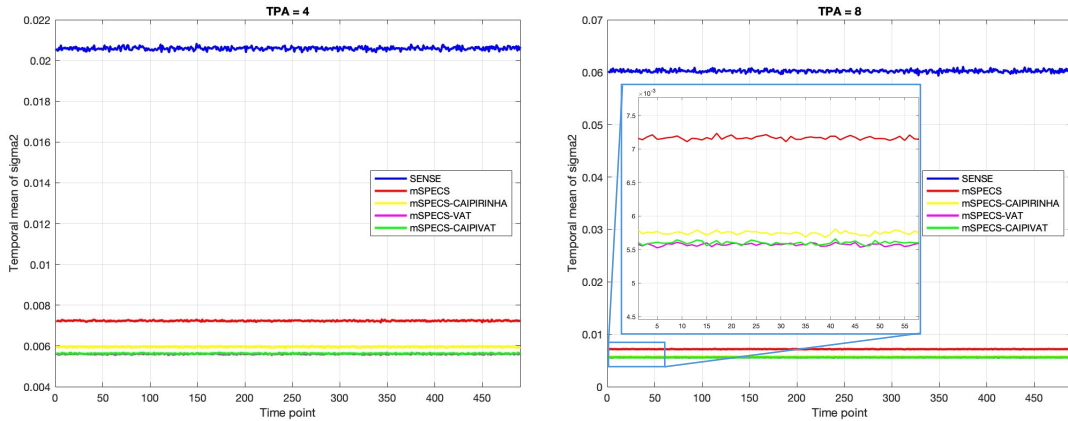


Figure 5.7: The temporal mean of the residual variance for slice 3 from SENSE, mSPECS, mSPECS-CAIPIRINHA, mSPECS-VAT, and mSPECS-CAIPIVAT model with acceleration factor TPA=4 and TPA=8.

CAIPIRINHA, mSPECS-VAT, and mSPECS-CAIPIVAT model with TPA=4 and TPA=8. From Figure 5.6 and Figure 5.7, as the acceleration factor increases, the temporal mean of the residual variance increases for the SENSE model, whereas the other four models maintain a steady residual variance. For each acceleration factor, the mSPECS model exhibits a higher residual variance compared to models incorporating image shift techniques. Among these, the mSPECS-VAT and mSPECS-CAIPIVAT models yield the lowest temporal residual variance. Figure 5.8 shows the temporal variance of the residual variance of slice 3 from SENSE, mSPECS, mSPECS-CAIPIRINHA, mSPECS-VAT, and mSPECS-CAIPIVAT model with TPA=2. The temporal variance of the residual variance is calculated according to Equation 2.26 in the main paper. Figure 5.9 shows the temporal variance of the residual variance of slice 3 from SENSE, mSPECS, mSPECS-CAIPIRINHA, mSPECS-VAT, and mSPECS-CAIPIVAT model with TPA=4 and TPA=8. From Figure 5.8 and Figure 5.9, the temporal variance of the residual variance for all models is close to zero. However, among these five models, the SENSE model produces the highest temporal variance. Compared to the models incorporating image shift techniques, the mSPECS model exhibits a higher temporal variance.

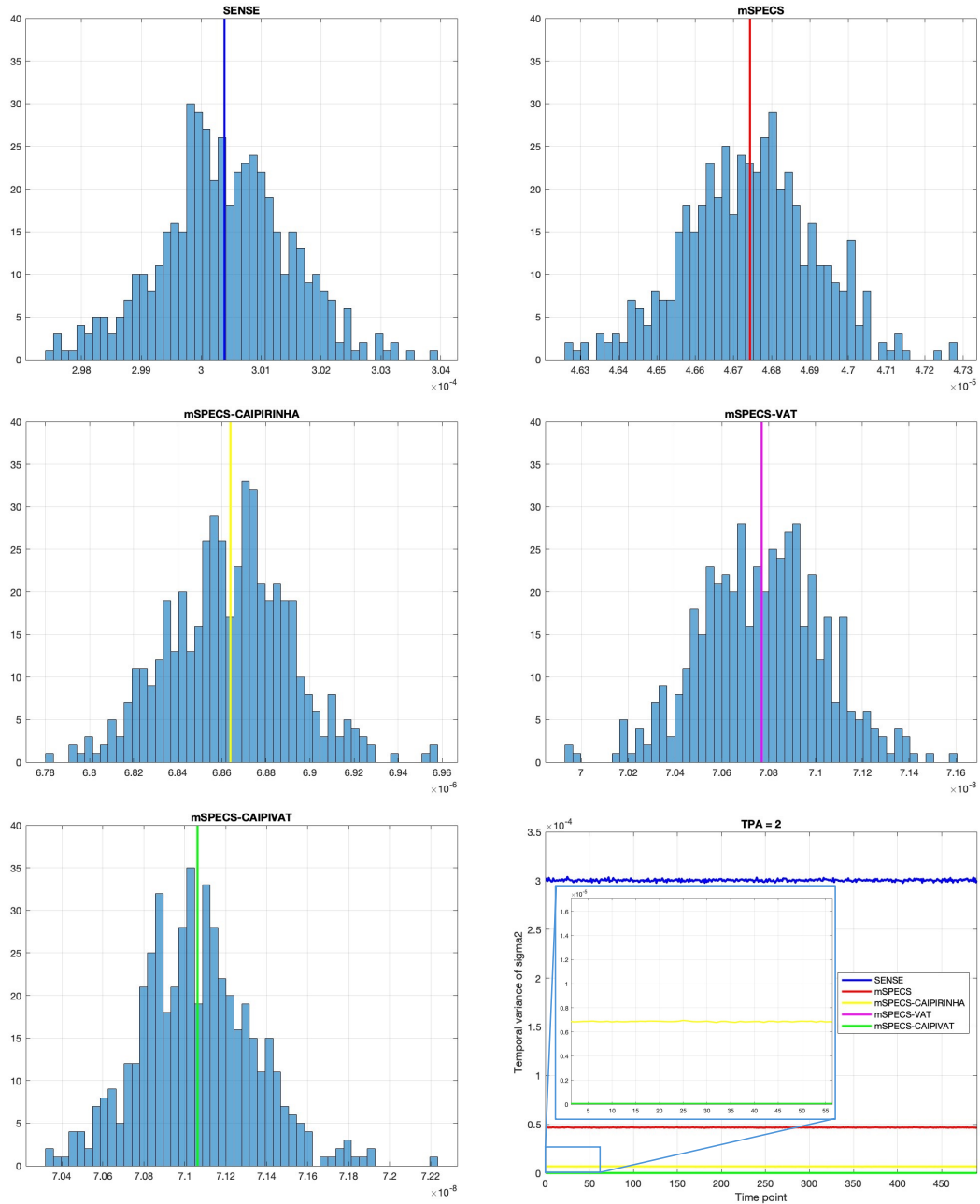


Figure 5.8: The Temporal variance of the residual variance for slice 3 from SENSE, mSPECS, mSPECS-CAIPIRINHA, mSPECS-VAT, and mSPECS-CAIPIVAT model with TPA=2.

To evaluate and compare the changes in SNR and g -factor values for each tissue type across different methods and through-plane acceleration factors, Table 2 presents the average SNR values for cerebral spinal fluid (CSF), gray matter (GM), and white

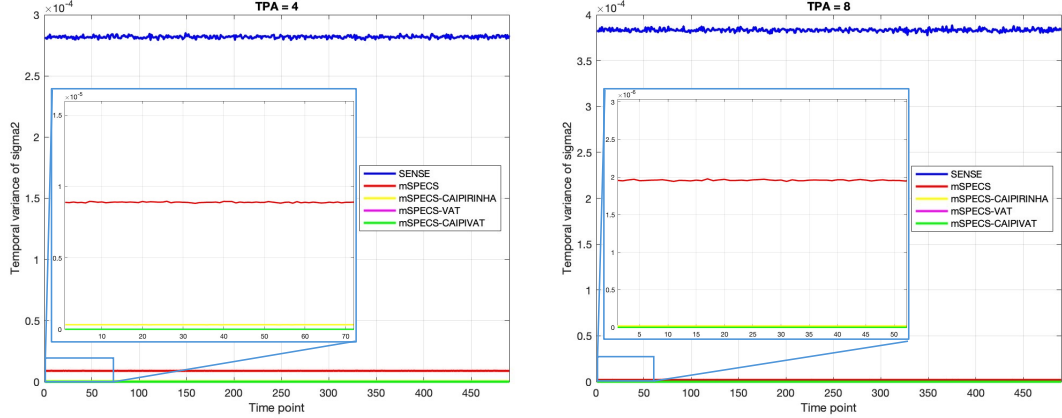


Figure 5.9: The Temporal variance of the residual variance for slice 3 from SENSE, mSPECS, mSPECS-CAIPIRINHA, mSPECS-VAT, and mSPECS-CAIPIVAT model with TPA=4 and TPA=8.

matter (WM), as well as the average g -factor penalty for the whole brain. From Table 2, we observe that the average SNR for CSF and GM in the standard SENSE model decreases slightly as the through-plane acceleration factor increases, while the average SNR for WM remains unchanged. In contrast, the average SNR for all tissue types in the other three models increases significantly with higher acceleration factors. Furthermore, the average g -factor for the SENSE model increases dramatically as the acceleration factor increases, compared to the modest increase in the average g -factor observed in the mSPECS, mSPECS-VAT, mSPECS-CAIPIRINHA, and mSPECS-CAIPIVAT models. Notably, compared to the mSPECS model, the three slice-wise image shift models, mSPECS-VAT, mSPECS-CAIPIRINHA and mSPECS-CAIPIVAT, exhibit lower average g -factor penalties, with the mSPECS-CAIPIVAT model showing the lowest average g -factor.

The SNR value and g -factor value were also compared across four models. The temporal signal-to-noise ratio is defined as $SNR = \bar{S}/\sigma_N$, where \bar{S} is the mean magnitude value in the time series, and σ_N is the standard deviation of the noise. The signal-to-noise ratio also can be expressed as $SNR = \beta_0/\sigma_N$, where β_0 is the baseline signal, and σ_N is the standard deviation of the magnitude of the noise.

SENSE				
Acceleration	CSF- <i>SNR</i>	GM- <i>SNR</i>	WM- <i>SNR</i>	<i>g</i> -factor
TPA=2	2.25	1.95	1.92	14.21
TPA=4	1.96	1.92	1.91	21.28
TPA=8	1.91	1.91	1.91	30.13
mSPECS				
Acceleration	CSF- <i>SNR</i>	GM- <i>SNR</i>	WM- <i>SNR</i>	<i>g</i> -factor
TPA=2	55.00	19.06	12.11	1.30
TPA=4	73.49	25.29	16.11	1.39
TPA=8	101.14	34.92	22.20	1.44
mSPECS-VAT				
Acceleration	CSF- <i>SNR</i>	GM- <i>SNR</i>	WM- <i>SNR</i>	<i>g</i> -factor
TPA=2	58.81	20.46	13.13	1.22
TPA=4	74.75	26.32	16.91	1.36
TPA=8	104.44	36.27	23.36	1.38
mSPECS-CAIPIRINHA				
Acceleration	CSF- <i>SNR</i>	GM- <i>SNR</i>	WM- <i>SNR</i>	<i>g</i> -factor
TPA=2	59.85	21.13	13.54	1.16
TPA=4	76.25	26.87	17.38	1.27
TPA=8	104.98	36.82	23.69	1.34
mSPECS-CAIPIVAT				
Acceleration	CSF- <i>SNR</i>	GM- <i>SNR</i>	WM- <i>SNR</i>	<i>g</i> -factor
TPA=2	61.11	21.41	13.73	1.15
TPA=4	78.19	27.56	17.89	1.27
TPA=8	107.72	37.97	24.50	1.29

Table 2: The average *SNR* value for cerebrospinal fluid (CSF), gray matter (GM), and white matter (WM) with the average *g*-factor value of the whole brain with respect to SENSE, mSPECS, mSPECS-VAT, mSPECS-CAIPIRINHA, and mSPECS-CAIPIVAT methods with through-plane acceleration factors TPA=2, TPA=4, and TPA=8 for slice 3.

Based on the definition of *SNR* in Chapter 2.1.1, the *g*-factor can be calculated as $g_{accelerate} = \sqrt{N_s} SNR_{full} / SNR_{accelerate} \sqrt{R}$, where SNR_{full} is the *SNR* map from model without acceleration technique, and R indicates the in-plane acceleration factor, which in this case $R = 1$. The *g*-factor also indicates the noise amplification level of the model. Figure 5.10 shows the temporal *SNR* map and *g*-factor map for the standard SENSE, mSPECS, mSPECS-VAT, mSPECS-CAIPIRINHA and mSPECS-CAIPIVAT models with through-plane acceleration factors TPA=2, TPA=4, and

TPA=8 for slice 3. From Figure 5.10, we observe that the standard SENSE model produces a low *SNR* map and a high *g*-factor penalty for all acceleration factors compared to the other four models. Increasing the through-plane acceleration factors reduces the *SNR* value and significantly increases the *g*-factor penalty. Although the mSPECS model offers a relatively good *SNR* map, the *g*-factor penalty increases as the through-plane acceleration factors rise. The mSPECS-VAT, mSPECS-CAIPIRINHA and mSPECS-CAIPIVAT models, however, provide better *SNR* and *g*-factor maps, with higher *SNR* values and lower *g*-factor penalties. As the through-plane acceleration factor increases, the *SNR* maps become brighter, indicating an increase in *SNR*, while the *g*-factor penalties remain relatively steady, as shown in Figure 5.10.

5.2.2 Task Simulated Reconstruction Results

We also applied the novel slice-wise image shift SMS models to the simulated right-handed finger-tapping fMRI data with different through-plane acceleration factors TPA=2, TPA=4, and TPA=8, and compared the task activation results between each method. In the interest of further exploring the task detection ability for each model, two important criteria, the contrast-to-noise (*CNR*) value and the activation detection maps were also investigated. The *CNR* ratio is calculated as $CNR = \beta_1/\sigma_N$, where β_1 represents the task activation signal contrast. Activation detection was performed using a complex-valued model to compute fMRI activation (Rowe and Logan (2004)). Figure 5.11 shows the *CNR* map for SENSE, mSPECS, mSPECS-VAT, mSPECS-CAIPIRINHA and mSPECS-CAIPIVAT model for at TPA=2, and the average *CNR* value and standard deviation of *CNR* value for region-of-interest (ROI). Since no simulated activation blocks were added to the last four slices, *CNR* values were not captured from those regions. In Figure 5.11, the SENSE model fails to capture any activation signal within the brain, while the

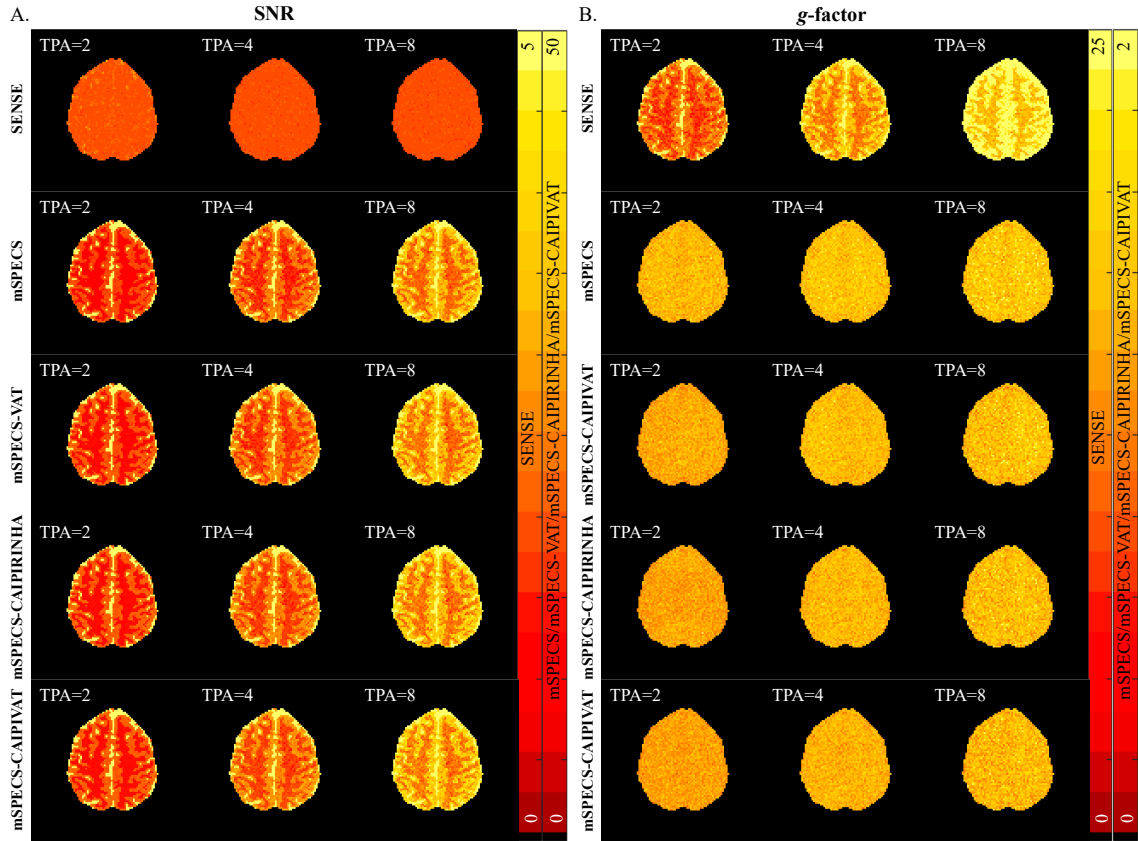


Figure 5.10: A. The SNR maps for SENSE, mSPECS, mSPECS-VAT, mSPECS-CAIPIRINHA and mSPECS-CAIPIVAT model with TPA=2, TPA=4, and TPA=8. The higher SNR , the better model performs. B. The g -factor maps for SENSE, mSPECS, mSPECS-VAT, mSPECS-CAIPIRINHA and mSPECS-CAIPIVAT model with TPA=2, TPA=4, and TPA=8. The closer g -factor is to 1, the better model performs.

mSPECS, mSPECS-VAT, mSPECS-CAIPIRINHA, and mSPECS-CAIPIVAT models successfully capture the simulated activation blocks with clear shapes and anatomical details. When comparing the average CNR value of the ROI, the mSPECS-VAT, mSPECS-CAIPIRINHA and mSPECS-CAIPIVAT models demonstrate slightly higher values than the mSPECS model with TPA=2. To further examine the influence of the acceleration factor on activation detection, we compared the CNR maps of the four models at different acceleration factors. Figure 5.12A displays the CNR maps from the SENSE, mSPECS, mSPECS-VAT, mSPECS-CAIPIRINHA, and mSPECS-CAIPIVAT models for TPA=2, TPA=4, and TPA=8 in slice 3. As the accelera-

tion factor increases, the average *CNR* value of the ROI decreases for the mSPECS, mSPECS-VAT, mSPECS-CAIPIRINHA, and mSPECS-CAIPIVAT models. However, the average *CNR* value in the three slice-wise image-shifting models remains slightly higher than in the mSPECS model. In contrast, the SENSE model fails to capture any simulated activation blocks at any acceleration factor. The mSPECS-CAIPIVAT provides the highest average *CNR* of the ROI among the three slice-wise image-shifting models with higher acceleration factors.

Concerning the main goal of this study is to improve the task activation detection rate, we also examined the activation detection map across four models. Figure 5.13 shows the activation detection maps for odd slices from SENSE, mSPECS, mSPECS-VAT, mSPECS-CAIPIRINHA and mSPECS-CAIPIVAT model for odd slices at acceleration factor TPA=2. Similar to the results observed in the *CNR* map, it is difficult to capture the simulated task activation blocks by applying the SENSE model. Additionally, the average z-score of the ROI from the SENSE model is the lowest among five models. In contrast, the mSPECS, mSPECS-VAT, mSPECS-CAIPIRINHA, and mSPECS-CAIPIVAT models can capture the simulated task activation blocks with complete shapes and anatomical structures. Comparing the average z-scores of the ROI from these three models, the three slice-wise image-shifting models, mSPECS-VAT, mSPECS-CAIPIRINHA and mSPECS-CAIPIVAT, exhibit higher significance levels than the mSPECS model. The mSPECS-CAIPIVAT model provides the highest average z-score of the ROI, indicating that it is more powerful in detecting activation signals than the other models. Similarly, we applied the four models with different acceleration factors to further investigate the activation detection process. Fig. 5.12B shows the task activation detection maps from the SENSE, mSPECS, mSPECS-VAT, mSPECS-CAIPIRINHA, and mSPECS-CAIPIVAT models at acceleration factors of TPA=2, TPA=4, and TPA=8 for slice 3. As the acceleration factor increases, the SENSE model fails to capture any task activation signals, and the

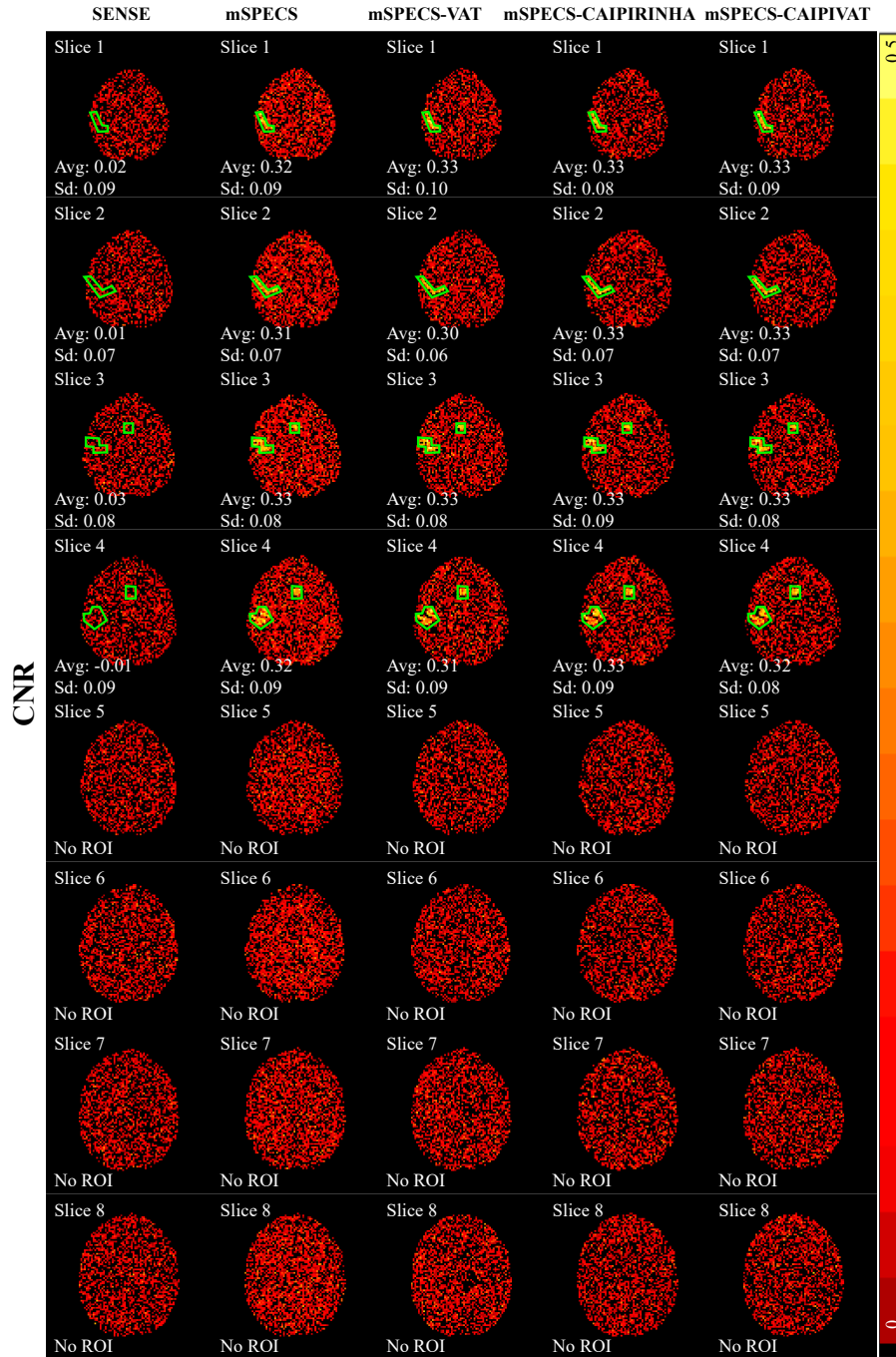


Figure 5.11: The *CNR* map and the average *CNR* value and standard deviation of *CNR* of ROI for SENSE, mSPECS, mSPECS-VAT, mSPECS-CAIPIRINHA and mSPECS-CAIPIVAT model for odd slices with TPA=2.

average z-score of the ROI remains the lowest among the four models. The average z-score of the ROI from the mSPECS, mSPECS-VAT, mSPECS-CAIPIRINHA,

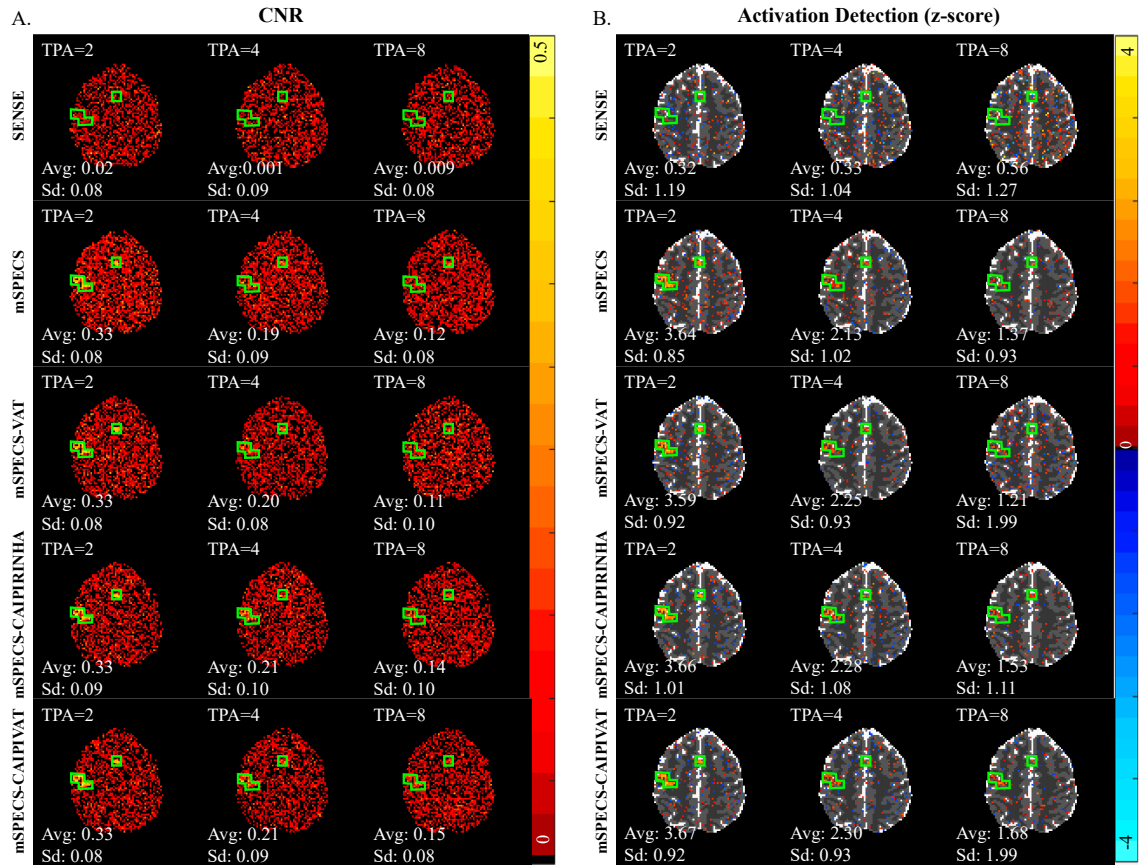


Figure 5.12: A. The *CNR* maps and average ROI *CNR* value from SENSE, mSPECS, mSPECS-VAT, mSPECS-CAIPIRINHA and mSPECS-CAIPIVAT model with respect to different acceleration factors TPA=2, TPA=4, and TPA=8 for slice 3. B. The task activation detection maps and average ROI z-score from SENSE, mSPECS, mSPECS-CAIPIRINHA and mSPECS-CAIPIVAT model with respect to acceleration factor TPA=2, TPA=4 and TPA=8 for slice 3. The higher *CNR* and z-score, the better model performs.

and mSPECS-CAIPIVAT models decreases with increasing acceleration factor, and it becomes more challenging to capture the full shape of the task activation blocks. However, consistent with the *CNR* map results, the three slice-wise image-shifting models provide higher average z-scores of the ROI compared to the mSPECS model. The mSPECS-CAIPIVAT model offers the highest average z-score, confirming that it is more effective in detecting activation signals than the other models.

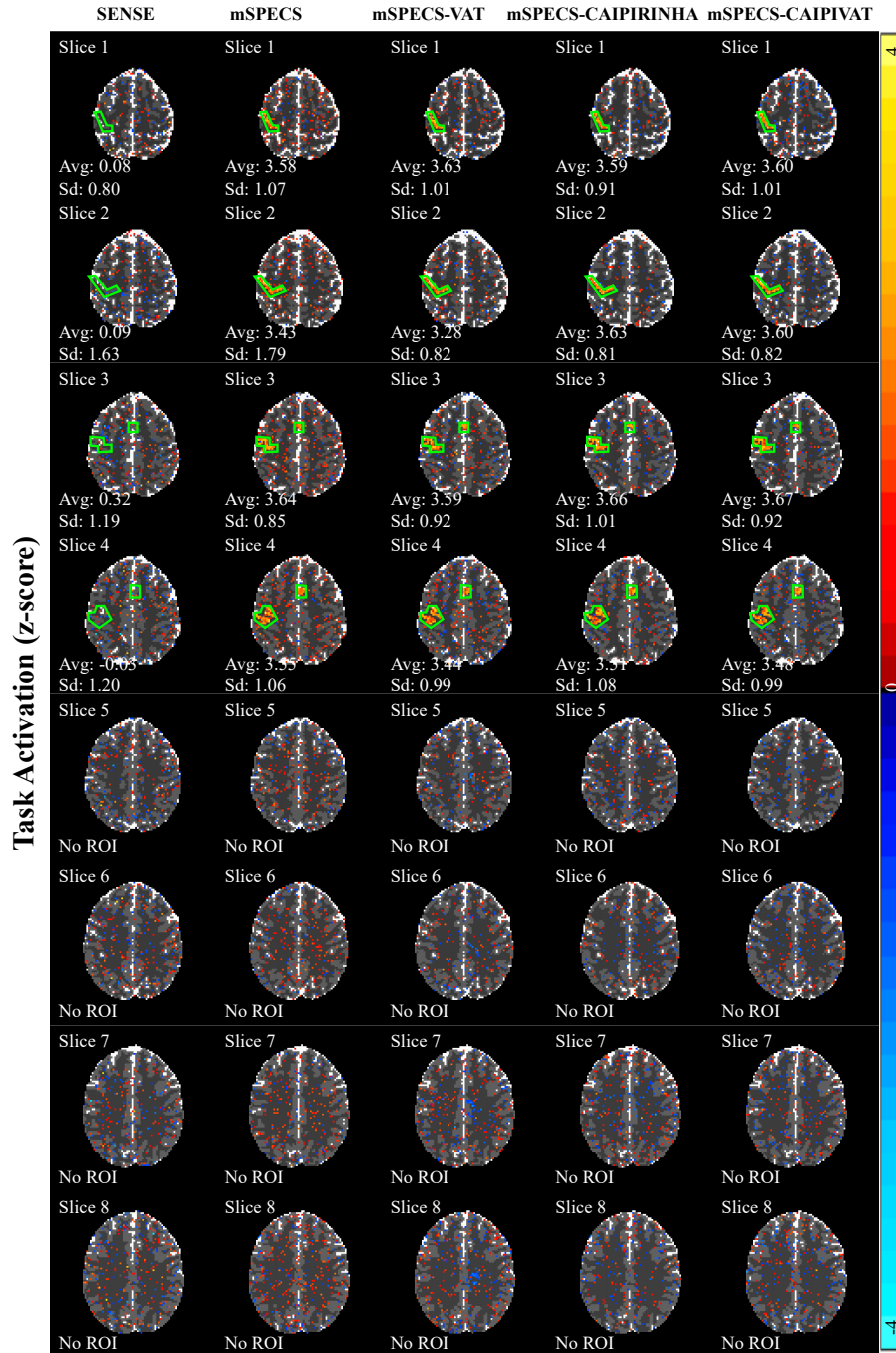


Figure 5.13: The activation detection map and the average and standard deviation of z-score of ROI for SENSE, mSPECS, mSPECS-VAT, mSPECS-CAIPIRINHA and mSPECS-CAIPIVAT model for odd slices with TPA=2 situation.

5.3 mSPECS-IPA-CAIPIVAT

5.3.1 Non-Task Simulated Reconstruction Results

Based on the methodology of the novel proposed image shift SMS techniques, we conducted the simulated experiment with the same in-plane acceleration factor, $IPA = 2$, and different through-plane acceleration factors with $TPA = 2$, $TPA = 4$, and $TPA = 8$. The reconstructed results were compared between mSPECS-IPA model (without image shift technique), mSPECS-IPA-CAIPIRINHA model (image shift along vertical direction), mSPECS-IPA-VAT model (image shift along horizontal direction), and mSPECS-IPA-CAIPIVAT (image shift along vertical and horizontal direction). The reconstructed results were also compared with the true noiseless simulated images. Figure 5.14 and Figure 5.15 show the mean magnitude and mean phase from odd slices of the reconstructed images from mSPECS-IPA, mSPECS-IPA-CAIPIRINHA, mSPECS-IPA-VAT, and mSPECS-IPA-CAIPIVAT, compared with the magnitude and phase from true noiseless simulated images, and the through-plane acceleration factor is 2. Figure 5.14 and Figure 5.15 are generated based on Equation 3.18. Compared to the true magnitude, the mean magnitude from these four models is closely aligned with the true value. No inter-slice signal leakage or artifact distortions appear in the mean magnitude images. The mean phase of the reconstructed images from these four models is also consistent with the phase value of the true noiseless simulated image inside the brain. However, residuals are present outside the brain in the mSPECS-IPA, mSPECS-IPA-CAIPIRINHA, mSPECS-IPA-VAT, and mSPECS-IPA-CAIPIVAT models due to differences in the image shift techniques and slice overlapping conditions in each model.

Figure 5.16 was generated according to Equation 3.19. The top-right corner displays the overlapping indicator for each novel SMS image reconstruction model, incorporating different TPA factors. It represents the slice overlapping and voxel

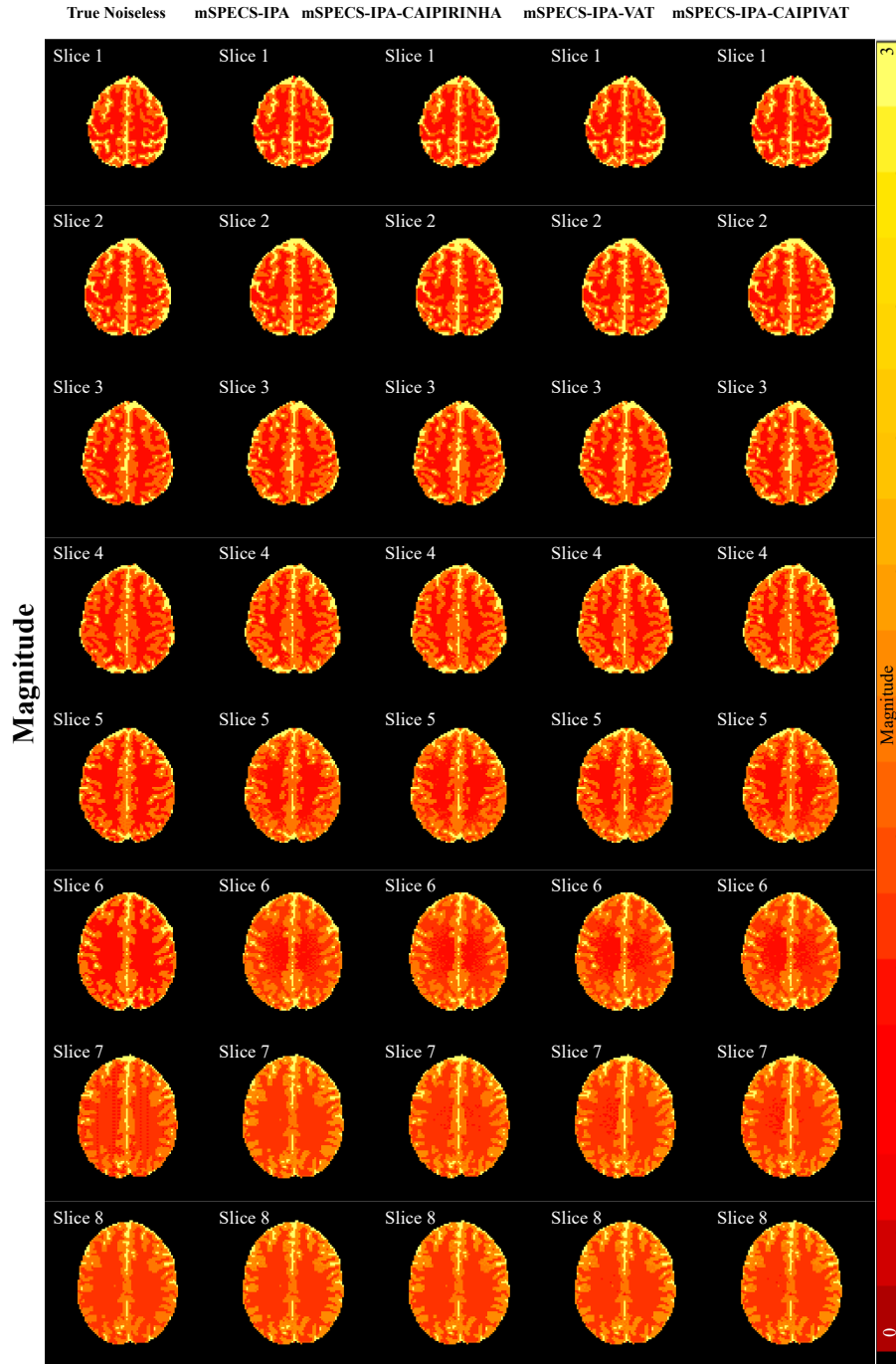


Figure 5.14: The magnitude of the reconstructed images from mSPECS-IPA, mSPECS-IPA-CAIPIRINHA, mSPECS-IPA-VAT, and mSPECS-IPA-CAIPIVAT, compared with the magnitude and phase from true noiseless simulated images with TPA=2.

aliasing situation for each approach and acceleration factor. When the acceleration factor is low, IPA = 2 and TPA = 2, all four models have a low variance at the center

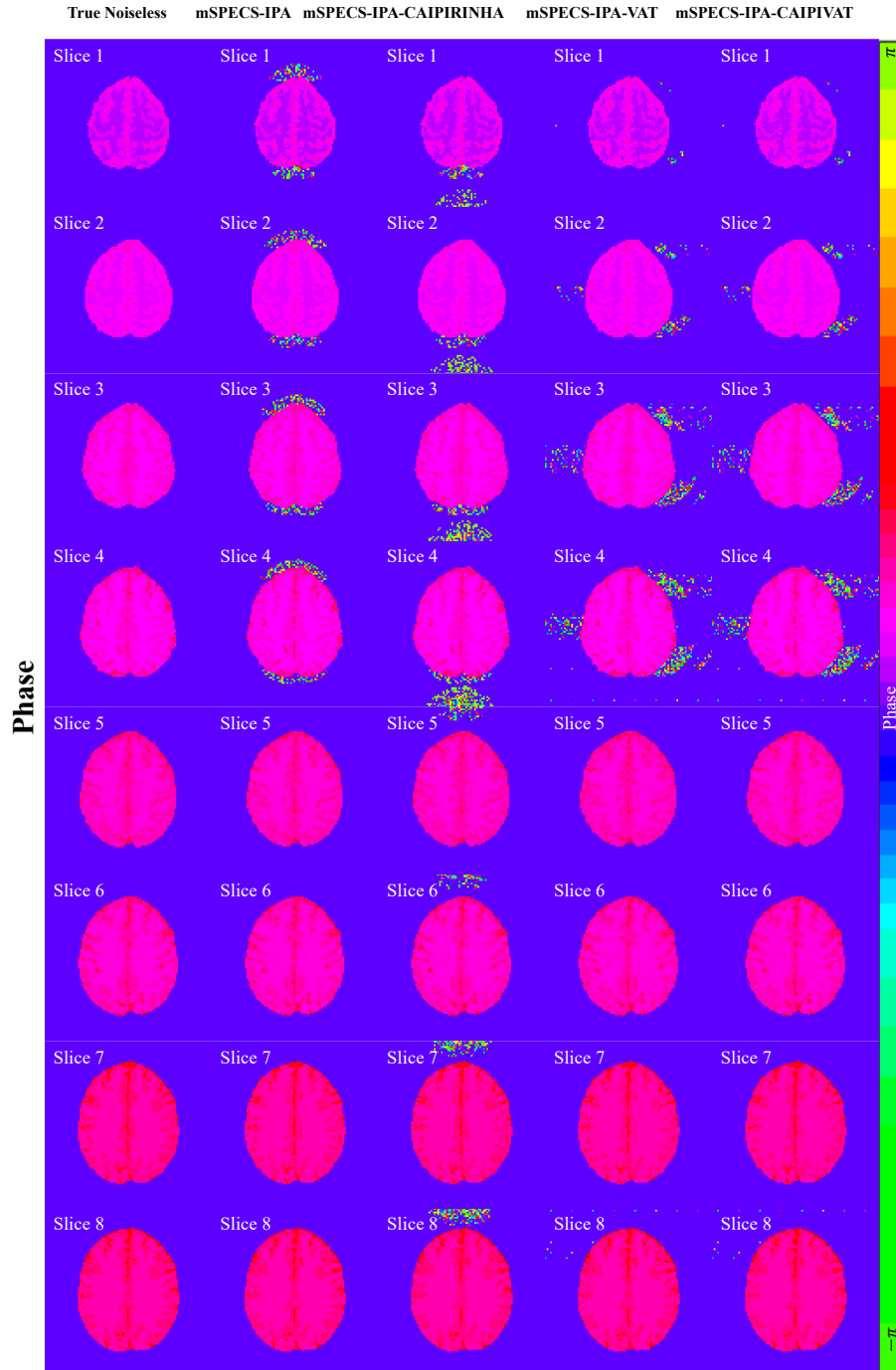


Figure 5.15: The phase of the reconstructed images from mSPECS-IPA, mSPECS-IPA-CAIPIRINHA, mSPECS-IPA-VAT, and mSPECS-IPA-CAIPIVAT, compared with the magnitude and phase from true noiseless simulated images odd slices with TPA=2.

of the brain image. However, due to a high overlapping indicator value at the anterior and posterior regions, high variance is detected at these region. As the acceleration

Variance of Baseline Signal

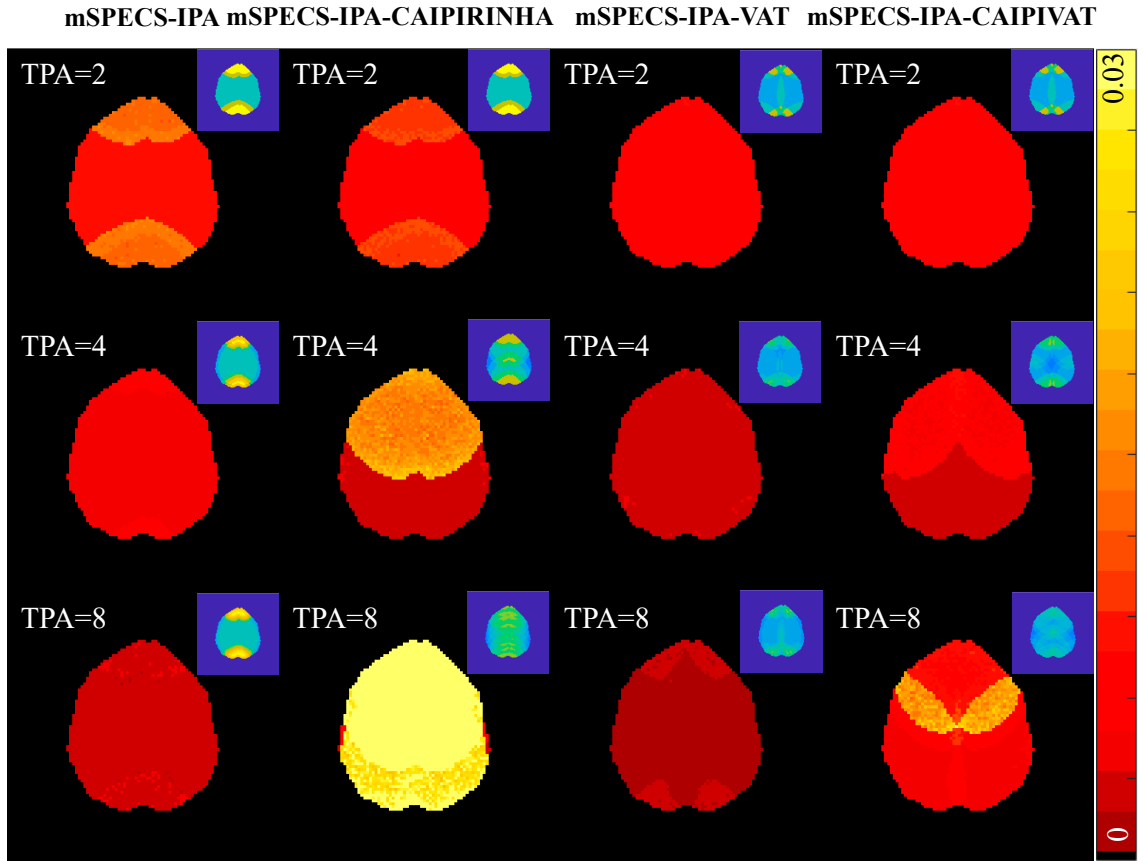


Figure 5.16: The variance of the baseline regression coefficient of slice 3 from reconstructed images from mSPECS-IPA, mSPECS-IPA-CAIPIRINHA, mSPECS-IPA-VAT, and mSPECS-IPA-CAIPIVAT model with different through-plane acceleration factors. The top right corner is the slices aliasing situation for slice 3 with different acceleration factors.

factor increases, models that do not incorporating with vertical image shift technique, mSPECS-IPA and mSPECS-IPA-VAT model, show a decrease in task regression coefficient variance. On the other hand, models that incorporate with the vertical image shift technique, mSPECS-IPA-CAIPIRINHA and mSPECS-IPA-CAIPIVAT model, exhibit an increase in task regression coefficient variance in the anterior region of the brain image. Among these four models, the mSPECS-IPA-CAIPIRINHA has the highest task regression coefficient variance when IPA = 2 and TPA = 8. Figure 5.17 shows the temporal variance of task coefficient of slice 3 from the reconstructed

Variance of Task Signal

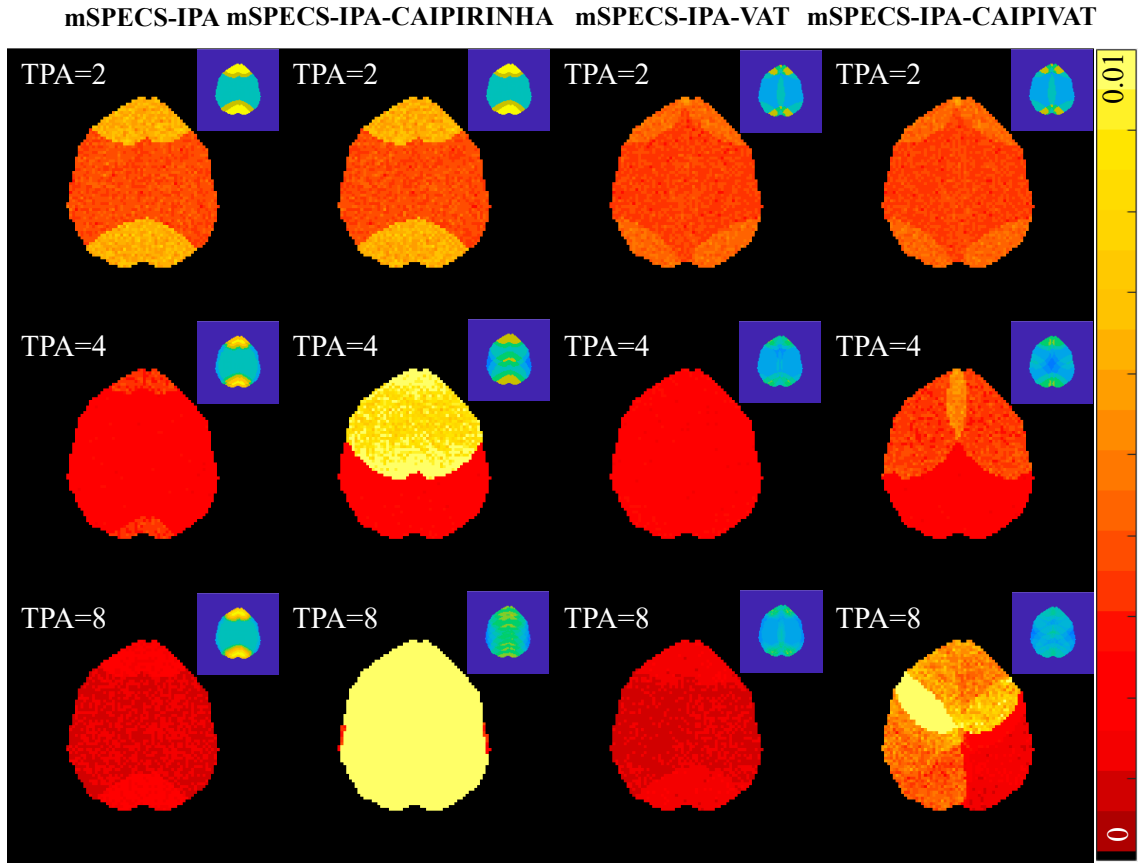


Figure 5.17: The task regression coefficient variance of slices 3 from reconstructed images from mSPECS-IPA, mSPECS-IPA-CAIPIRINHA, mSPECS-IPA-VAT, and mSPECS-IPA-CAIPIVAT model with different through-plane acceleration factors. The top right corner is the slices aliasing situation for slice 3 with different acceleration factors.

images corresponding to the mSPECS-IPA, mSPECS-IPA-CAIPIRINHA, mSPECS-IPA-VAT, and mSPECS-IPA-CAIPIVAT with different through-plane acceleration factors. The top right corner is the slice overlapping situation corresponding to the average of first N_α time point for each model, indicating the voxel aliasing complexity for each method. For $TPA = 2$ and $IPA = 2$, the voxel aliasing and slice overlapping conditions are identical for the mSPECS-IPA and mSPECS-IPA-CAIPIRINHA models, as well as for the mSPECS-IPA-VAT and mSPECS-IPA-CAIPIVAT models. Consequently, the temporal variance of the reconstructed images from mSPECS-

structed from mSPECS-IPA, mSPECS-IPA-CAIPIRINHA, mSPECS-IPA-VAT and mSPECS-IPA-CAIPIVAT model with $IPA = 2$ and $TPA = 2$. Figure 5.19 shows temporal mean of residual variance for brain images reconstructed from same models but with acceleration factors $IPA = 2$ and $TPA = 4$ and 8 . Figure 5.18 and Figure 5.19 are generated based on equation 3.21. For each acceleration factor, among the four models, mSPECS-IPA has the highest temporal mean of residual variance, whereas the models incorporating the horizontal image shift technique, mSPECS-IPA-VAT and mSPECS-IPA-CAIPIVAT, exhibit the lowest temporal mean of residual variance. As the acceleration factor increases, the temporal mean of residual variance slightly decreases across all four models. Figure 5.20 and Figure 5.21. Figure 5.20 shows the temporal variance of the residual variance for brain images reconstructed from four SMS models: mSPECS-IPA, mSPECS-IPA-CAIPIRINHA, mSPECS-IPA-VAT and mSPECS-IPA-CAIPIVAT model with $IPA = 2$ and $TPA = 2$. Figure 5.21 shows the temporal variance of the residual variance for brain images reconstructed from the same model but with acceleration factor $IPA = 2$ and $TPA = 4$ and 8 . Figure 5.20 and Figure 5.21 are generated from equation 3.22. For each acceleration factor, the mSPECS-IPA model has the highest temporal variance of residual variance, while

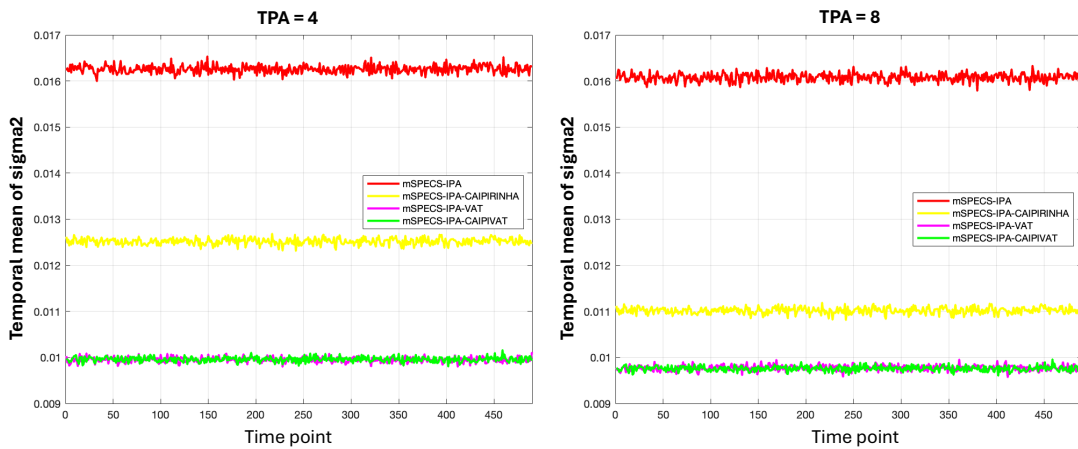


Figure 5.19: The temporal mean of residual variance of brain images reconstructed from mSPECS-IPA, mSPECS-IPA-CAIPIRINHA, mSPECS-IPA-VAT and mSPECS-IPA-CAIPIVAT model with $IPA = 2$ and $TPA = 4$ and 8 .

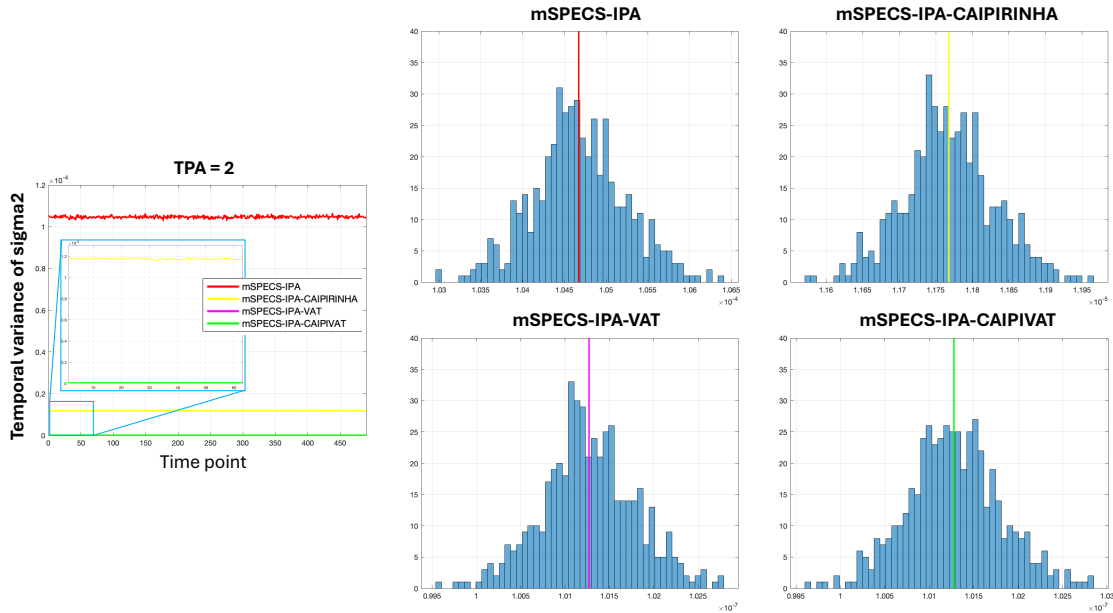


Figure 5.20: The variance of the baseline regression coefficient of slice 3 from reconstructed images from mSPECS-IPA, mSPECS-IPA-CAIPIRINHA, mSPECS-IPA-VAT, and mSPECS-IPA-CAIPIVAT model with different through-plane acceleration factors.

the mSPECS-IPA-VAT and mSPECS-IPA-CAIPIVAT models have the lowest, with values approaching zero. Moreover, as the acceleration factor increases, the temporal variance of residual variance decreases for all four models.

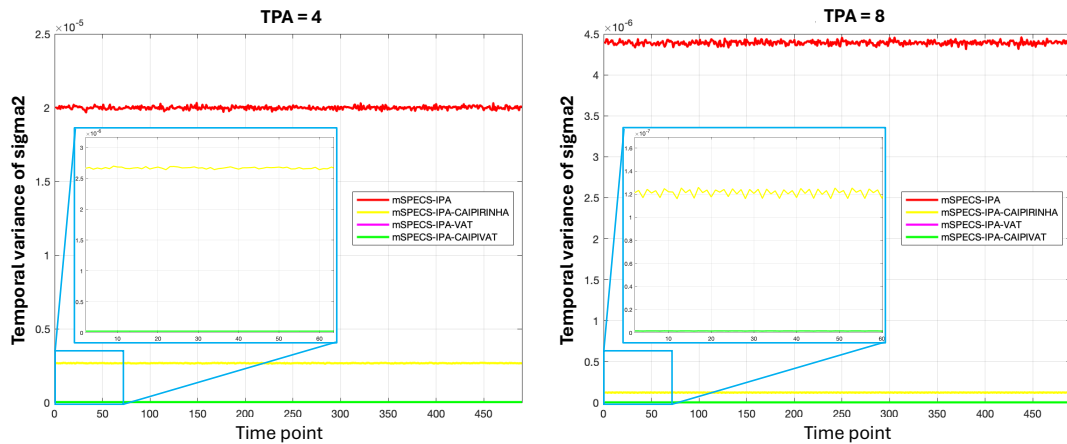


Figure 5.21: The variance of the baseline regression coefficient of slice 3 from reconstructed images from mSPECS-IPA, mSPECS-IPA-CAIPIRINHA, mSPECS-IPA-VAT, and mSPECS-IPA-CAIPIVAT model with different through-plane acceleration factors.

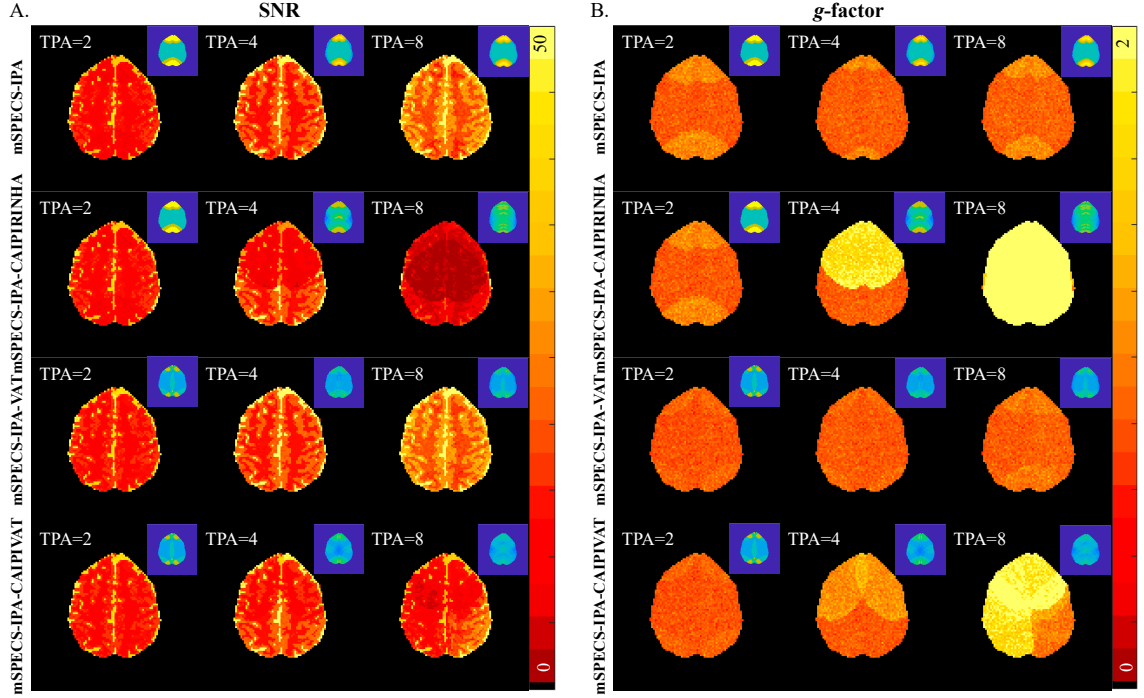


Figure 5.22: A. The SNR value of slice 3 from reconstructed images for mSPECS-IPA, mSPECS-IPA-CAIPIRINHA, mSPECS-IPA-VAT, and mSPECS-IPA-CAIPIVAT model with different TPA factor. B. The g -factor value of slice 3 from reconstructed images for mSPECS-IPA, mSPECS-IPA-CAIPIRINHA, mSPECS-IPA-VAT, and mSPECS-IPA-CAIPIVAT model with different TPA factor.

We also investigated the signal-to-noise ratio (SNR) and the geometric factor g -factor values across mSPECS-IPA, mSPECS-IPA-CAIPIRINHA, mSPECS-IPA-VAT, and mSPECS-IPA-CAIPIVAT models. The SNR can be calculated as $SNR = \beta_0 / \sigma_N$, where β_0 represents the baseline signal for each location of the brain image, and σ_N represents the standard deviation of the noise. The higher the SNR value is, the better performance of the model. According to the definition of g -factor (equation 3.1) in Chapter 3.1.1, the through-plane acceleration factor also need to be incorporated into it. Thus, the g -factor can be calculated as $g_{accelerate} = \sqrt{N_s} SNR_{full} / SNR_{accelerate} \sqrt{R}$, where $R = 2$ indicating the in-plane acceleration factor. The closer g -factor is to 1, the better reconstructed results the model will produce. Figure 5.22A shows the SNR value of slice 3 for four models with different through-plane acceleration factors. The top right corner is the slice overlapping situation corresponding to average of the

first N_α time point for each model. As the TPA factor increases, the SNR value for the mSPECS-IPA and mSPECS-IPA-VAT models also increases. Moreover, in the mSPECS-IPA-VAT model, both the posterior and anterior regions of the brain exhibit higher SNR values compared to the mSPECS-IPA model. In contrast, for the mSPECS-IPA-CAIPIRINHA and mSPECS-IPA-CAIPIVAT models, the SNR value does not increase evenly across the entire brain image as the TPA factor increases. In the mSPECS-IPA-CAIPIRINHA model, at higher TPA factors, the SNR in the middle brain region is lower than at lower TPA factors. A similar pattern is observed in the left side of the brain image in the mSPECS-IPA-CAIPIVAT model. Figure 5.22B shows the g -factor of slice 3 across different models with varying through-plane acceleration factors. As the TPA factor increases, the g -factor in the mSPECS-IPA-CAIPIRINHA and mSPECS-IPA-CAIPIVAT models increases dramatically, whereas in the mSPECS-IPA and mSPECS-IPA-VAT models, it increases only slightly. Comparing the g -factor values between the mSPECS-IPA and mSPECS-IPA-VAT models, the g -factor in the mSPECS-IPA-VAT model is closer to 1 in both the posterior and anterior regions of the brain.

5.3.2 Task Simulated Reconstruction Results

In order to investigate the task activation detection performance of each model, we applied the novel image shift SMS techniques to the simulated right-handed finger tapping experiment with the same in-plane acceleration factor, IPA=2, and different through-plane acceleration factors TPA=2, TPA=4, and TPA=8. For each voxel in the brain image, the signal can be expressed as $y = \beta_0 + \beta_1 x + \epsilon$, where β_0 is the baseline signal of the voxel, β_1 is the task signal, x is a vector with elements 0 and 1 indicating each time point with or without task activation. Therefore, the contrast-to-noise ratio (CNR) can be calculated as $CNR = \beta_1/\sigma_N$, and same as the definition in SNR , σ_N stands for the standard deviation of the noise. The activation detec-

tion rate for each model was also investigated by applying a complex-valued model to compute fMRI activation (Rowe and Logan (2004)). Figure 5.23 shows the average and standard deviation of the *CNR* values in the region of interest (ROI) from the mSPECS-IPA, mSPECS-IPA-CAIPIRINHA, mSPECS-IPA-VAT, and mSPECS-IPA-CAIPIVAT models with an acceleration factor of $TPA = 2$. The *CNR* value of the ROI for slice 1 in the mSPECS-IPA-VAT and mSPECS-IPA-CAIPIVAT models is slightly higher than in the mSPECS-IPA and mSPECS-IPA-CAIPIRINHA models. Meanwhile, the *CNR* value of the ROI for slice 3 is similar across all four models. Figure 5.24 shows the average task activation detection rate in the ROI from the mSPECS-IPA, mSPECS-IPA-CAIPIRINHA, mSPECS-IPA-VAT, and mSPECS-IPA-CAIPIVAT models with $TPA = 2$. Compared to the models with a horizontal image shift, mSPECS-IPA-VAT and mSPECS-IPA-CAIPIVAT, the models without horizontal image shift, mSPECS-IPA and mSPECS-IPA-CAIPIRINHA, exhibit a lower average z-score in the ROI. This indicates that the activation detection ability of mSPECS-IPA and mSPECS-IPA-CAIPIRINHA is lower than that of the mSPECS-IPA-VAT and mSPECS-IPA-CAIPIVAT models.

To assess the influence of a high acceleration factor on the task activation detection ability of each model, we compared the *CNR* value and the task activation detection rate of ROI for mSPECS-IPA, mSPECS-IPA-CAIPIRINHA, mSPECS-IPA-VAT, and mSPECS-IPA-CAIPIVAT models under different acceleration factors, $TPA = 2$, $TPA = 4$, and $TPA = 8$. Figure 5.25A shows the average *CNR* value in the ROI of slice 3 for the mSPECS-IPA, mSPECS-IPA-CAIPIRINHA, mSPECS-IPA-VAT, and mSPECS-IPA-CAIPIVAT models with different acceleration factors. As the acceleration factor increases, the average *CNR* value decreases across all four models. However, at high acceleration factors, the average *CNR* value in the ROI is higher in the mSPECS-IPA and mSPECS-IPA-VAT models compared to the models incorporating vertical image shift, mSPECS-IPA-CAIPIRINHA and mSPECS-IPA-

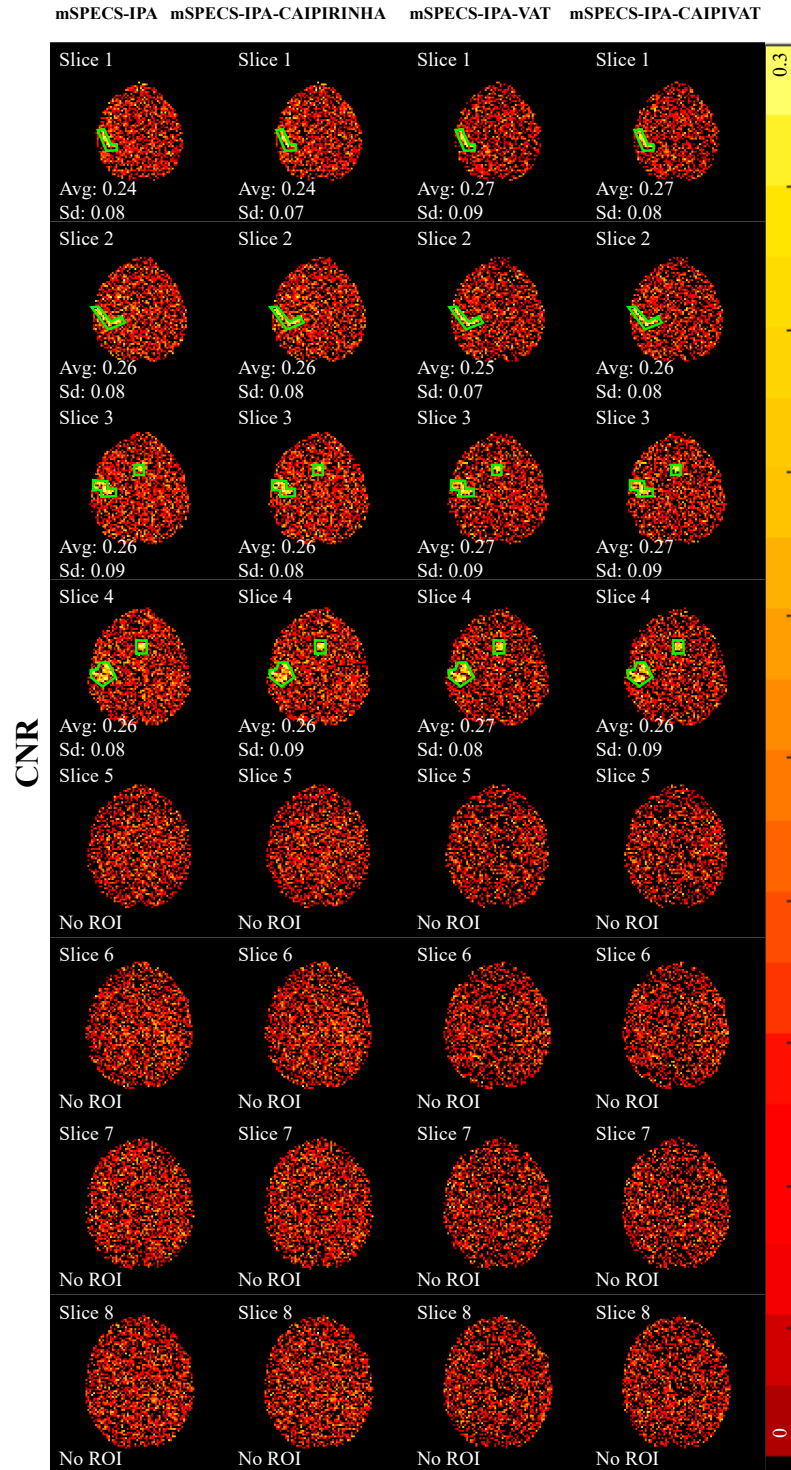


Figure 5.23: The average *CNR* value of ROI for with acceleration factor $TPA=2$ from mSPECS-IPA, mSPECS-IPA-CAIPIRINHA, mSPECS-IPA-VAT, and mSPECS-IPA-CAIPIVAT model.

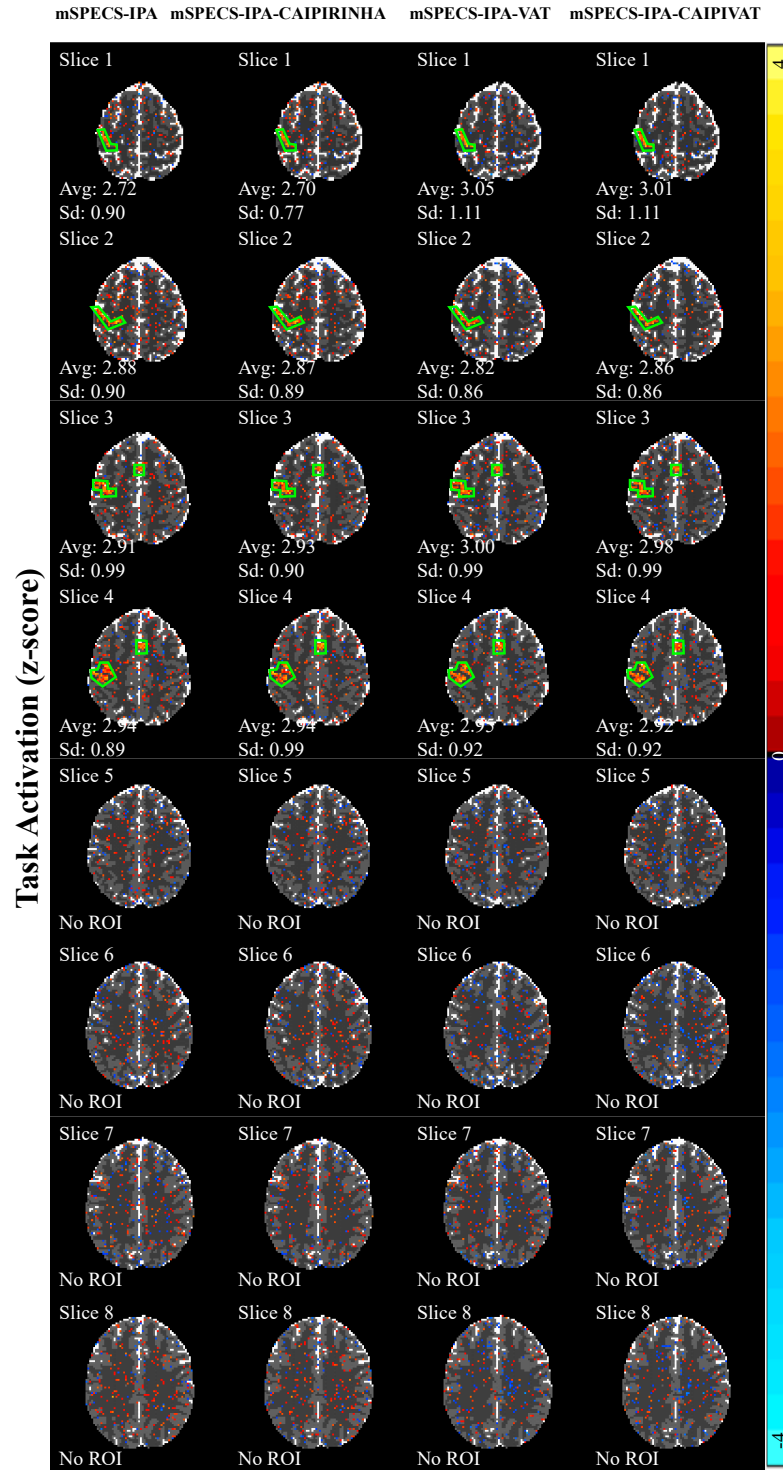


Figure 5.24: The average task activation rate (z-score) of ROI for with acceleration factor TPA=2 from mSPECS-IPA, mSPECS-IPA-CAIPIRINHA, mSPECS-IPA-VAT, and mSPECS-IPA-CAIPIVAT model.

CAIPIVAT. Among these models, the model applies image shift only along the vertical direction, mSPECS-IPA-CAIPIRINHA exhibits the lowest average *CNR* value in the ROI. Figure 5.25B shows the activation detection rate (z-score) in the ROI of slice 3 for the mSPECS-IPA, mSPECS-IPA-CAIPIRINHA, mSPECS-IPA-VAT, and mSPECS-IPA-CAIPIVAT models with different acceleration factors. As the acceleration factor increases, it becomes more difficult to capture the entire simulated activation blocks across all four models. However, at $TPA = 8$, the models without vertical image shift, mSPECS-IPA and mSPECS-IPA-VAT, exhibit higher average z-scores in the ROI compared to the models with vertical image shift, mSPECS-IPA-CAIPIRINHA and mSPECS-IPA-CAIPIVAT. Although the models incorporating vertical image shift exhibit lower average z-scores in the ROI, the mSPECS-IPA-CAIPIVAT model achieves a higher average z-score compared to the mSPECS-IPA-CAIPIRINHA model. Among all models, mSPECS-IPA-CAIPIRINHA provides the lowest activation detection rate, indicating that it has the least ability to capture the simulated task activation blocks.

5.4 GRAPPA Approach for mSPECS-IPA-CAIPIVAT

5.4.1 Non-Task Simulated Reconstruction Results

Following the methodology of the GRAPPA approach for the mSPECS-IPA-CAIPIVAT technique, as presented in Chapter 4.2, we applied the GRAPPA technique in conjunction with novel SMS multi-directional image shift techniques, using an in-plane acceleration factor of $IPA = 2$ and varying through-plane acceleration factors of $TPA = 2$, $TPA = 4$, and $TPA = 8$. The reconstructed results were compared between GRAPPA for mSPECS-IPA model (without image shift technique), GRAPPA for mSPECS-IPA-CAIPIRINHA model (image shift along vertical direction), GRAPPA for mSPECS-IPA-VAT model (image shift along horizontal direction), and GRAPPA for mSPECS-IPA-CAIPIVAT (image shift along vertical and horizontal direction). The reconstructed results were also compared with the true

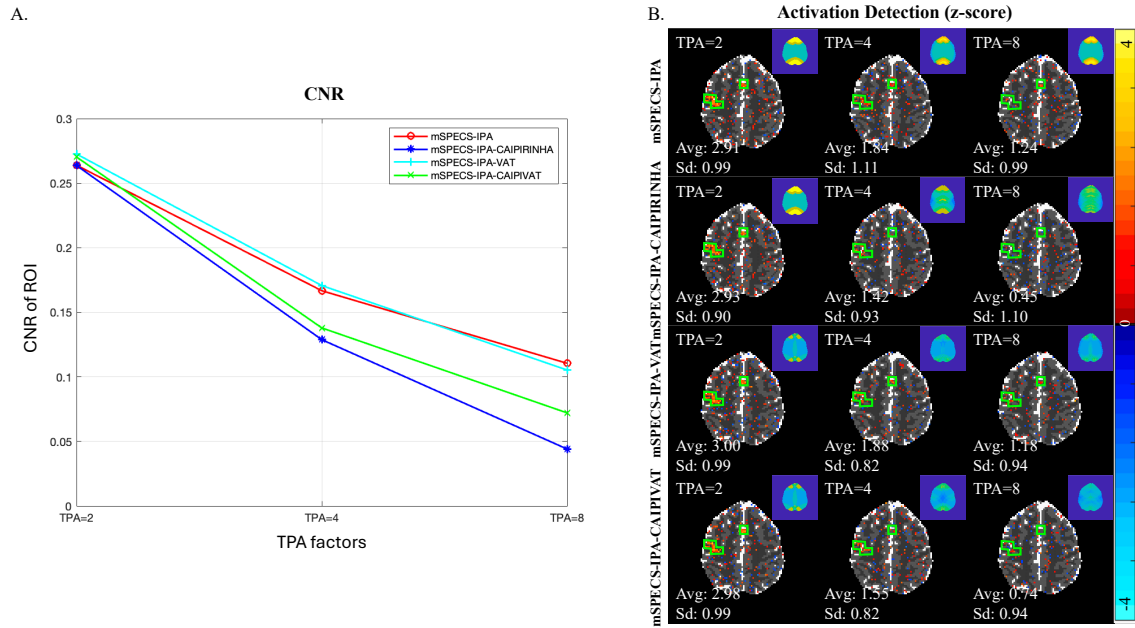


Figure 5.25: A. The average *CNR* value of ROI for slice 3 from mSPECS-IPA, mSPECS-IPA-CAIPIRINHA, mSPECS-IPA-VAT, and mSPECS-IPA-CAIPIVAT model with acceleration factor TPA=2, TPA=4, and TPA=8. B. The average activation detection rate (z-score) of ROI for slice 3 from mSPECS-IPA, mSPECS-IPA-CAIPIRINHA, mSPECS-IPA-VAT, and mSPECS-IPA-CAIPIVAT model with acceleration factor TPA=2, TPA=4, and TPA=8.

noiseless simulated images. Figure 5.26 and Figure 5.27 shows the mean magnitude and phase of the reconstructed images from GRAPPA approach for mSPECS-IPA, GRAPPA approach for mSPECS-IPA-CAIPIRINHA, GRAPPA approach for mSPECS-IPA-VAT, and GRAPPA approach for mSPECS-IPA-CAIPIVAT, and compared with the magnitude and phase from true simulated images with $IPA = 2$ and $TPA = 2$ situation. As shown in these figures, the mean magnitude of the reconstructed images from all four models closely resembles the true noiseless magnitude images. Similarly, the mean phase of the reconstructed images is consistent with the true noiseless phase images within the brain region. However, Figure 5.27 reveals phase residues outside the brain images in models incorporating vertical image shift techniques, namely mSPECS-IPA-CAIPIRINHA and mSPECS-IPA-CAIPIVAT. These phase residues arise because the image shift direction aligns with the in-plane

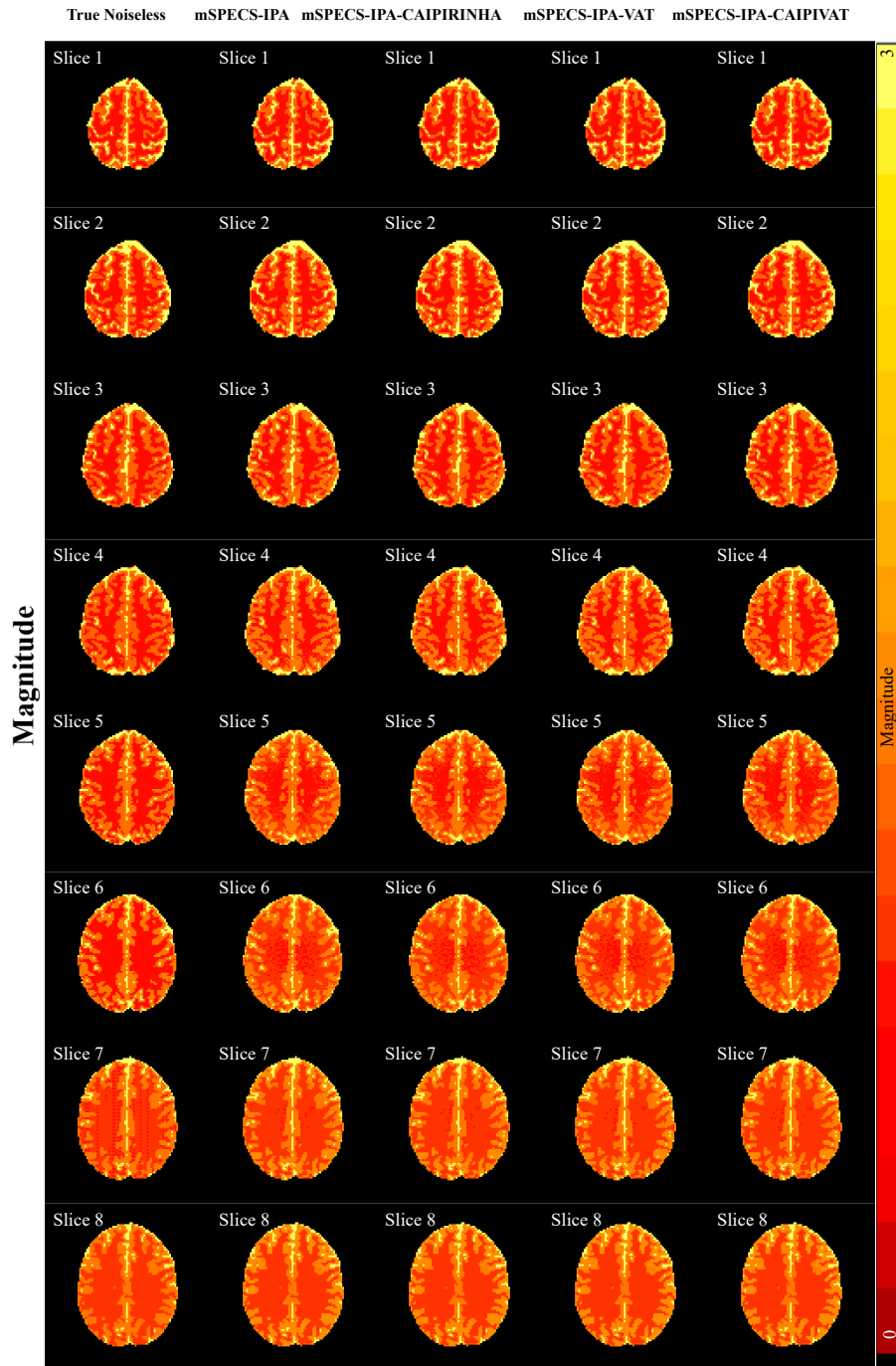


Figure 5.26: The magnitude of the reconstructed images from GRAPPA approach for mSPECS-IPA, GRAPPA approach for mSPECS-IPA-CAIPIRINHA, GRAPPA approach for mSPECS-IPA-VAT, and GRAPPA approach for mSPECS-IPA-CAIPIVAT, compared with the magnitude from true noiseless simulated images with $TPA=2$.

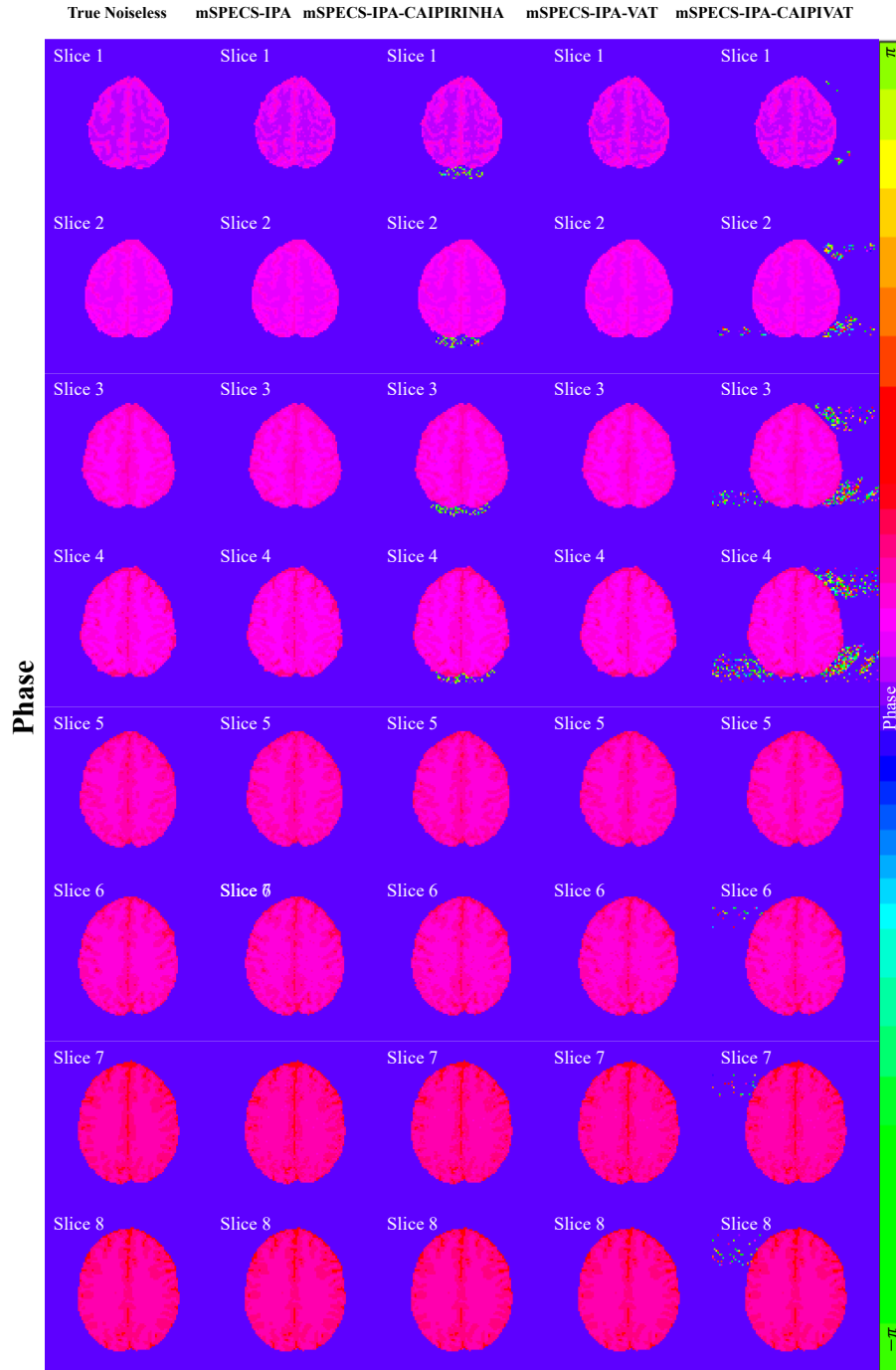


Figure 5.27: The phase of the reconstructed images from GRAPPA approach for mSPECS-IPA, GRAPPA approach for mSPECS-IPA-CAIPIRINHA, GRAPPA approach for mSPECS-IPA-VAT, and GRAPPA approach for mSPECS-IPA-CAIPIVAT, compared with the phase from true noiseless simulated images with TPA=2.

Variance of Task Signal

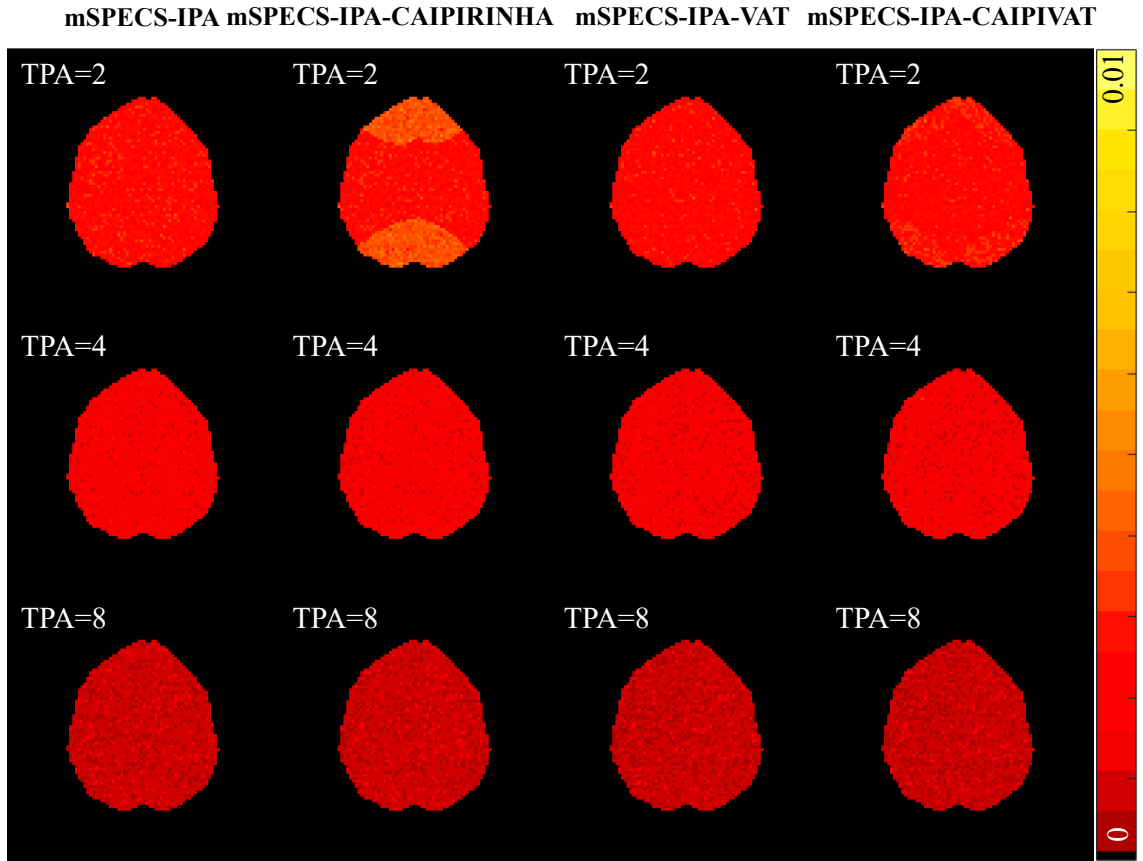


Figure 5.28: The task regression coefficient variance of slices 3 from reconstructed images from GRAPPA for mSPECS-IPA, GRAPPA for mSPECS-IPA-CAIPIRINHA, GRAPPA for mSPECS-IPA-VAT, and GRAPPA for mSPECS-IPA-CAIPIVAT model with different through-plane acceleration factors.

acceleration technique.

Similar to the previous chapter, we also investigated the variance of the task signal from the reconstructed brain images. Figure 5.28 displays the task regression coefficient variance of slices 3 from reconstructed images from GRAPPA for mSPECS-IPA, GRAPPA for mSPECS-IPA-CAIPIRINHA, GRAPPA for mSPECS-IPA-VAT, and GRAPPA for mSPECS-IPA-CAIPIVAT model with in-plane acceleration factor $IPA = 2$ and different through-plane acceleration factors, $TPA = 2$, $TPA = 4$, and $TPA = 8$. As shown in Figure 5.28, as the through-plane acceleration factor

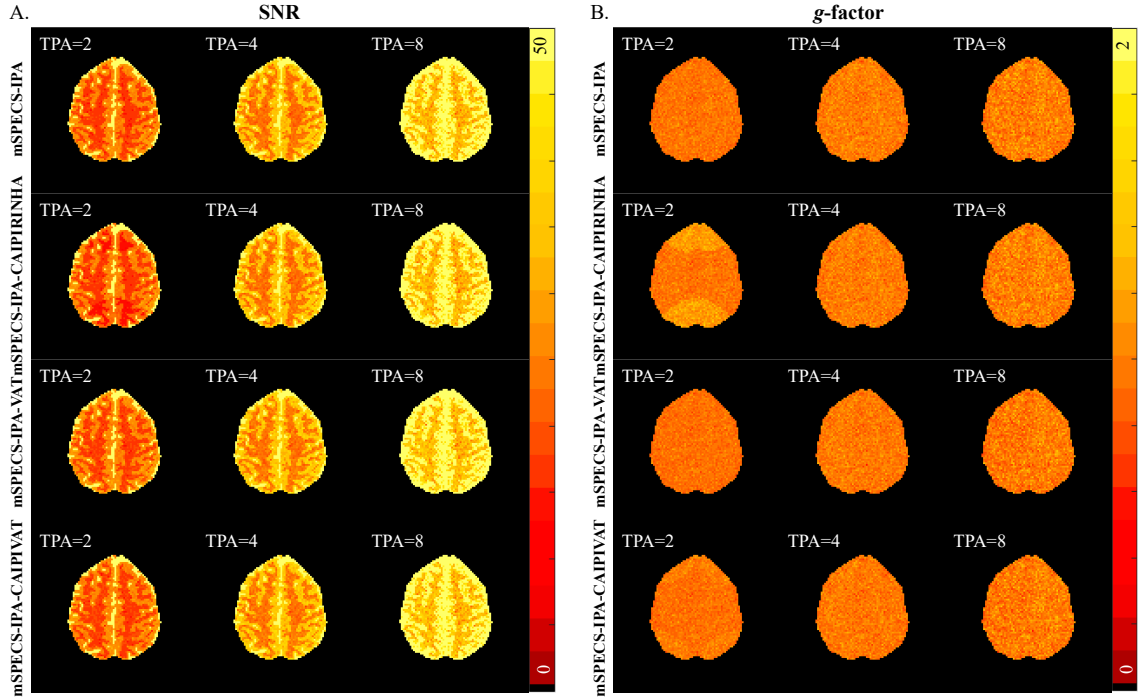


Figure 5.29: A. The SNR value of slice 3 from reconstructed images for GRAPPA for mSPECS-IPA, GRAPPA for mSPECS-IPA-CAIPIRINHA, GRAPPA for mSPECS-IPA-VAT, and GRAPPA for mSPECS-IPA-CAIPIVAT model with different TPA factor. B. The g -factor value of slice 3 from reconstructed images for GRAPPA for mSPECS-IPA, GRAPPA for mSPECS-IPA-CAIPIRINHA, GRAPPA for mSPECS-IPA-VAT, and GRAPPA for mSPECS-IPA-CAIPIVAT model with different TPA factor.

TPA increases, the variance of the task signal decreases. However, when comparing the variance of the task signal across different models, the GRAPPA for mSPECS-IPA-CAIPIVAT model exhibits the lowest variance among the four models. Moreover, compared to the variance of the task signal from the mSPECS-IPA-CAIPIVAT model (Figure 5.17), the variance of the task signal from the GRAPPA for mSPECS-IPA-CAIPIVAT model (Figure 5.28) is lower. This difference is particularly evident when incorporating vertical image shift techniques, the mSPECS-IPA-CAIPIRINHA and mSPECS-IPA-CAIPIVAT models, where the variance of the task signal from the GRAPPA approach remains lower at high through-plane acceleration factors.

We also investigated the signal-to-noise ratio (SNR) and the geometric factor

g -factor values between GRAPPA for mSPECS-IPA, GRAPPA for mSPECS-IPA-CAIPIRINHA, GRAPPA for mSPECS-IPA-VAT, and GRAPPA for mSPECS-IPA-CAIPIVAT models. The SNR can be calculated as $SNR = \beta_0/\sigma_N$, where β_0 represents the baseline signal for each location of the brain image, and σ_N represents the standard deviation of the noise. The higher the SNR value is, the better performance of the model. The g -factor is same as the definition in Chapter 3.1.1, and can be calculated as $g_{accelerate} = \sqrt{N_s}SNR_{full}/SNR_{accelerate}\sqrt{R}$, where $R = 2$ indicating the in-plane acceleration factor. The closer g -factor is to 1, the better reconstructed results the model will produce. Figure 5.29A shows the SNR value of slice 3 for four models with an in-plane acceleration factor of $IPA = 2$ and different through-plane acceleration factors: $TPA = 2$, $TPA = 4$, and $TPA = 8$. As the TPA factor increases, the SNR value of the reconstructed brain images from all four models also increases. Moreover, the GRAPPA approach applied to the novel SMS techniques yields a higher SNR value than the mSPECS-IPA-CAIPIVAT model (Figure 5.22). When the TPA factor is high, the SNR images do not exhibit overlapping artifacts in models incorporating the vertical image shift technique, mSPECS-IPA-CAIPIRINHA and mSPECS-IPA-CAIPIVAT, when using the GRAPPA approach. Figure 5.29B shows the g -factor of slice 3 for four models with an in-plane acceleration factor of $IPA = 2$ and different through-plane acceleration factors: $TPA = 2$, $TPA = 4$, and $TPA = 8$. As seen in Figure 5.29B, compared to the g -factor from the mSPECS-IPA-CAIPIVAT model (Figure 5.22), the g -factor from the GRAPPA approach remains stable as the TPA factor increases. Moreover, the g -factor from the model incorporating the vertical image shift technique in the GRAPPA approach does not exhibit overlapping artifacts, unlike the g -factor images from the mSPECS-IPA-CAIPIRINHA and mSPECS-IPA-CAIPIVAT models shown in Figure 5.22.

5.4.2 Task Simulated Reconstruction Results

We also investigated the task activation detection performance of each model. We applied the GRAPPA approach of the novel SMS techniques incorporating with different directional image shift techniques to the simulated right-handed finger tapping experiment with the same in-plane acceleration factor, $IPA = 2$, and different through-plane acceleration factors $TPA = 2$, $TPA = 4$, and $TPA = 8$. Similar to the previous two models, for each voxel in the brain image, the signal can be expressed as $y = \beta_0 + \beta_1 x + \epsilon$, where β_0 is the baseline signal of the voxel, β_1 is the task signal, x is a vector with elements 0 and 1 indicating each time point with or without task activation. Therefore, the contrast-to-noise ratio (CNR) can be calculated as $CNR = \beta_1/\sigma_N$, and same as the definition in SNR , σ_N stands for the standard deviation of the noise. The activation detection rate for each model was also investigated by applying a complex-valued model to compute fMRI activation (Rowe and Logan (2004)). Figure 5.30 shows the average and standard deviation of the CNR values in the region of interest (ROI) for the GRAPPA approach for mSPECS-IPA, mSPECS-IPA-CAIPIRINHA, mSPECS-IPA-VAT, and mSPECS-IPA-CAIPIVAT models, with an acceleration factor of $IPA = 2$ and $TPA = 2$. As shown in Figure 5.30, the average CNR values in the ROI are very similar across the four models. Moreover, when comparing the average CNR values in the ROI from the mSPECS-IPA, mSPECS-IPA-CAIPIRINHA, mSPECS-IPA-VAT, and mSPECS-IPA-CAIPIVAT models in Figure 5.23, the average CNR values from the models incorporating the GRAPPA technique are slightly lower under the $IPA = 2$ and $TPA = 2$ condition. Figure 5.31 shows the average task activation detection rate in the ROI for the GRAPPA approach for mSPECS-IPA, mSPECS-IPA-CAIPIRINHA, mSPECS-IPA-VAT, and mSPECS-IPA-CAIPIVAT models with $IPA = 2$ and $TPA = 2$. A similar conclusion can be drawn from Figure 5.31. The average task activation detection rate in the ROI for the novel SMS techniques incorporating the GRAPPA technique is

nearly identical across models, and it is also slightly lower than the average task activation detection rate in the ROI for the mSPECS-IPA, mSPECS-IPA-CAIPIRINHA, mSPECS-IPA-VAT, and mSPECS-IPA-CAIPIVAT models in Figure 5.24 under the $IPA = 2$ and $TPA = 2$ condition.

Similar to previous chapters, to assess the influence of a high acceleration factor on the task activation detection ability of each model, we also compared the CNR value and the task activation detection rate of ROI for GRAPPA for mSPECS-IPA, GRAPPA for mSPECS-IPA-CAIPIRINHA, GRAPPA for mSPECS-IPA-VAT, and GRAPPA for mSPECS-IPA-CAIPIVAT models under in-plane acceleration factor $IPA = 2$, and different acceleration factors, $TPA = 2$, $TPA = 4$, and $TPA = 8$. Figure 5.32A shows the average CNR value in the ROI of slice 3 for the GRAPPA-applied mSPECS-IPA, mSPECS-IPA-CAIPIRINHA, mSPECS-IPA-VAT, and mSPECS-IPA-CAIPIVAT models with different acceleration factors. As the acceleration factor increases, the average CNR value decreases across all four models. However, compared to the average CNR value in the ROI for the mSPECS-IPA-CAIPIRINHA and mSPECS-IPA-CAIPIVAT models in Figure 5.25A, the average CNR value in the ROI for the novel SMS techniques incorporating the GRAPPA approach is higher, especially at high through-plane acceleration factors. Moreover, at high acceleration factors, the GRAPPA approach for mSPECS-IPA-CAIPIVAT exhibits a higher average CNR value in the ROI compared to the other models. Figure 5.32B shows the average activation detection rate (z-score) in the ROI of slice 3 for the GRAPPA-applied mSPECS-IPA, mSPECS-IPA-CAIPIRINHA, mSPECS-IPA-VAT, and mSPECS-IPA-CAIPIVAT models with different acceleration factors. Similar to what was observed in the mSPECS-IPA-CAIPIVAT model, as the acceleration factor increases, it becomes more challenging to capture the entire simulated activation blocks across all four models. However, compared to the average activation detection rate in the ROI for the mSPECS-IPA-CAIPIRINHA and mSPECS-IPA-CAIPIVAT models in Figure 5.25B,

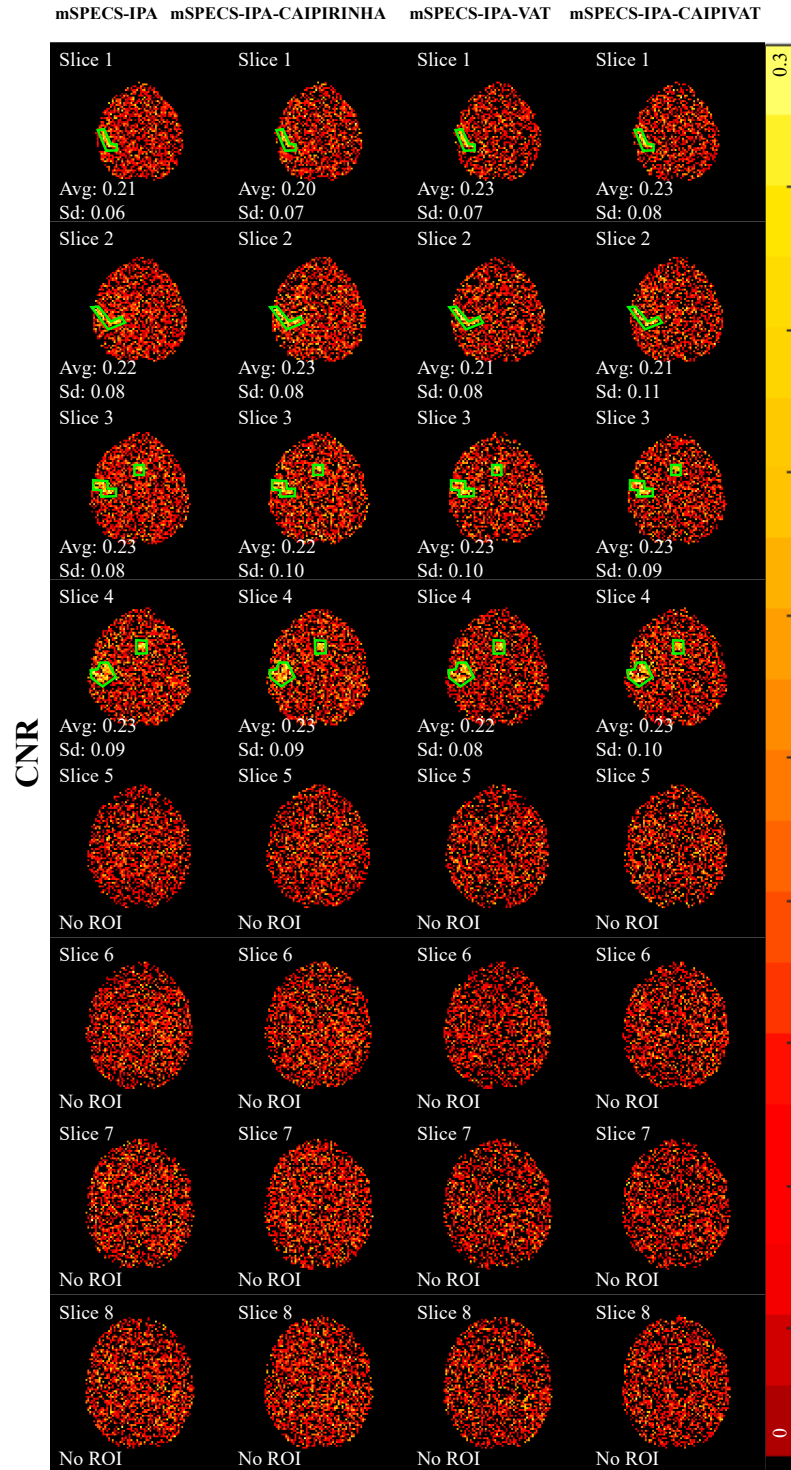


Figure 5.30: The average CNR value of ROI for with acceleration factor $TPA=2$ situation from GRAPPA for mSPECS-IPA, GRAPPA for mSPECS-IPA-CAIPIRINHA, GRAPPA for mSPECS-IPA-VAT, and GRAPPA for mSPECS-IPA-CAIPIVAT model.

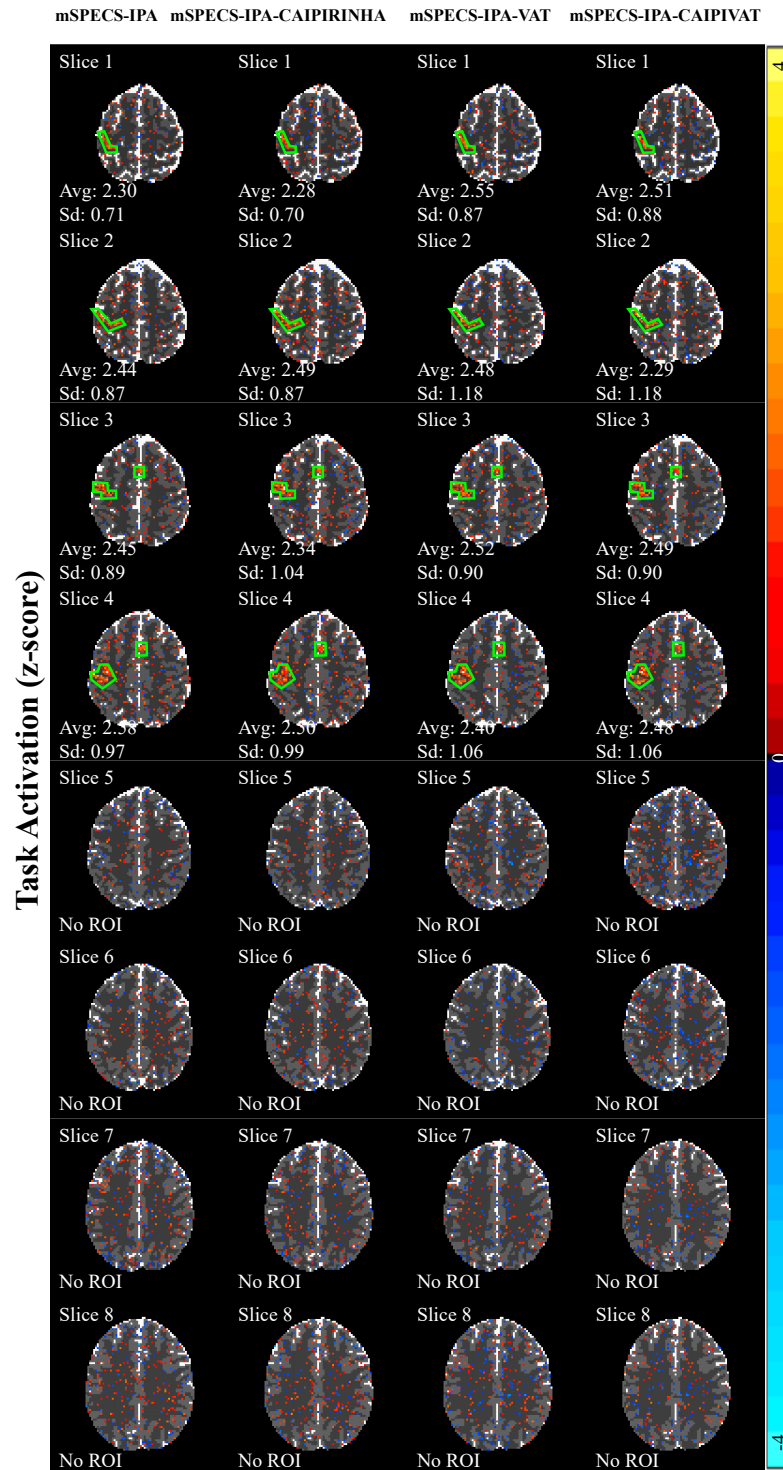


Figure 5.31: The average task activation rate (z-score) of ROI for with acceleration factor TPA=2 from GRAPPA for mSPECS-IPA, GRAPPA for mSPECS-IPA-CAIPIRINHA, GRAPPA for mSPECS-IPA-VAT, and GRAPPA for mSPECS-IPA-CAIPIVAT model.

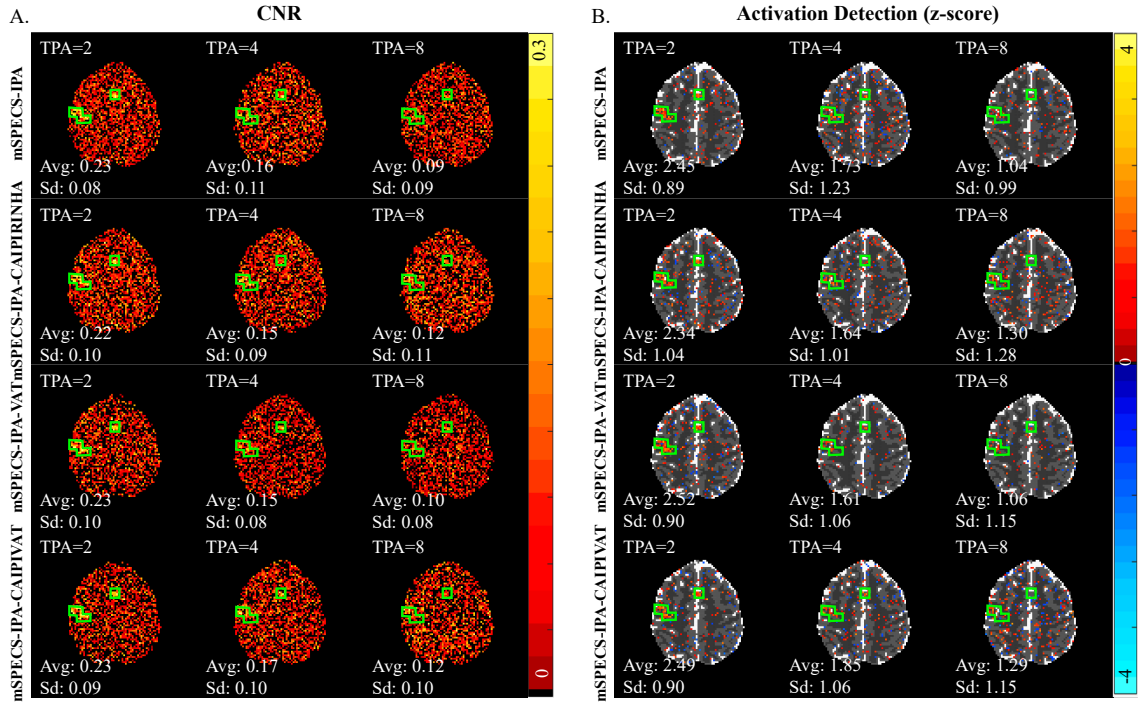


Figure 5.32: A. The average *CNR* value of ROI for slice 3 from GRAPPA for mSPECS-IPA, GRAPPA for mSPECS-IPA-CAIPIRINHA, GRAPPA for mSPECS-IPA-VAT, and GRAPPA for mSPECS-IPA-CAIPIVAT model with acceleration factor $TPA = 2$, $TPA = 4$, and $TPA = 8$. B. The average activation detection rate (*z*-score) of ROI for slice 3 from GRAPPA for mSPECS-IPA, GRAPPA for mSPECS-IPA-CAIPIRINHA, GRAPPA for mSPECS-IPA-VAT, and GRAPPA for mSPECS-IPA-CAIPIVAT model with acceleration factor $TPA = 2$, $TPA = 4$, and $TPA = 8$.

the average activation detection rate in the ROI for the novel SMS techniques incorporating the GRAPPA approach is higher, particularly at high through-plane acceleration factors. Additionally, at high acceleration factors, the GRAPPA approach for mSPECS-IPA-CAIPIVAT exhibits a higher average activation detection rate in the ROI compared to the other models. Thus, among these four GRAPPA incorporated SMS image shift techniques, the GRAPPA approach for mSPECS-IPA-CAIPIVAT is the most effective model for capturing the task signal at high acceleration factors.

CHAPTER 6: EXPERIMENTAL RECONSTRUCTION RESULTS

We also investigate performance and compare the *in vivo* reconstructed results of the three approaches. The mSPECS-CAIPIVAT, mSPECS-IPA-CAIPIVAT, and the GRAPPA approach for the mSPECS-IPA-CAIPIVAT model are applied to experimental fMRI data.

6.1 Experimental fMRI Data

The real-world right-handed finger tapping fMRI experiment for a single object was executed through a 3.0 T General Electric Signa LX MRI scanner. The flip angle is 90° and the acquisition bandwidth is 125kHz in this experiment. The slice thickness for the axial brain images is 2.5 mm. A total of nine slices were scanned. However, since the dimension of the Hadamard and 2D Hadamard aliasing coefficient must be a power of two, only eight slices were used in the proposed image-shifted SMS techniques, with the most inferior axial brain slice disregarded. In this experiment, an 8 channel receiver head coil was utilized with dimension 96×96 for a 24 cm full field-of-view, with the phase encoding direction from posterior to anterior. In the real-world right-handed finger tapping fMRI experiment, two fMRI time series were acquired: the non-task calibration time series and the task time series. The right-handed finger tapping experiment was designed with an initial 20s off rest, followed by 15s off and 15s on for 16 epochs, and the final 10s of rest, resulting in a total 510s for the task time series. The first 20s of the task time series were disregarded to achieve a steady magnetic field of the scanner, resulting in last 490s of the task time series were applied to the novel proposed model.

The same acceleration factors from the simulated fMRI time series were applied in the real-world right-handed finger tapping experiment with $IPA = 2$, and $TPA = 2, 4, 8$. The same net acceleration factors were achieved in the real-world

experimental time series. The mSPECS-CAIPIVAT, mSPECS-IPA-CAIPIVAT and GRAPPA approach for mSPECS-IPA-CAIPIVAT were applied to the right-handed finger tapping experiment fMRI time series. The SENSE method was also applied to the calibration fMRI time series, and the reconstructed images were utilized as the reference images. The reconstructed results from the novel image shift SMS technique were compared with the reference images. All of the reconstruction and the analysis process were finished through the MATLAB programming software.

6.2 mSPECS-CAIPIVAT

6.2.1 Non-Task Experimental Reconstruction Results

In order to investigate the performance of the new slice-wise image shift SMS models on a real-world experiment, we applied mSPECS-VAT, mSPECS-CAIPIRINHA and mSPECS-CAIPIVAT model to the right-handed finger-tapping fMRI experiment time series. Reconstructed axial brain images were obtained from these three image shifting models and compared with the reconstruction results from SENSE and mSPECS models; reference images were also included in the comparison. We also investigated the model performance of the new slice-wise image shift models with different acceleration factors $TPA=2$, $TPA=4$ and $TPA=8$, and compared the reconstruction results with the SENSE and mSPECS model. Figure 6.1 and Figure 6.2 show the temporal mean magnitude and mean phase of the reconstructed images from the reference, SENSE, mSPECS, mSPECS-VAT, mSPECS-CAIPIRINHA, and mSPECS-CAIPIVAT model for odd slices with acceleration factor $TPA = 2$. From Figure 6.1 and Figure 6.2, compared with the reference brain images, the reconstructed images from the SENSE model exhibit strong signal leakage from aliased slices, making anatomical structures difficult to discern. In contrast, the reconstructed images from the mSPECS, mSPECS-VAT, mSPECS-CAIPIRINHA, and mSPECS-CAIPIVAT models closely resemble the reference images, with clear anatomical struc-

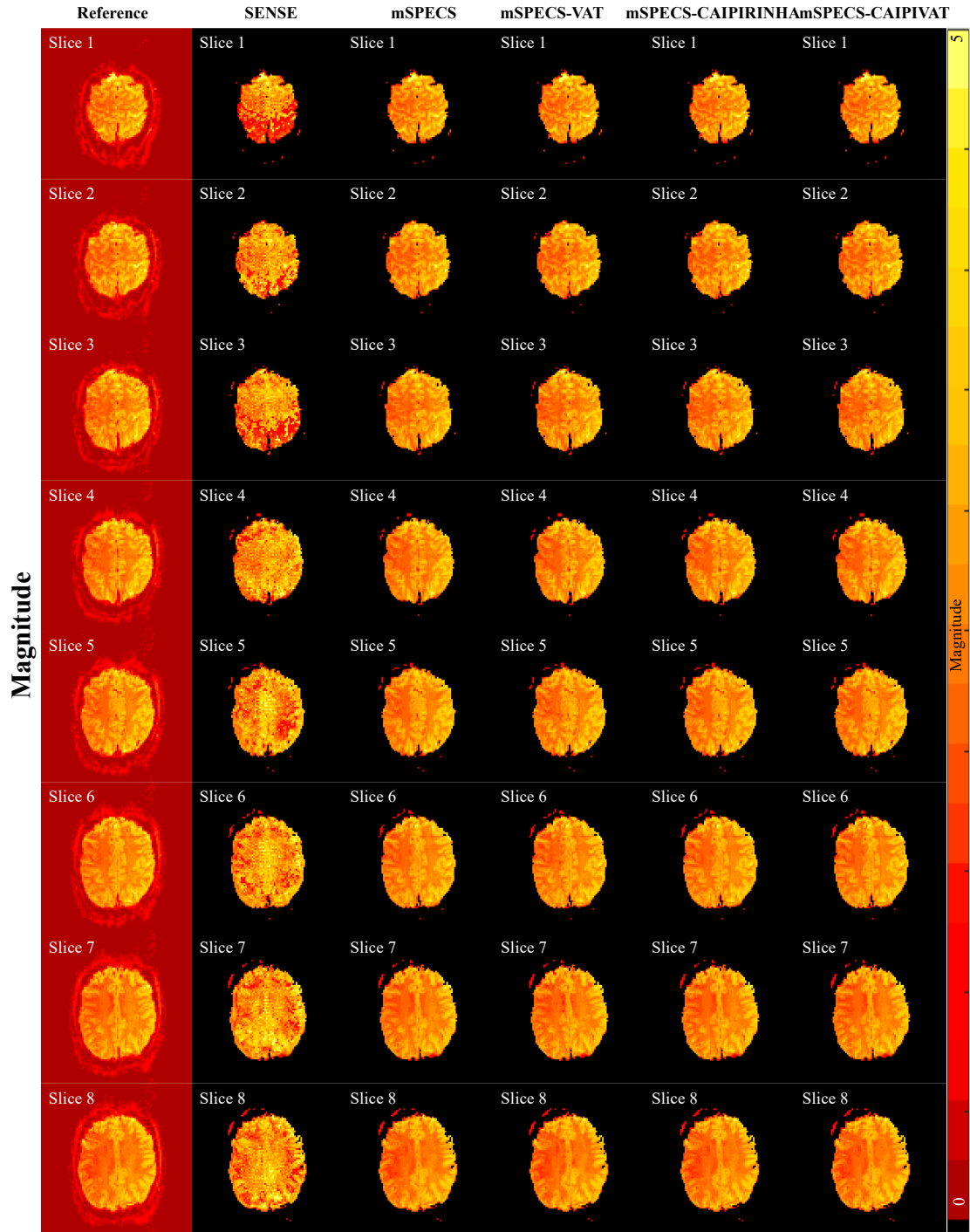


Figure 6.1: The temporal mean magnitude of the axial brain images from the reference, SENSE, mSPECS, mSPECS-VAT, mSPECS-CAIPIRINHA, and mSPECS-CAIPIVAT with acceleration factor TPA=2.

tures.

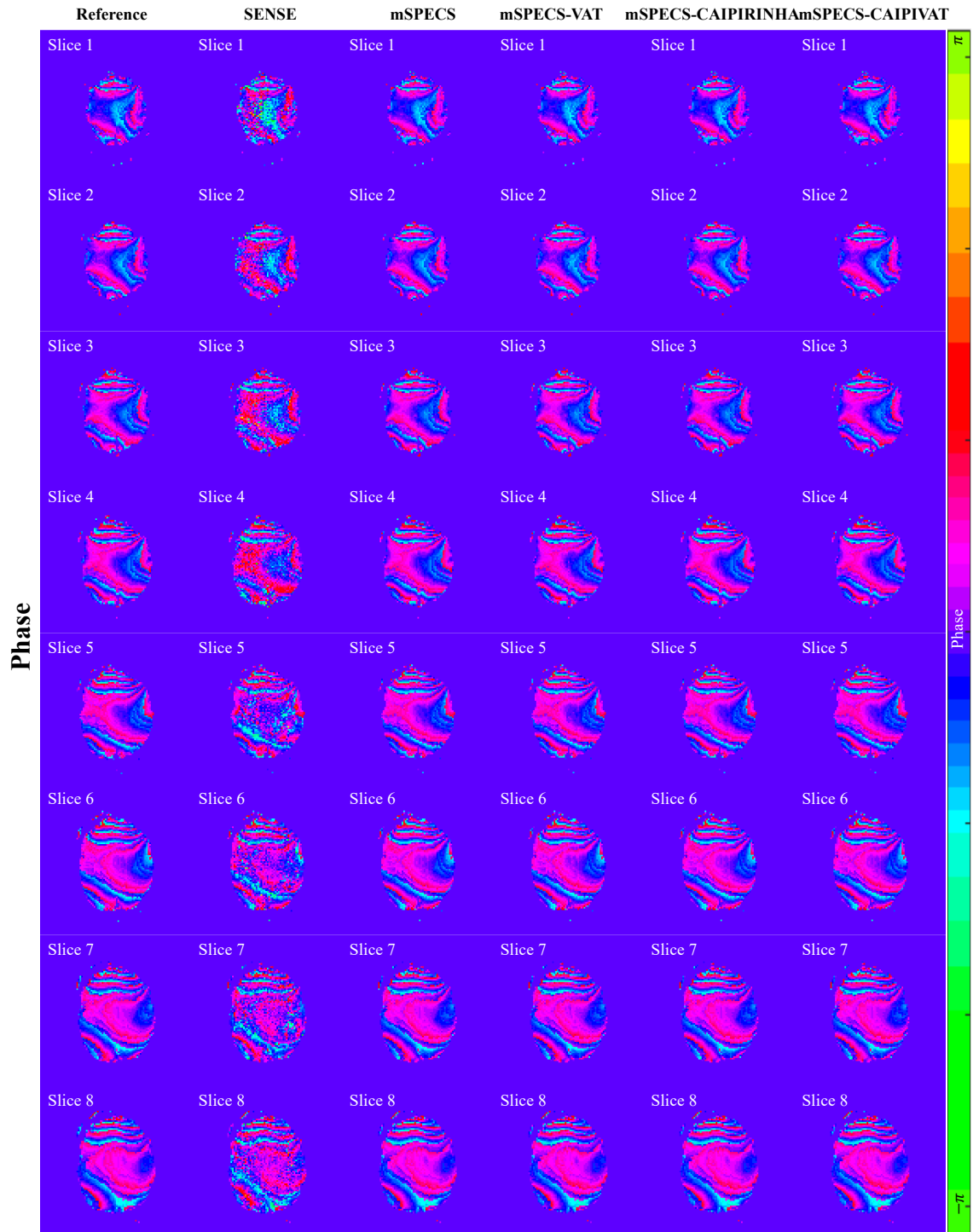


Figure 6.2: The temporal mean phase of the axial brain images from the reference, SENSE, mSPECS, mSPECS-VAT, mSPECS-CAIPIRINHA, and mSPECS-CAIIVAT with acceleration factor TPA=2.

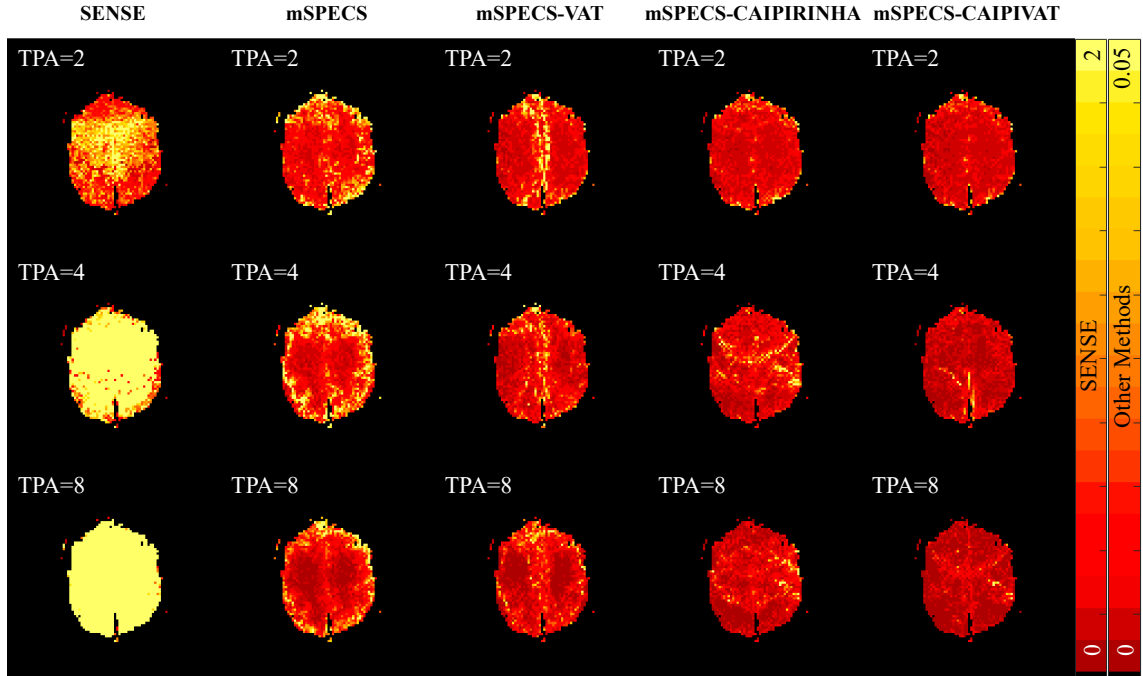


Figure 6.3: The temporal variance of SENSE, mSPECS, mSPECS-VAT, mSPECS-CAIPIRINHA, and mSEPCS-CAIPIVAT model with different acceleration factors of slice 3.

Figure 6.3 shows the temporal variance of the task signal of the reconstructed images from SENSE, mSPECS, mSPECS-VAT, mSPECS-CAIPIRINHA, and mSEPCS-CAIPIVAT model with different acceleration factors of slice 3. From Figure 6.3, we observe that the temporal variance from the SENSE model increases with increasing acceleration factor, whereas the temporal variance from the mSPECS, mSPECS-VAT, mSPECS-CAIPIRINHA, and mSPECS-CAIPIVAT models decreases as the acceleration factor increases. Furthermore, when comparing the mSPECS model with the three slice-wise image shift techniques, the mSPECS-VAT, the mSPECS-CAIPIRINHA and mSPECS-CAIPIVAT models provide lower temporal variance, with the mSPECS-CAIPIVAT model yielding the lowest temporal variance results.

Similar to the simulation reconstruction results, we also investigated the *SNR* and *g*-factor values of the reconstructed axial brain images of the four models. Fig. 6.4 shows the average and standard deviation of *SNR* and *g*-factor values of the ROI of

reconstructed images for SENSE, mSPECS, mSPECS-VAT, mSPECS-CAIPIRINHA, and mSPECS-CAIPIVAT model with different acceleration factors. From Figure 6.4A, as the acceleration factor increases, the average SNR value of the ROI from the SENSE model decreases, whereas the average SNR values from the other three models increase. Comparing the mSPECS and the two slice-wise image shift techniques, the mSPECS-CAIPIVAT model provides the highest average SNR value of the ROI among these three models. From Figure 6.4B, as the acceleration factor increases, the average g -factor value of the ROI from the SENSE model increases dramatically. On the other hand, similar to the results from the simulation reconstruction study, the average g -factor values of the ROI from the mSPECS, mSPECS-VAT, mSPECS-CAIPIRINHA, and mSPECS-CAIPIVAT models increase slightly, with the mSPECS-CAIPIVAT model providing the lowest average g -factor value among the four models.

6.2.2 Task Experimental Reconstruction Results

We also investigated the activation signal detection of the new proposed slice-wise image shift model by analyzing the CNR value map and the activation detection maps and comparing the reconstructed results with the SENSE and mSPECS model. We compared the average CNR value of the ROI between different models with different acceleration factors. Figure 6.5 shows the CNR value map for odd axial brain slices from the SENSE, mSPECS, mSPECS-VAT, mSPECS-CAIPIRINHA, and mSPECS-CAIPIVAT models with an acceleration factor of $TPA=2$. The average and standard deviation of the CNR values for the ROI are also shown in Figure 6.5. From Fig. 6.5, it is evident that the SENSE model cannot detect any activation blocks in the right motor cortex brain area. In contrast, the other three models, mSPECS, mSPECS-VAT, mSPECS-CAIPIRINHA, and mSPECS-CAIPIVAT can detect clear activation blocks with detailed anatomical structures. When comparing the average CNR values

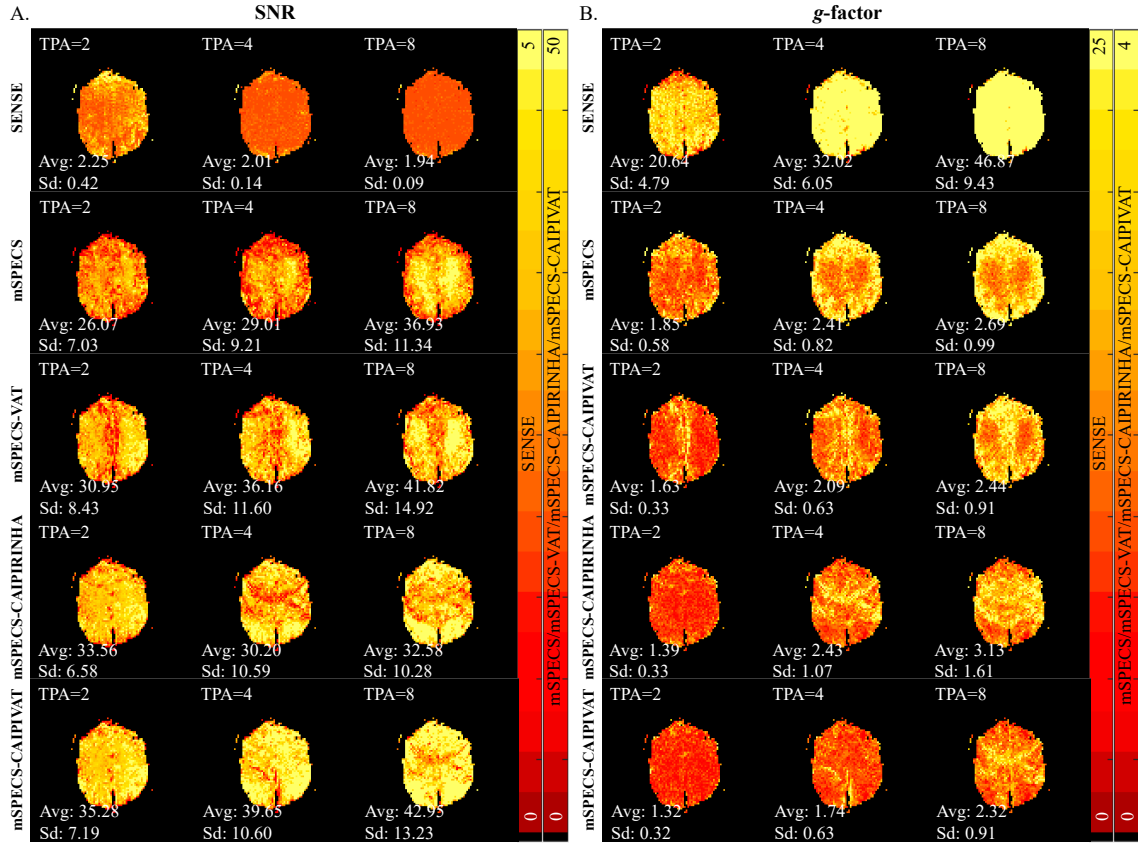


Figure 6.4: A. The SNR maps for SENSE, mSPECS, mSPECS-VAT, mSPECS-CAIPIRINHA and mSPECS-CAIIVAT model with TPA=2, TPA=4, and TPA=8. B. The g -factor maps for SENSE, mSPECS, mSPECS-VAT, mSPECS-CAIPIRINHA and mSPECS-CAIIVAT model with TPA=2, TPA=4, and TPA=8.

of the ROI, the three slice-wise image shift techniques, mSPECS-VAT, mSPECS-CAIPIRINHA and mSPECS-CAIIVAT, have higher values than mSPECS model. Figure 6.6 presents the activation block detection maps from the four models with an acceleration factor of TPA=2. The average and standard deviation of the z-scores for the ROI are also shown in Figure 6.6. Similar to the CNR maps, the SENSE model fails to detect any activation blocks within the brain. The mSPECS, mSPECS-VAT, mSPECS-CAIPIRINHA, and mSPECS-CAIIVAT models capture the activation signals with clear shapes and anatomical structures. The average z-score of the ROI from the two slice-wise image shift techniques is higher than that of the mSPECS model, with the mSPECS-CAIIVAT model providing the highest

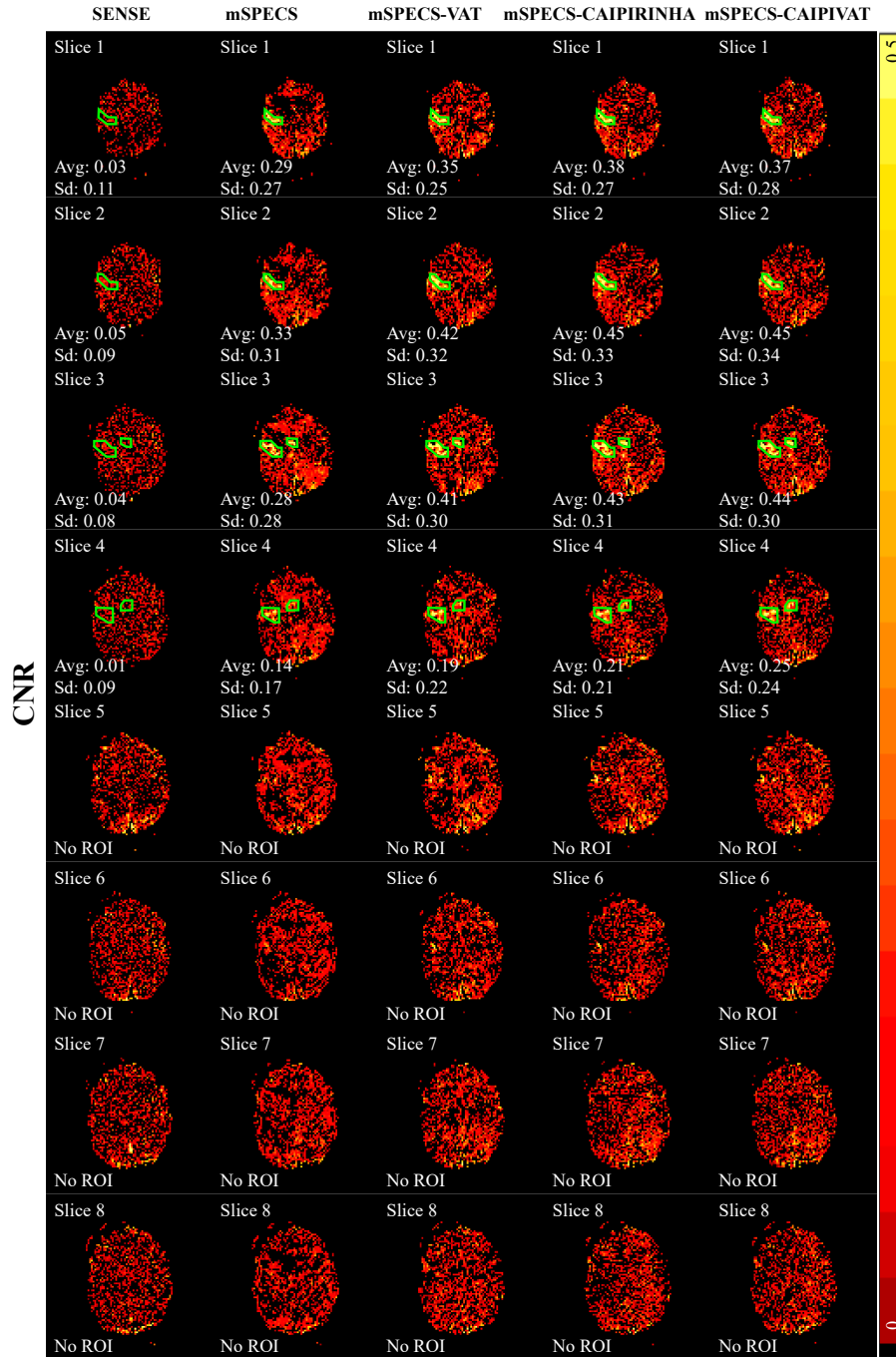


Figure 6.5: The *CNR* map and the average *CNR* value and standard deviation of *CNR* of ROI for SENSE, mSPECS, mSPECS-CAIPIRINHA and mSPECS-CAIPIVAT model with TPA=2.

average z-score for the ROI. A similar conclusion can be drawn from the *CNR* maps and task activation detection maps for even slices of the experimental reconstructed

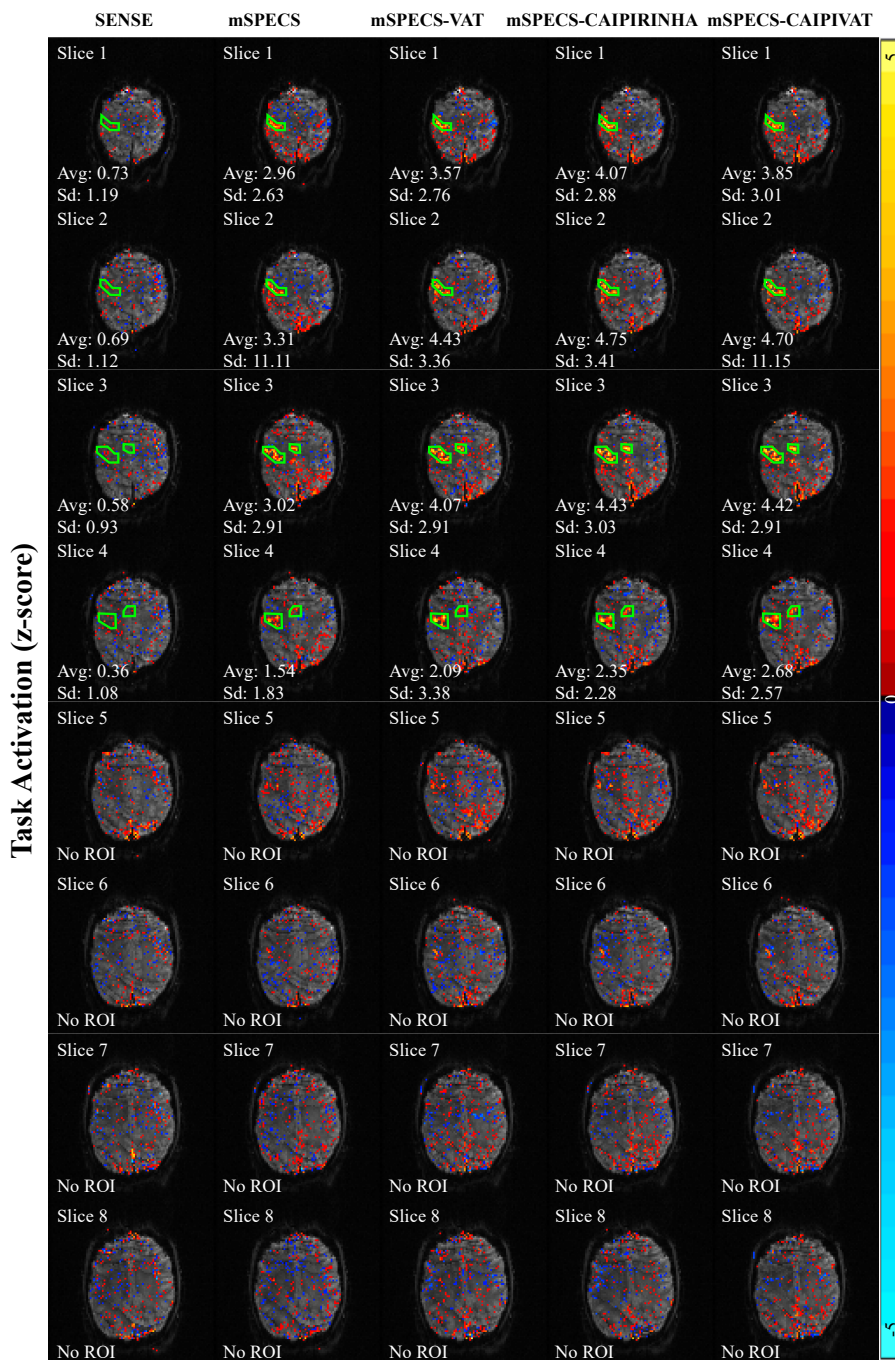


Figure 6.6: The activation detection map and the average and standard deviation of z-score of ROI for SENSE, mSPECS, mSPECS-CAIPIRINHA and mSPECS-CAIPIVAT model with TPA=2.

images.

Figure 6.7A shows the *CNR* map for SENSE, mSPECS, mSPECS-VAT, mSPECS-

CAIPIRINHA, and mSPECS-CAIPIVAT model with TPA=2, TPA=4, and TPA=8. As the acceleration factor increases, the SENSE model cannot capture any activation signals. Furthermore, the average CNR value of the ROI decreases for the mSPECS, mSPECS-VAT, mSPECS-CAIPIRINHA, and mSPECS-CAIPIVAT models as the acceleration factor increases, indicating that as the number of aliasing slices increases, the activation blocks become harder to detect. However, the two slice-wise image-shifting techniques still provide higher average CNR values for the ROI than the mSPECS model, with the mSPECS-CAIPIVAT model providing the highest score. This means that the mSPECS-CAIPIVAT model is more powerful than the other three models in detecting activation blocks. The activation detection maps were also investigated. Figure 6.7B shows the activation detection map and the average z-score of the ROI from four models with different acceleration factors TPA=2, TPA=4, and TPA=8. The SENSE model cannot detect any activation blocks with any acceleration factor. Additionally, as the acceleration factor increases, the average z-score of the ROI decreases for the mSPECS, mSPECS-VAT, mSPECS-CAIPIRINHA, and mSPECS-CAIPIVAT models, indicating that detecting activation blocks becomes more challenging with more aliasing slices. However, when comparing the mSPECS model with the image-shifting techniques, the slice-wise image-shifting models provide higher average z-scores of the ROI, with the mSPECS-CAIPIVAT model having the highest average z-score. Thus, we reach the same conclusion as in the simulation study: the mSPECS-CAIPIVAT model is more powerful in detecting activation signals compared to the other models.

6.3 mSPECS-IPA-CAIPIVAT

6.3.1 Non-Task Experimental Reconstruction Results

To investigate the performance of the proposed novel image-shifted SMS techniques in a real-world fMRI experiment, we applied four models to an *in vivo* right-

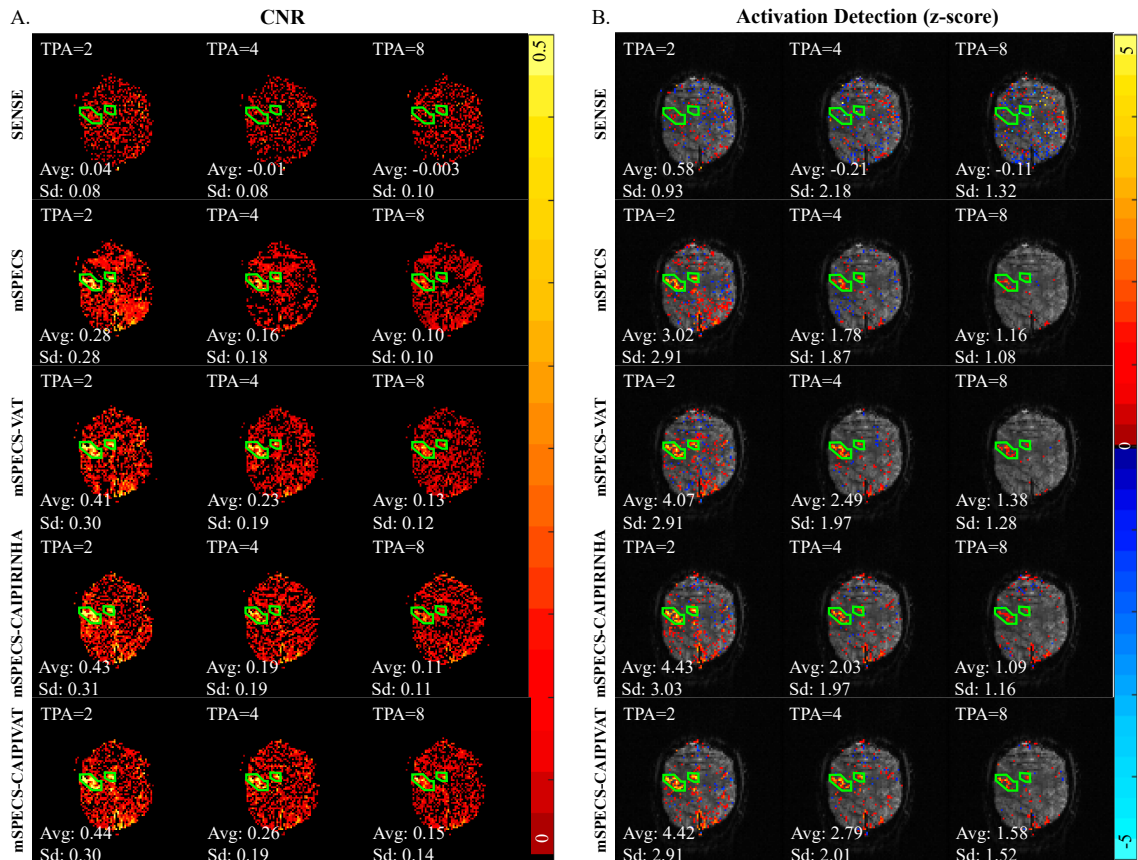


Figure 6.7: A. The *CNR* maps and average ROI *CNR* value from SENSE, mSPECS, mSPECS-VAT, mSPECS-CAIPIRINHA and mSPECS-CAIPIVAT model with respect to different acceleration factors TPA=2, TPA=4, and TPA=8 for slice 3. B. The task activation detection maps and the average ROI z-score from SENSE, mSPECS, mSPECS-VAT, mSPECS-CAIPIRINHA and mSPECS-CAIPIVAT model with respect to acceleration factor TPA=2, TPA=4 and TPA=8 for slice 3. The higher *CNR* and z-score, the better model performs.

handed finger-tapping fMRI time series. The reconstruction results from these models were compared with reference axial brain images, reconstructed using the SENSE technique from the calibration axial brain image time series. Additionally, we applied the novel image-shifted SMS techniques with the same in-plane acceleration factor, IPA = 2, and varying through-plane acceleration factors, TPA = 2, TPA = 4, and TPA = 8, to examine the impact of acceleration on each model. Figure 6.8 and Figure 6.9 show the mean magnitude and mean phase of the reconstructed with TPA = 2 from the mSPECS-IPA, mSPECS-IPA-CAIPIRINHA, mSPECS-IPA-VAT,

and mSPECS-IPA-CAIPIVAT models, compared to the mean magnitude and mean phase of the reference image from the calibration images. Compared to the mean magnitude of the reference image, the mean magnitude from the four image-shifted SMS models is closely aligned with the reference image. No inter-slice signal leakage or artifactual brain distortions from other slices were observed in the reconstructed images. Compared to the mean phase of the reference image, the mean phase of the reconstructed images from the mSPECS-IPA, mSPECS-IPA-CAIPIRINHA, mSPECS-IPA-VAT, and mSPECS-IPA-CAIPIVAT models exhibits a highly similar pattern inside the brain. However, residual artifacts appear outside the brain, particularly in the mSPECS-IPA-CAIPIRINHA and mSPECS-IPA-CAIPIVAT models, which can be attributed to voxel aliasing, slice overlapping, and image shift techniques applied in different models.

Figure 6.10 shows the temporal variance of the reconstructed image of slice 3 for each model under different acceleration factors. As the acceleration factor increases, the temporal variance increases significantly in the mSPECS-IPA-CAIPIRINHA model. The temporal variance in the mSPECS-IPA-CAIPIVAT model also increases, particularly in the central region of the brain, as the acceleration factor increases. However, in the two models without vertical image shift techniques, mSPECS-IPA and mSPECS-IPA-VAT, the temporal variance decreases. Moreover, in a comparison between these two models, the mSPECS-IPA-VAT model exhibits lower temporal variance in the left and right motor cortex regions of the brain as the acceleration factor increases.

Similar to the simulation-based reconstructed axial brain image analysis, we also investigate the signal-to-noise ratio (SNR) and the geometric factor (g -factor) in the reconstructed brain images from the mSPECS-IPA, mSPECS-IPA-CAIPIRINHA, mSPECS-IPA-VAT, and mSPECS-IPA-CAIPIVAT models under different acceleration factors. The SNR value and the g -factor are calculated as described in Chap-

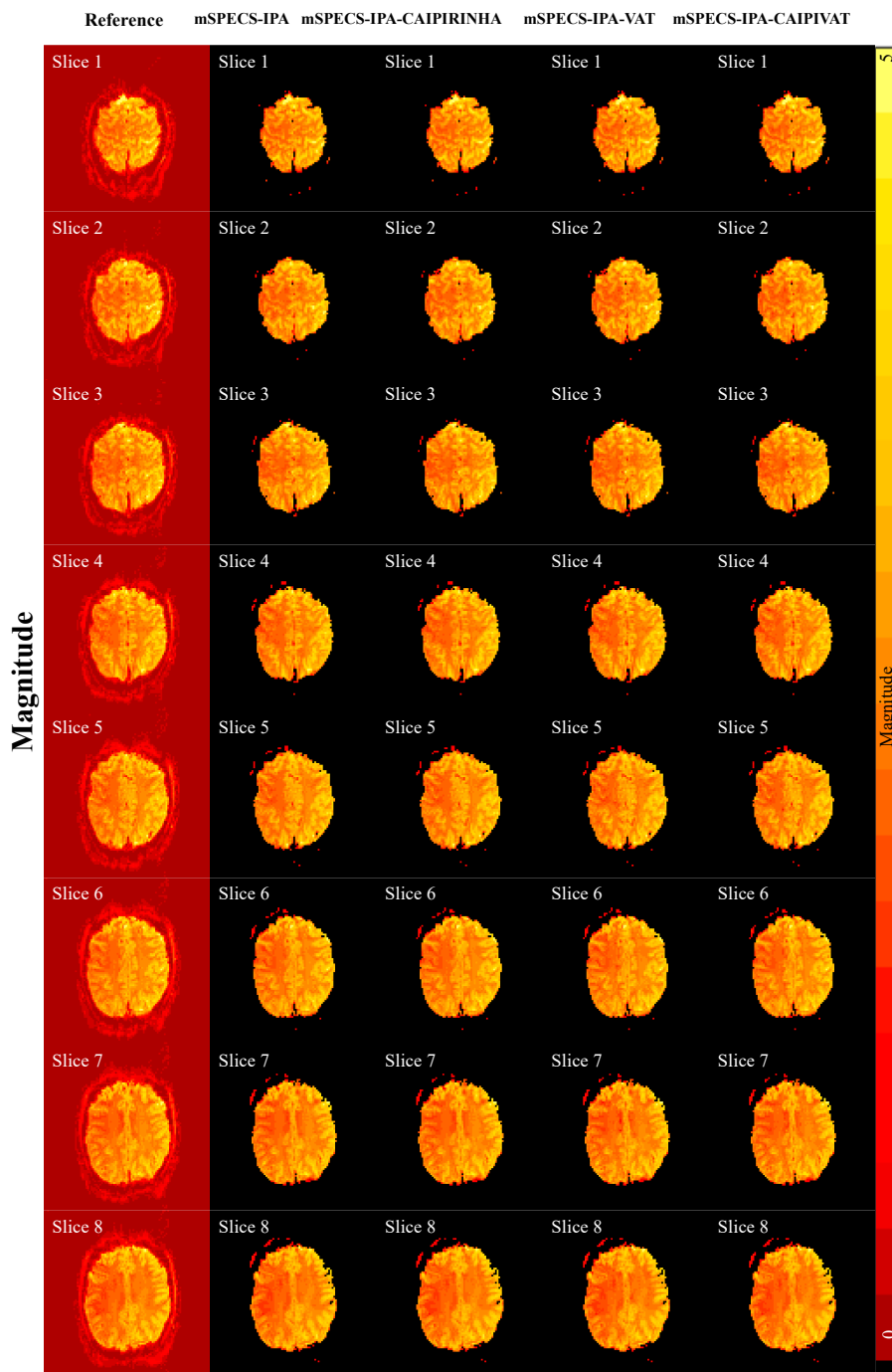


Figure 6.8: The mean magnitude from reconstructed image with through-plane acceleration factor $TPA=2$ corresponding to mSPECS-IPA, mSPECS-IPA-CAIPIRINHA, mSPECS-IPA-VAT and mSPECS-IPA-CAIPIVAT model.

ter 5.3.1. Figure 6.11A shows the average SNR value for slice 3 in the mSPECS-IPA, mSPECS-IPA-CAIPIRINHA, mSPECS-IPA-VAT, and mSPECS-IPA-CAIPIVAT mod-

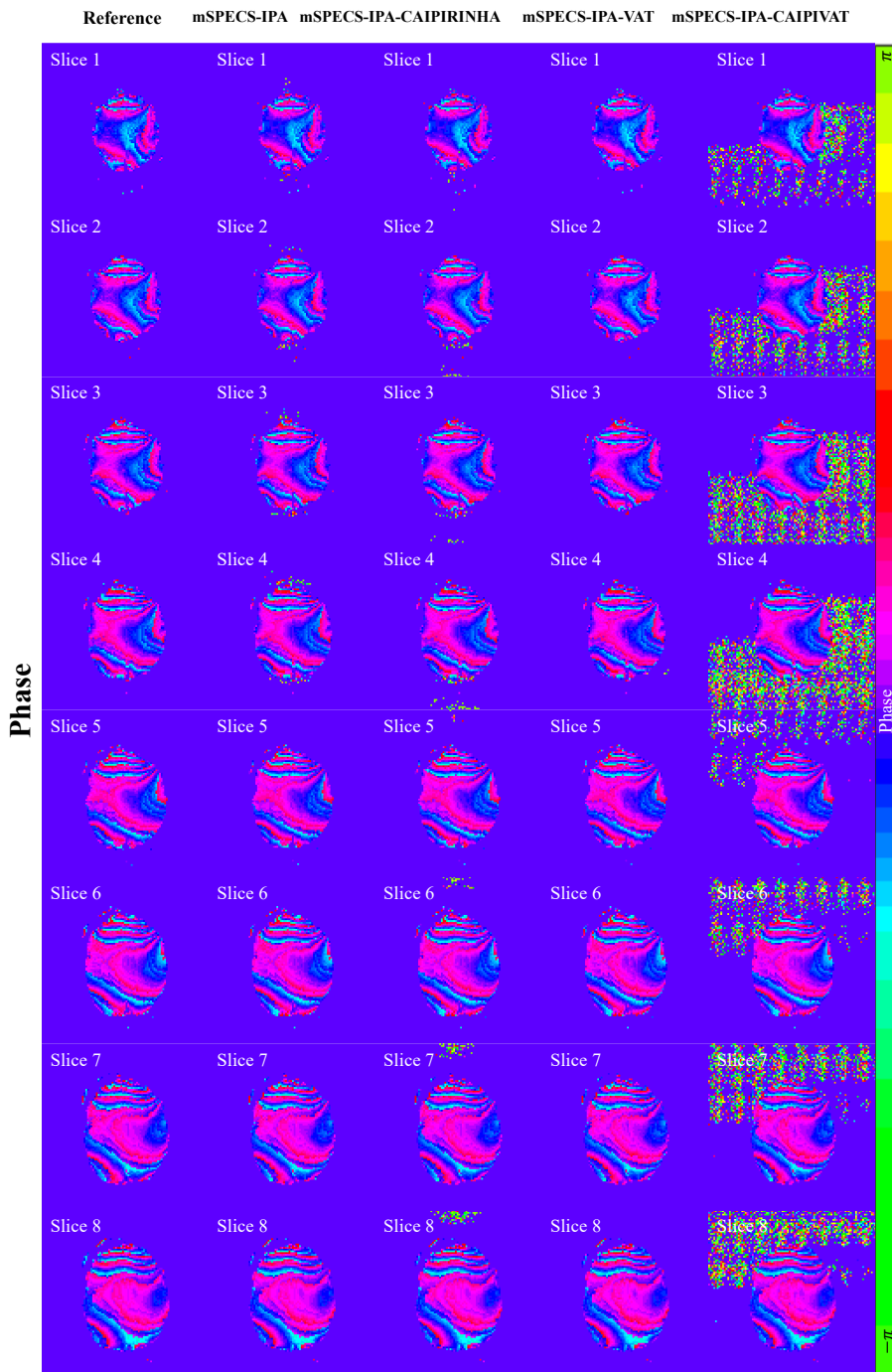


Figure 6.9: The mean phase from reconstructed image with through-plane acceleration factor $TPA=2$ corresponding to mSPECS-IPA, mSPECS-IPA-CAIPIRINHA, mSPECS-IPA-VAT and mSPECS-IPA-CAIPIVAT model.

els with acceleration factors $TPA = 2$, $TPA = 4$, and $TPA = 8$. As the acceleration factor increases, the average SNR in the mSPECS-IPA and mSPECS-IPA-VAT mod-

Variance of Task Signal

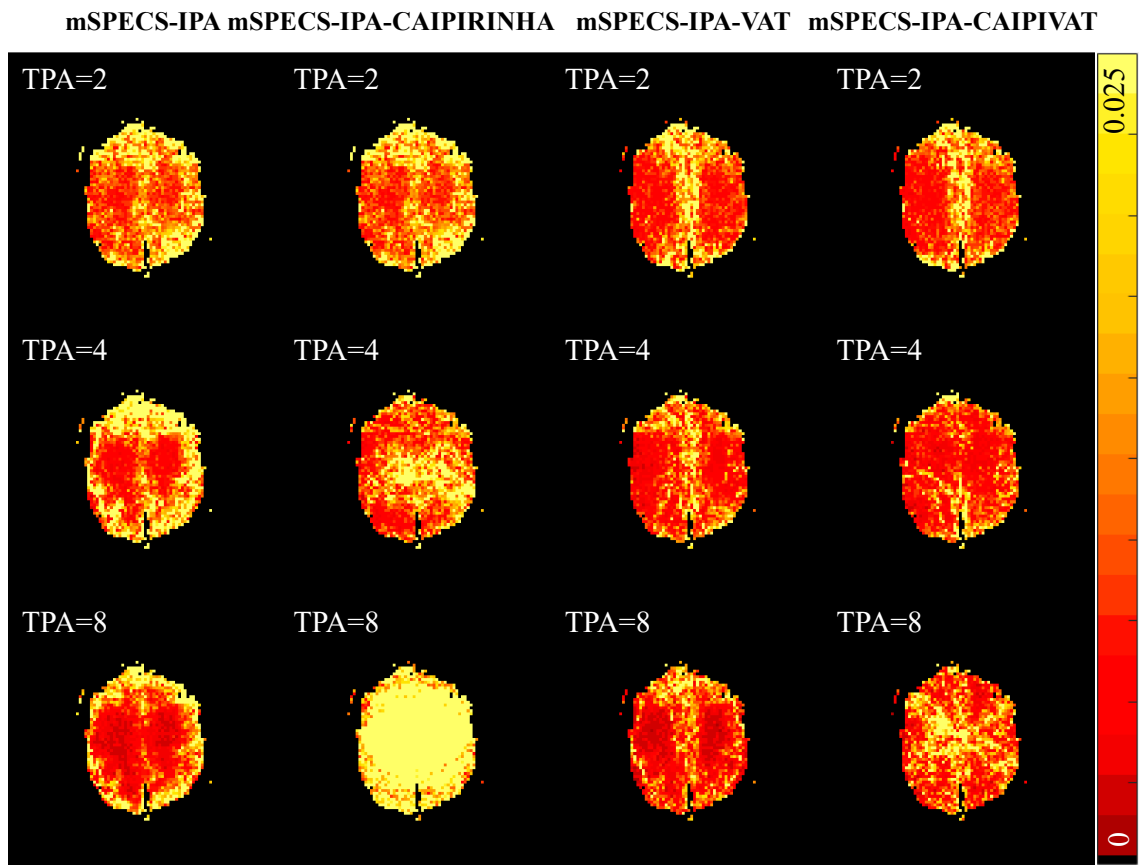


Figure 6.10: The temporal variance of reconstructed image for slice 3 from mSPECS-IPA, mSPECS-IPA-CAIPIRINHA, mSPECS-IPA-VAT and mSPECS-IPA-CAIPIVAT model with different acceleration factor TPA=2, TPA=4, and TPA=8.

els also increases. The mSPECS-IPA-VAT model exhibits a higher average SNR at the edges of the brain image compared to the mSPECS-IPA model. Conversely, in the models incorporating vertical image shift (mSPECS-IPA-CAIPIRINHA and mSPECS-IPA-CAIPIVAT), the average SNR initially increases as the acceleration factor increases from TPA = 2 to TPA = 4 but decreases at TPA = 8. Comparing the average SNR of the reconstructed axial brain images across the four models, the mSPECS-IPA-VAT model provides the highest SNR value. Figure 6.11B shows the g -factor of the reconstructed image of slice 3 for the mSPECS-IPA, mSPECS-IPA-CAIPIRINHA, mSPECS-IPA-VAT, and mSPECS-IPA-CAIPIVAT models un-

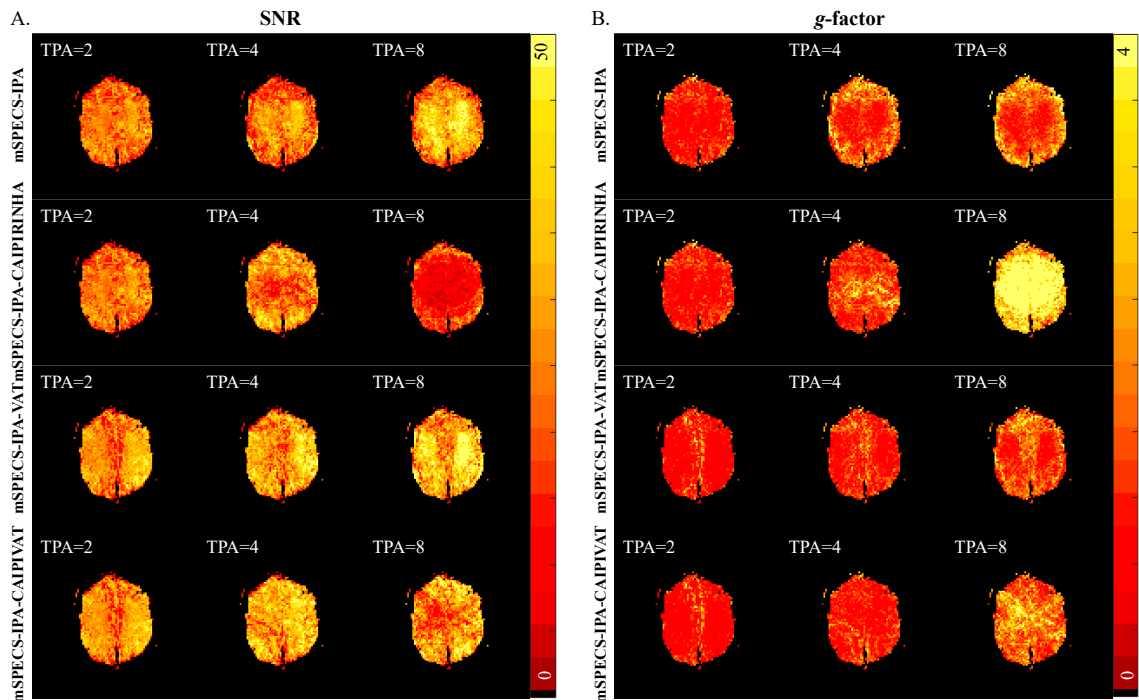


Figure 6.11: A. The SNR value of reconstructed brain images slice 3 from mSPECS-IPA, mSPECS-IPA-CAIPIRINHA, mSPECS-IPA-VAT and mSPECS-IPA-CAIPIVAT model with different acceleration factors. B. The g -factor value of reconstructed brain images slice 3 from mSPECS-IPA, mSPECS-IPA-CAIPIRINHA, mSPECS-IPA-VAT and mSPECS-IPA-CAIPIVAT model with different acceleration factors.

der different acceleration factors. Although the g -factor increases across all four models as the acceleration factor increases, the mSPECS-IPA-VAT model exhibits the lowest g -factor compared to the other three models. In contrast, the mSPECS-IPA-CAIPIRINHA model has the highest g -factor among the four models at TPA = 8.

6.3.2 Task Experimental Reconstruction Results

To analyze the activation detection ability of the proposed image-shifted SMS technique in a real-world right-handed finger-tapping fMRI experiment, we also investigate the contrast-to-noise ratio (CNR) and the activation detection rate (z -score) of ROI of the reconstructed axial brain images from the mSPECS-IPA, mSPECS-IPA-

CAIPIRINHA, mSPECS-IPA-VAT, and mSPECS-IPA-CAIPIVAT models under different acceleration factors. Since the right-handed finger-tapping fMRI experiment was conducted, the task activation area was expected to be in the left motor cortex of the brain. Figure 6.12 shows the average *CNR* value in the ROI for odd slices of the reconstructed images from the mSPECS-IPA, mSPECS-IPA-CAIPIRINHA, mSPECS-IPA-VAT, and mSPECS-IPA-CAIPIVAT models with an acceleration factor of $TPA = 2$. Compared to models without horizontal image shift, mSPECS-IPA and mSPECS-IPA-CAIPIRINHA, models incorporating horizontal image shift, mSPECS-IPA-VAT and mSPECS-IPA-CAIPIVAT, exhibit a higher average *CNR* value in the ROI, with mSPECS-IPA-VAT achieving the highest *CNR* value among the four models. Figure 6.13 shows the task activation detection rate for odd slices of the reconstructed images from the mSPECS-IPA, mSPECS-IPA-CAIPIRINHA, mSPECS-IPA-VAT, and mSPECS-IPA-CAIPIVAT models with $TPA = 2$. Similar to the conclusion drawn from the average *CNR* in the ROI, the mSPECS-IPA-VAT and mSPECS-IPA-CAIPIVAT models exhibit a higher average z-score in the ROI of the left motor cortex compared to the mSPECS-IPA and mSPECS-IPA-CAIPIRINHA models. Among these four models, the mSPECS-IPA-VAT model provides the best activation detection map at $TPA = 2$, indicating that mSPECS-IPA-VAT is the most sensitive model for detecting task activation blocks.

The average *CNR* value in the ROI and the task activation detection rate were also analyzed for the mSPECS-IPA, mSPECS-IPA-CAIPIRINHA, mSPECS-IPA-VAT, and mSPECS-IPA-CAIPIVAT models under different acceleration factors. Figure 6.14A shows the average *CNR* value in the ROI of slice 3 for the four models, compared at different acceleration factors, $TPA = 2$, $TPA = 4$, and $TPA = 8$. As the acceleration factor increases, the average *CNR* decreases significantly across all four models. However, among them, the mSPECS-IPA-VAT model provides the highest average *CNR* in the ROI, while the mSPECS-IPA-CAIPIRINHA model exhibits the

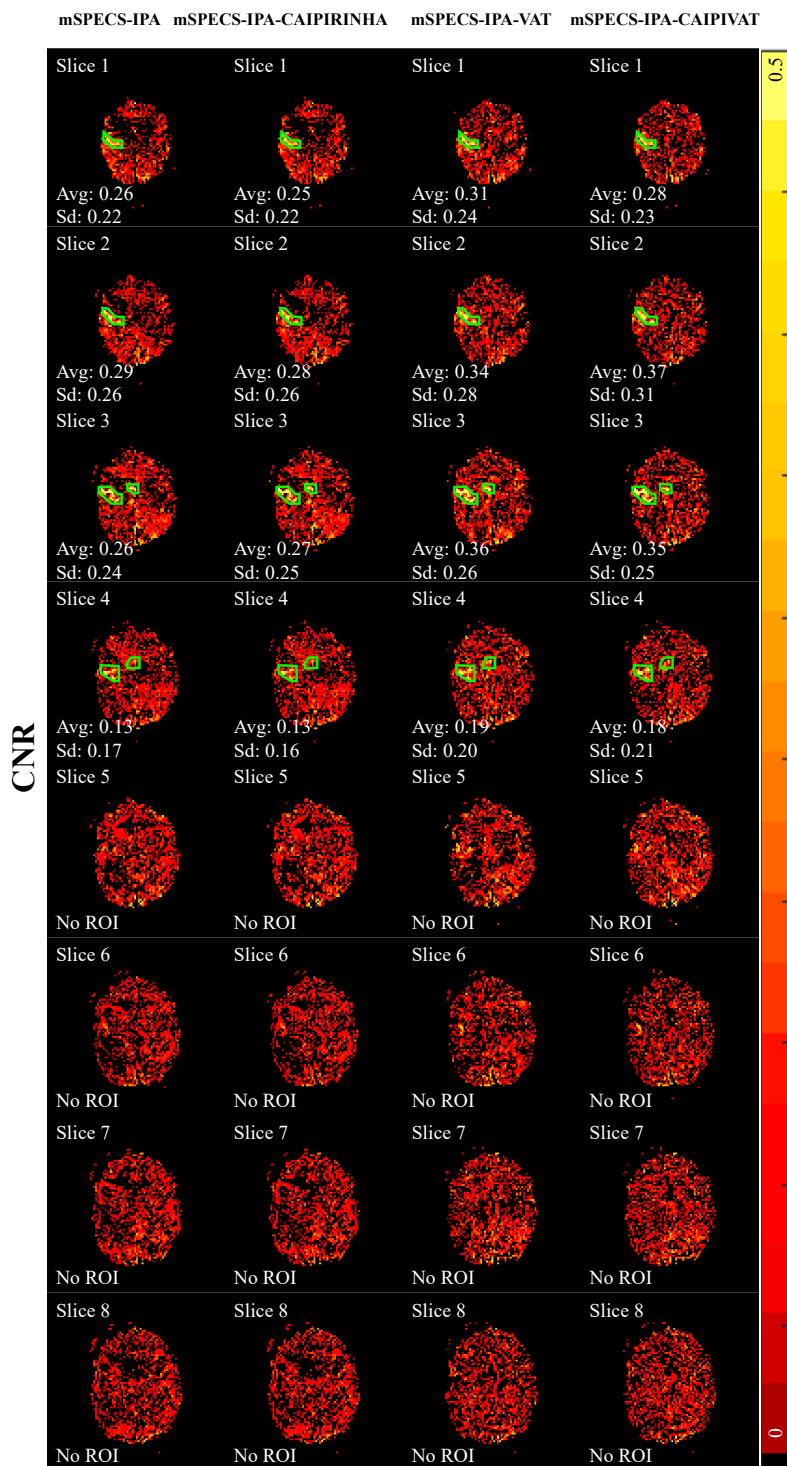


Figure 6.12: The average *CNR* value of ROI for odd slices of reconstructed images from mSPECS-IPA, mSPECS-IPA-CAIPIRINHA, mSPECS-IPA-VAT and mSPECS-IPA-CAPIVAT model with TPA=2.

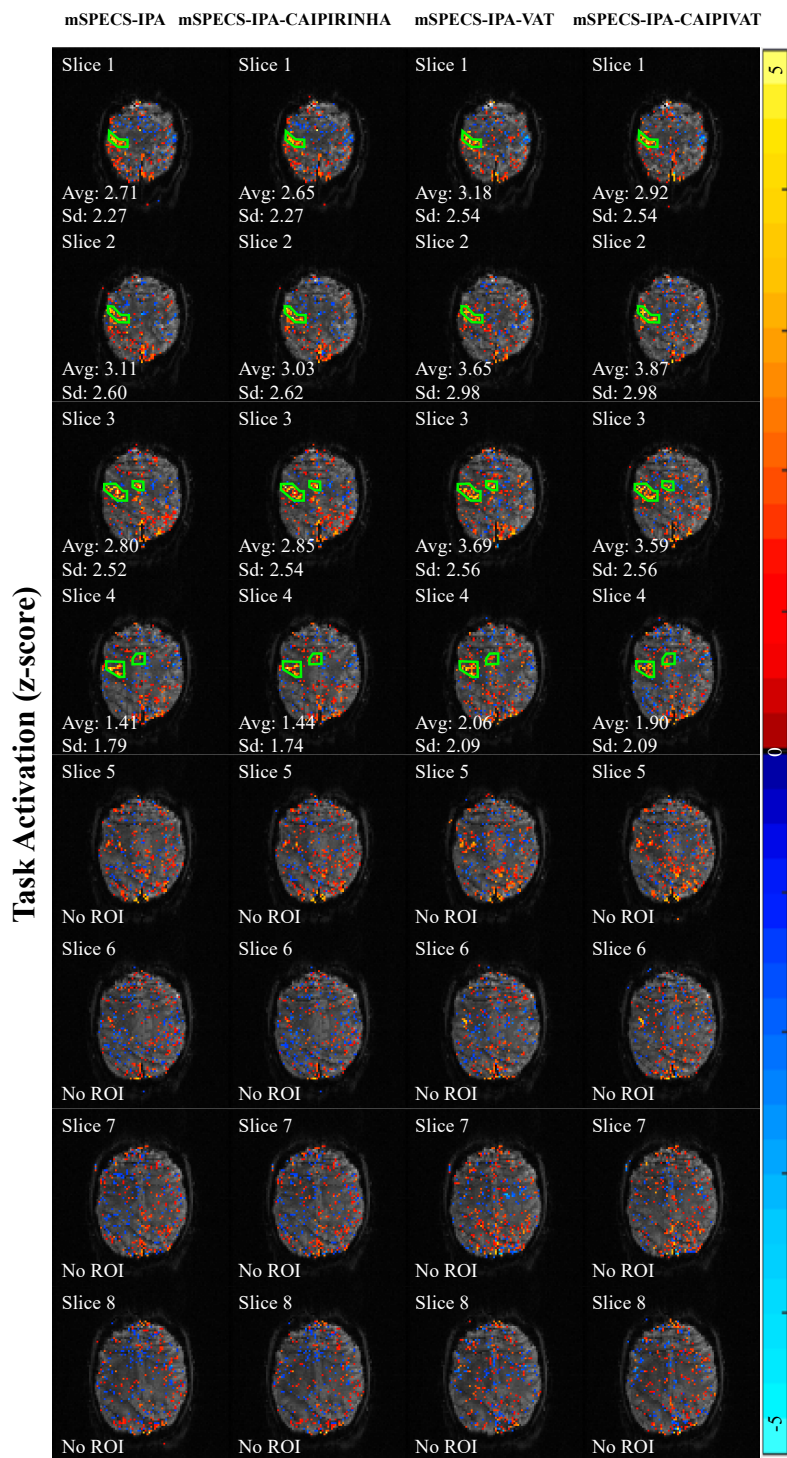


Figure 6.13: The task activation detection (z-score) map of ROI for odd slices of reconstructed images from mSPECS-IPA, mSPECS-IPA-CAIPIRINHA, mSPECS-IPA-VAT and mSPECS-IPA-CAIPIVAT model with TPA=2.

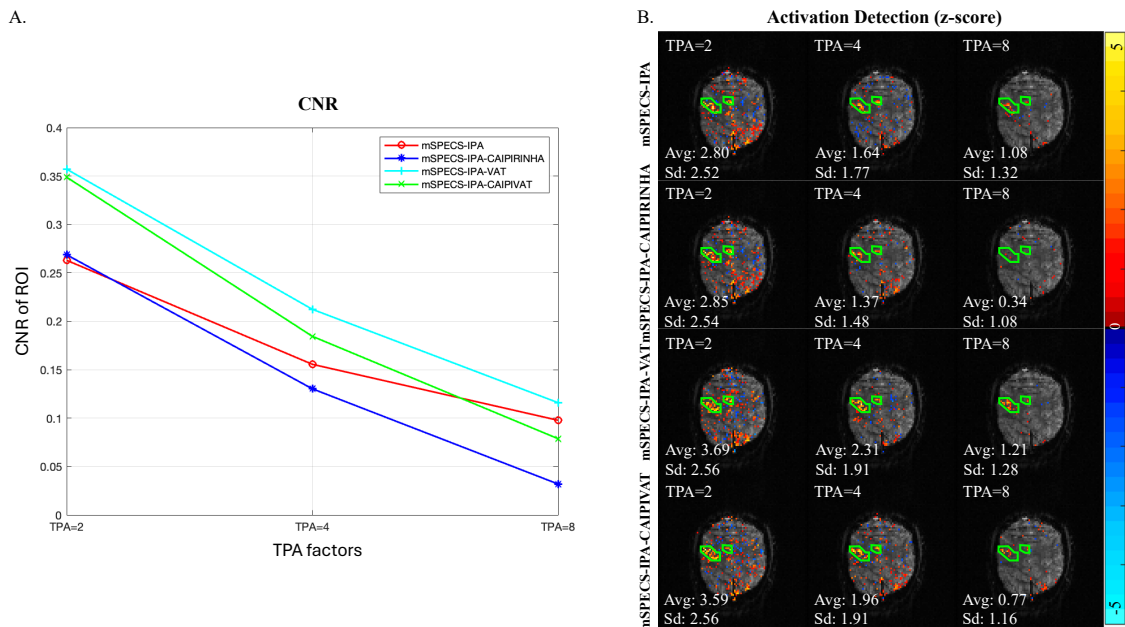


Figure 6.14: A. The average *CNR* value of ROI for slice 3 from mSPECS-IPA, mSPECS-IPA-CAIPIRINHA, mSPECS-IPA-VAT, and mSPECS-IPA-CAIPIVAT model with acceleration factor TPA=2, TPA=4, and TPA=8. B. The average activation detection rate (z-score) of ROI for slice 3 from mSPECS-IPA, mSPECS-IPA-CAIPIRINHA, mSPECS-IPA-VAT, and mSPECS-IPA-CAIPIVAT model with acceleration factor TPA=2, TPA=4, and TPA=8.

lowest average *CNR*. Moreover, models incorporating horizontal image shift exhibit a higher average *CNR* in the ROI compared to models without horizontal image shift. Figure 6.14B shows the average task activation detection map for the ROI of slice 3 across the four models with different acceleration factors. As the acceleration factor increases, the average z-score in the ROI decreases significantly for each model. Among these four models, the mSPECS-IPA-VAT model provides the highest average z-score in the ROI, while the mSPECS-IPA-CAIPIRINHA model exhibits the lowest. Additionally, models incorporating vertical image shift exhibit a lower average z-score compared to models without vertical image shift. The mSPECS-IPA-VAT model demonstrates the strongest ability to detect task activation blocks in brain images.

6.4 GRAPPA Approach for mSPECS-IPA-CAIPIVAT

6.4.1 Non-Task Experimental Reconstruction Results

We investigated the performance of the proposed GRAPPA approach novel image-shifted SMS techniques in a real-world fMRI experiment, hence, similar to the previous chapters, we also applied four models to an *in vivo* right-handed finger-tapping fMRI time series. The reconstruction results from these models were compared with reference axial brain images, reconstructed using the SENSE technique from the calibration axial brain image time series. Additionally, we applied the novel image-shifted SMS techniques with the same in-plane acceleration factor, $IPA = 2$, and varying through-plane acceleration factors, $TPA = 2$, $TPA = 4$, and $TPA = 8$, to examine the impact of acceleration on each model. Figure 6.15 and Figure 6.16 show the mean magnitude and mean phase of the reconstructed with $TPA = 2$ from the GRAPPA for mSPECS-IPA, GRAPPA for mSPECS-IPA-CAIPIRINHA, GRAPPA for mSPECS-IPA-VAT, and GRAPPA for mSPECS-IPA-CAIPIVAT models, compared to the mean magnitude and mean phase of the reference image from the calibration images. Compared to the mean magnitude of the reference image, the mean magnitude from the four GRAPPA applied image-shifted SMS models is closely aligned with the reference image. No inter-slice signal leakage or artifactual brain distortions from other slices were observed in the reconstructed images. Compared to the mean phase of the reference image, the mean phase of the reconstructed images from the GRAPPA for mSPECS-IPA, GRAPPA for mSPECS-IPA-CAIPIRINHA, GRAPPA for mSPECS-IPA-VAT, and GRAPPA for mSPECS-IPA-CAIPIVAT models exhibits a highly similar pattern inside the brain. Moreover, when comparing with the mean phase of the reconstructed images from Figure 6.9, the residual artifacts are significantly eliminated outside the brain, particularly in the GRAPPA for mSPECS-IPA-CAIPIRINHA and GRAPPA for mSPECS-IPA-CAIPIVAT models.

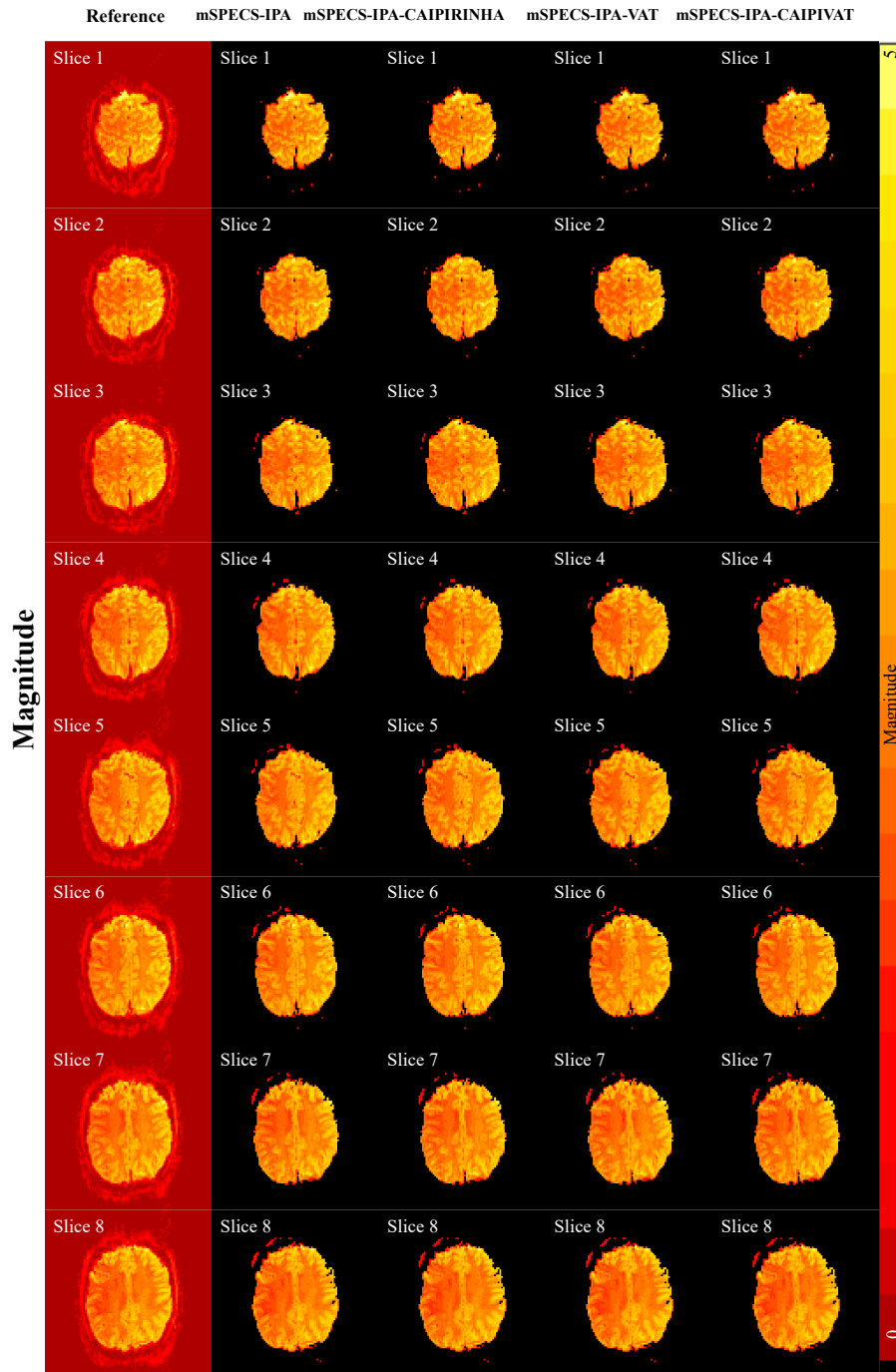


Figure 6.15: The mean magnitude from reconstructed image with in-plane acceleration factor $IPA = 2$ through-plane acceleration factor $TPA = 2$ corresponding to GRAPPA for mSPECS-IPA, GRAPPA for mSPECS-IPA-CAIPIRINHA, GRAPPA for mSPECS-IPA-VAT and GRAPPA for mSPECS-IPA-CAIPIVAT model.

Figure 6.17 shows the temporal variance of the task signal from the reconstructed image of slice 3 for each model under an in-plane acceleration factor of $IPA = 2$

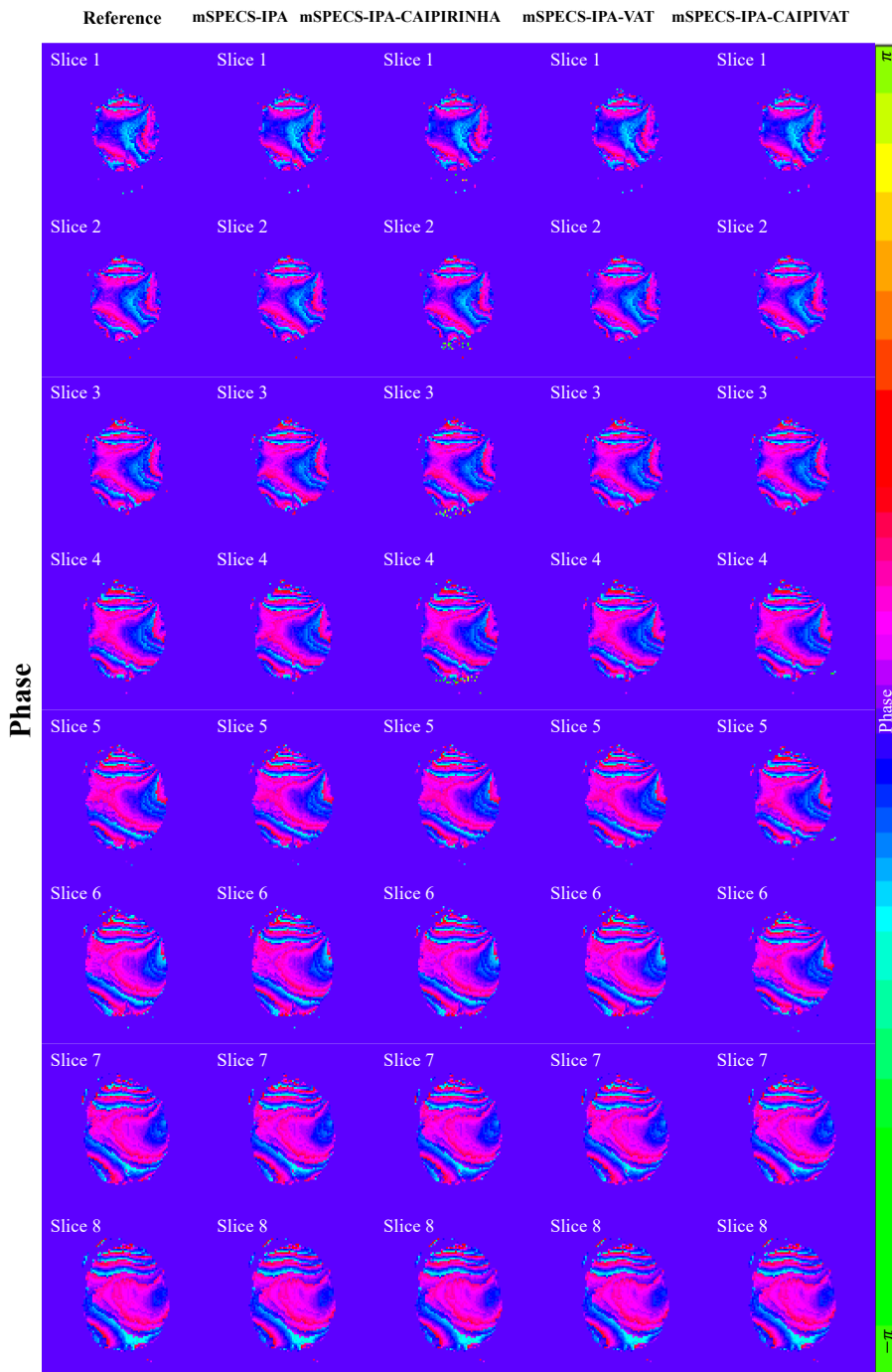


Figure 6.16: The mean phase from reconstructed image with in-plane acceleration factor $IPA = 2$ through-plane acceleration factor $TPA = 2$ corresponding to GRAPPA for mSPECS-IPA, GRAPPA for mSPECS-IPA-CAIPIRINHA, GRAPPA for mSPECS-IPA-VAT and GRAPPA for mSPECS-IPA-CAIPIVAT model.

and different through-plane acceleration factors. As the acceleration factor increases, the temporal variance of the task signal decreases significantly across all four models.

However, the temporal variance of the task signal at the central region of the reconstructed brain image from the GRAPPA applied mSPECS-IPA-CAIPIRINHA model increases compared to the other three models, despite the overall decreasing trend. In the posterior and anterior regions of the brain, the variance of the task signal from the GRAPPA applied mSPECS-IPA-CAIPIRINHA model decreases as the acceleration factor increases. Among these four models, the mSPECS-IPA-CAIPIVAT model provides the lowest temporal variance of the task signal at high acceleration factors. Furthermore, compared to the temporal variance of the task signal from the mSPECS-IPA, mSPECS-IPA-CAIPIRINHA, mSPECS-IPA-VAT, and mSPECS-IPA-CAIPIVAT models in Figure 6.10, the temporal variance of the task signal from the GRAPPA applied novel SMS image shift techniques decreases significantly.

We also investigate the signal-to-noise ratio (SNR) and the geometric factor (g -factor) in the reconstructed brain images from the GRAPPA for mSPECS-IPA, GRAPPA for mSPECS-IPA-CAIPIRINHA, GRAPPA for mSPECS-IPA-VAT, and GRAPPA for mSPECS-IPA-CAIPIVAT models under different acceleration factors. The SNR value and the g -factor are calculated same as described in Chapter 5.3.1. Figure 6.18A shows the average SNR value for slice 3 in the GRAPPA for mSPECS-IPA, GRAPPA for mSPECS-IPA-CAIPIRINHA, GRAPPA for mSPECS-IPA-VAT, and GRAPPA for mSPECS-IPA-CAIPIVAT models with in-plane acceleration factor $IPA = 2$ and through-plane acceleration factors $TPA = 2$, $TPA = 4$, and $TPA = 8$. As the through-plane acceleration factor increases, the average SNR across the four models also increases significantly. In the posterior and anterior regions of the brain image, the GRAPPA for mSPECS-IPA-CAIPIVAT model exhibits the highest average SNR among these four models. However, in the peripheral regions of the brain, the GRAPPA-applied SMS image shift technique incorporating the vertical image shift technique shows a lower average SNR . Moreover, compared to the average SNR in Figure 6.11A, the average SNR in Figure 6.18A is higher. Figure 6.18B shows the

Variance of Task Signal

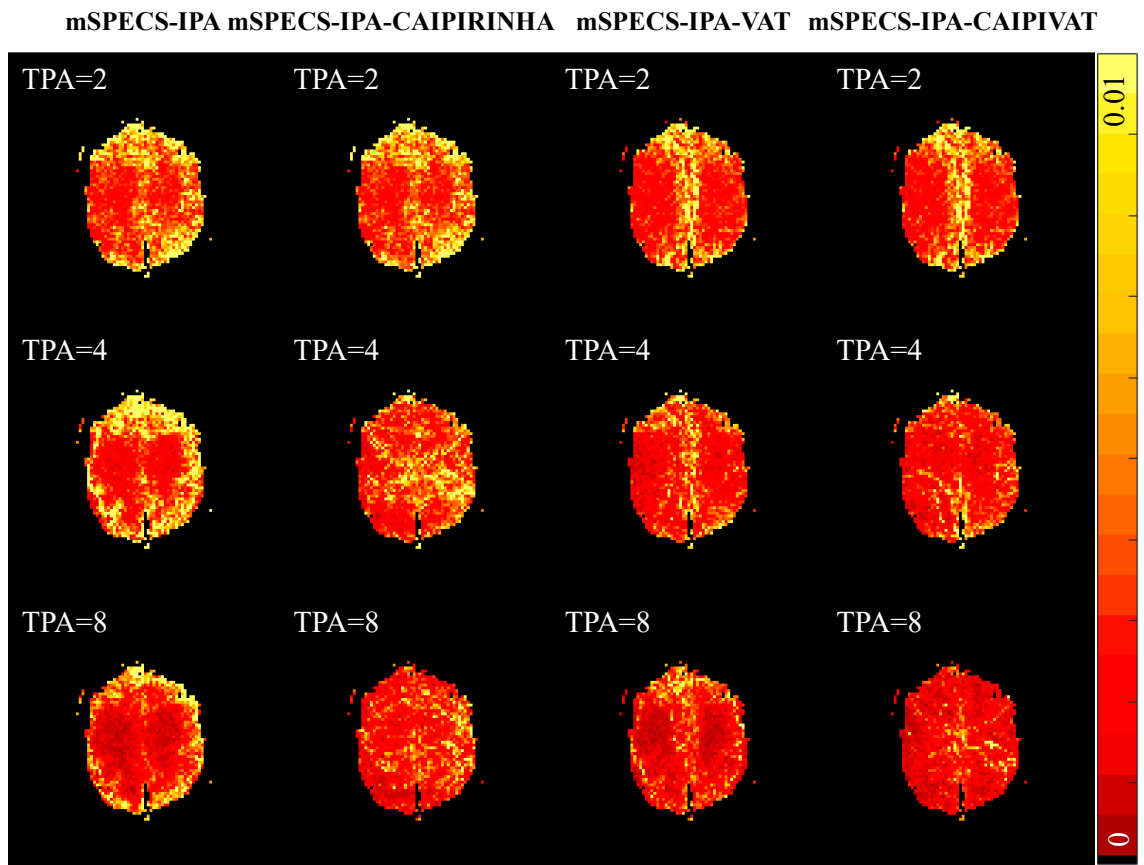


Figure 6.17: The temporal variance of task signal from reconstructed image for slice 3 from GRAPPA for mSPECS-IPA, GRAPPA for mSPECS-IPA-CAIPIRINHA, GRAPPA for mSPECS-IPA-VAT and GRAPPA for mSPECS-IPA-CAIPIVAT model with in-plane acceleration factor $IPA = 2$ different acceleration factor $TPA = 2$, $TPA = 4$, and $TPA = 8$.

g -factor of the reconstructed image of slice 3 for the GRAPPA for mSPECS-IPA, GRAPPA for mSPECS-IPA-CAIPIRINHA, GRAPPA for mSPECS-IPA-VAT, and GRAPPA for mSPECS-IPA-CAIPIVAT models with an in-plane acceleration factor of $IPA = 2$ and different through-plane acceleration factors: $TPA = 2$, $TPA = 4$, and $TPA = 8$. As the through-plane acceleration factor increases, the g -factor of the reconstructed images from all four models also increases. The GRAPPA applied mSPECS-IPA-CAIPIVAT model exhibits a lower g -factor in the posterior and anterior regions of the brain image. However, in the central region of the brain image,

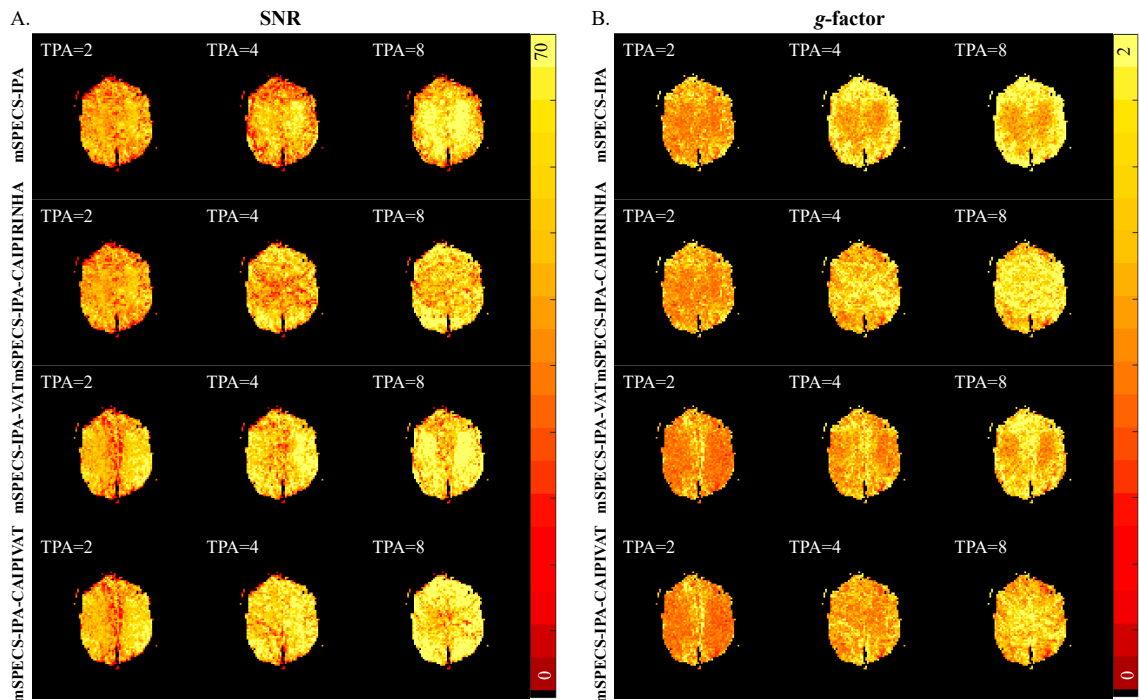


Figure 6.18: A. The SNR value of reconstructed brain images slice 3 from GRAPPA for mSPECS-IPA, GRAPPA for mSPECS-IPA-CAIPIRINHA, GRAPPA for mSPECS-IPA-VAT and GRAPPA for mSPECS-IPA-CAIPIVAT model with in-plane acceleration factor $IPA = 2$ and different through-plane acceleration factors, $TPA = 2$, $TPA = 4$, and $TPA = 8$. B. The g -factor value of reconstructed brain images slice 3 from GRAPPA for mSPECS-IPA, GRAPPA for mSPECS-IPA-CAIPIRINHA, GRAPPA for mSPECS-IPA-VAT and GRAPPA for mSPECS-IPA-CAIPIVAT model with in-plane acceleration factor $IPA = 2$ and different through-plane acceleration factors, $TPA = 2$, $TPA = 4$, and $TPA = 8$.

the g -factor from the GRAPPA applied mSPECS-IPA-CAIPIVAT and mSPECS-IPA-CAIPIRINHA models is higher than that of the other two models. Overall, the g -factor in Figure 6.18B is lower than the g -factor in Figure 6.11B, particularly in models incorporating vertical image shift techniques at high through-plane acceleration factors.

6.4.2 Task Experimental Reconstruction Results

We also investigate the contrast-to-noise ratio (CNR) and the activation detection rate (z-score) of ROI of the reconstructed axial brain images from the GRAPPA for mSPECS-IPA, GRAPPA for mSPECS-IPA-CAIPIRINHA, GRAPPA for mSPECS-

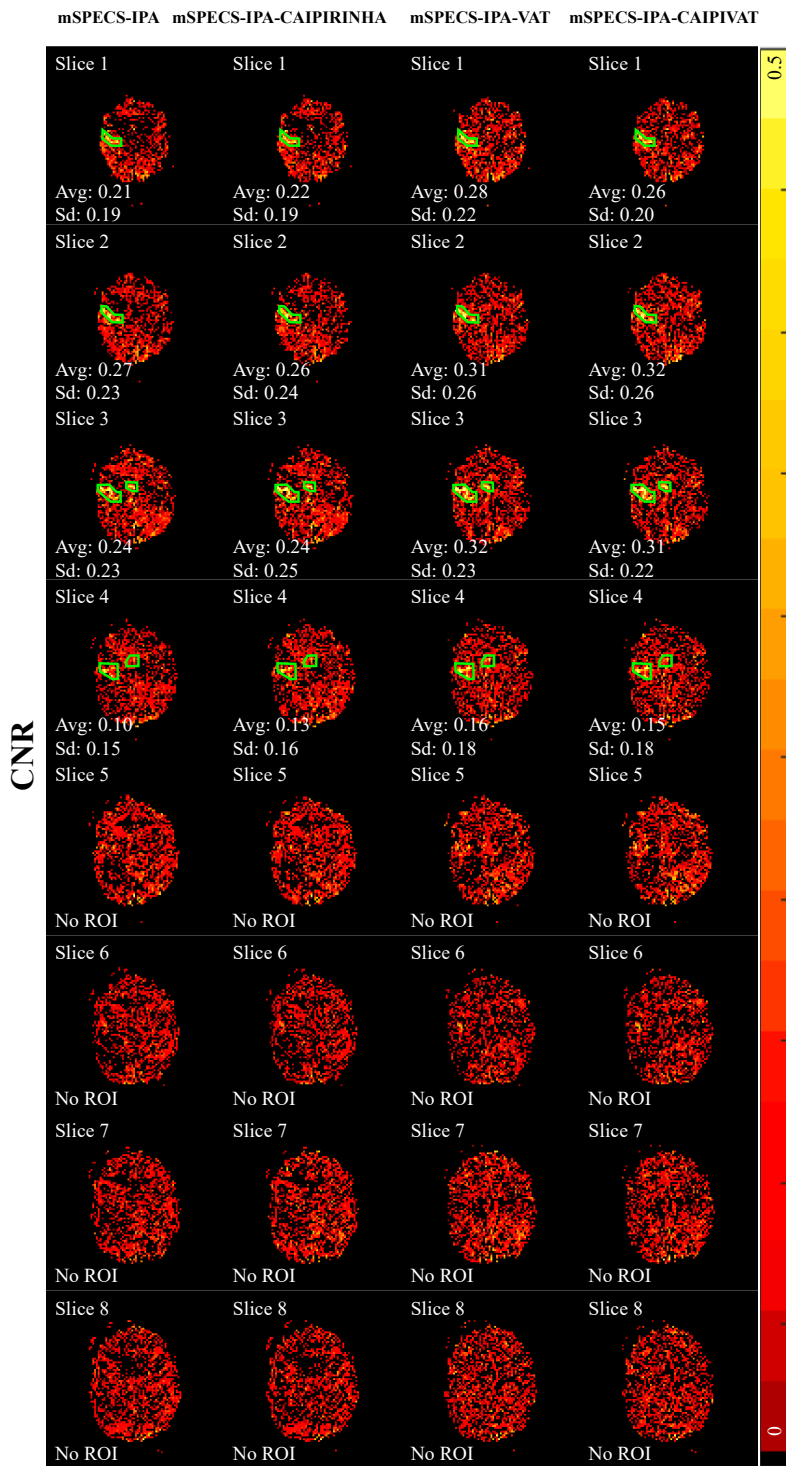


Figure 6.19: The average CNR value of ROI of reconstructed images from GRAPPA for mSPECS-IPA, GRAPPA for mSPECS-IPA-CAIPIRINHA, GRAPPA for mSPECS-IPA-VAT and GRAPPA for mSPECS-IPA-CAIPIVAT model with $IPA = 2$ and $TPA = 2$.

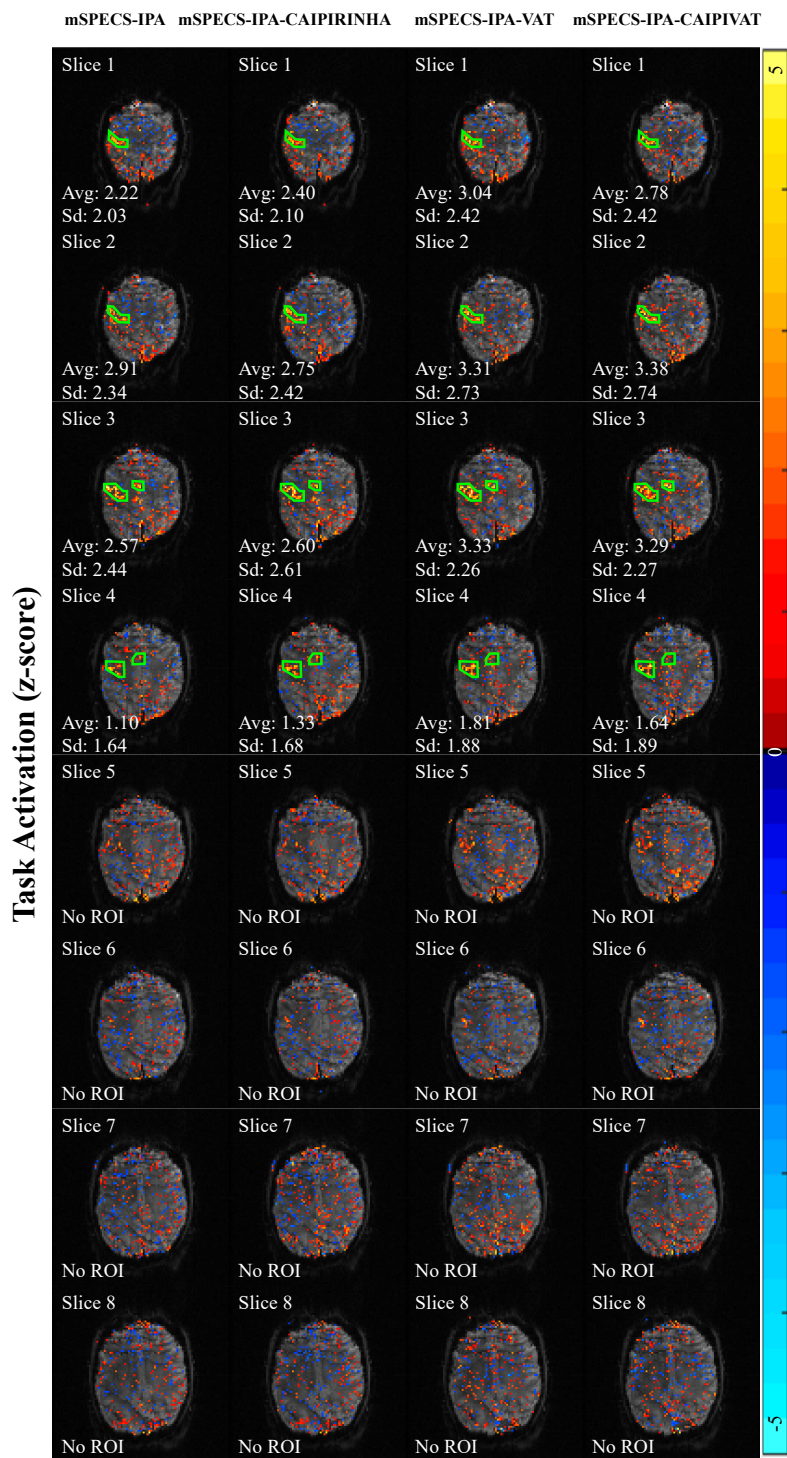


Figure 6.20: The task activation detection (z-score) map of ROI of reconstructed images from the GRAPPA for mSPECS-IPA, GRAPPA for mSPECS-IPA-CAIPIRINHA, GRAPPA for mSPECS-IPA-VAT, and GRAPPA for mSPECS-IPA-CAIPIVAT models with $IPA = 2$ and $TPA = 2$.

IPA-VAT, and GRAPPA for mSPECS-IPA-CAIPIVAT models with same in-plane acceleration factor and different acceleration factors, in order to analyze the activation detection ability of the proposed image-shifted SMS technique in a real-world right-handed finger-tapping fMRI experiment. Since the right-handed finger-tapping fMRI experiment was conducted, the task activation area was expected to be in the left motor cortex of the brain. Figure 6.19 shows the average *CNR* value in the ROI of the reconstructed images from GRAPPA for mSPECS-IPA, GRAPPA for mSPECS-IPA-CAIPIRINHA, GRAPPA for mSPECS-IPA-VAT and GRAPPA for mSPECS-IPA-CAIPIVAT model with $IPA = 2$ and $TPA = 2$. Compared to models without horizontal image shift, GRAPPA for mSPECS-IPA and GRAPPA for mSPECS-IPA-CAIPIRINHA, models incorporating horizontal image shift, GRAPPA for mSPECS-IPA-VAT and GRAPPA for mSPECS-IPA-CAIPIVAT, exhibit a higher average *CNR* value in the ROI. However, compared with the average *CNR* value in the ROI from Figure 6.12, the average *CNR* value in the ROI from Figure 6.19 has slightly lower value when through-plane acceleration factor is low. Figure 6.20 shows the task activation detection rate for ROI of the reconstructed images from the GRAPPA for mSPECS-IPA, GRAPPA for mSPECS-IPA-CAIPIRINHA, GRAPPA for mSPECS-IPA-VAT, and GRAPPA for mSPECS-IPA-CAIPIVAT models with $IPA = 2$ and $TPA = 2$. Similar to the conclusion drawn from the average *CNR* in the ROI, the GRAPPA applied mSPECS-IPA-VAT and mSPECS-IPA-CAIPIVAT models exhibit a higher average z-score in the ROI of the left motor cortex compared to the GRAPPA applied mSPECS-IPA and mSPECS-IPA-CAIPIRINHA models. Moreover, consistent with the findings from the average *CNR* values in Figure 6.19, the average z-score value in the ROI from Figure 6.20 is slightly lower than that in Figure 6.13 when the through-plane acceleration factor is low.

We also investigated the average *CNR* value in the ROI and the task activation detection rate and analyzed for the GRAPPA for mSPECS-IPA, GRAPPA for

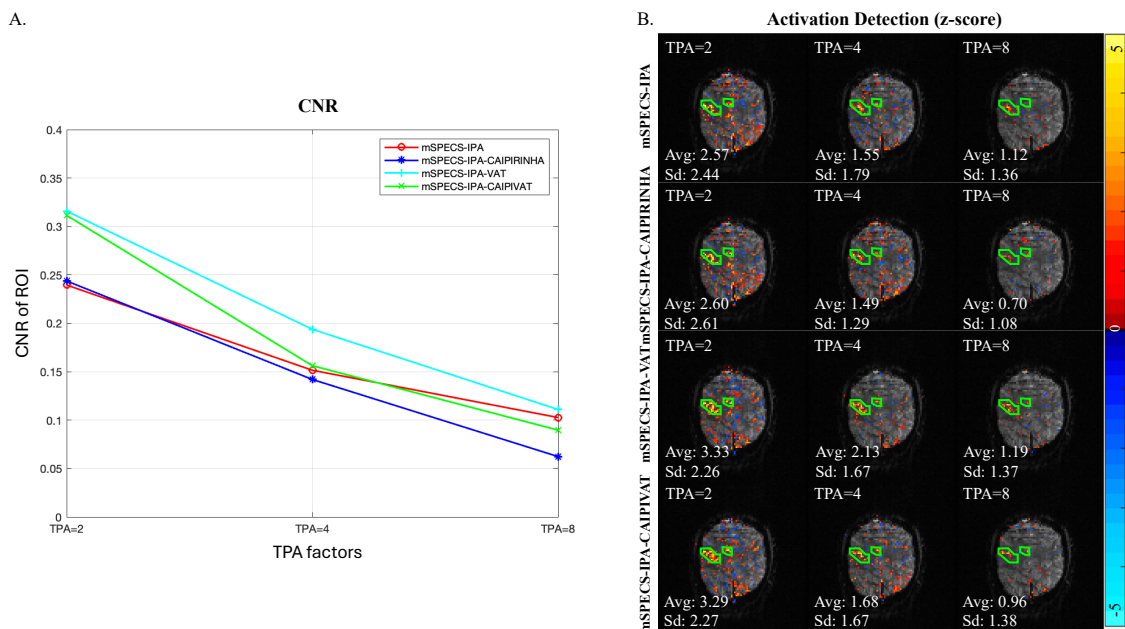


Figure 6.21: A. The average CNR value of ROI for slice 3 from GRAPPA for mSPECS-IPA, GRAPPA for mSPECS-IPA-CAIPIRINHA, GRAPPA for mSPECS-IPA-VAT, and GRAPPA for mSPECS-IPA-CAIPIVAT model with in-plane acceleration factor $IPA = 2$ and through-plane acceleration factor $TPA = 2$, $TPA = 4$, and $TPA = 8$. B. The average activation detection rate (z-score) of ROI for slice 3 from GRAPPA for mSPECS-IPA, GRAPPA for mSPECS-IPA-CAIPIRINHA, GRAPPA for mSPECS-IPA-VAT, and GRAPPA for mSPECS-IPA-CAIPIVAT model with in-plane acceleration factor $IPA = 2$ and through-plane acceleration factor $TPA = 2$, $TPA = 4$, and $TPA = 8$.

mSPECS-IPA-CAIPIRINHA, GRAPPA for mSPECS-IPA-VAT, and GRAPPA for mSPECS-IPA-CAIPIVAT models with same in-plane acceleration factor and different through-plane acceleration factors. Figure 6.21A shows the average CNR value in the ROI of slice 3 for the four models, compared at different acceleration factors, $TPA = 2$, $TPA = 4$, and $TPA = 8$. As the acceleration factor increases, the average CNR decreases significantly across all four models. However, among them, GRAPPA applied mSPECS-IPA-VAT model provides the highest average CNR in the ROI, while the GRAPPA applied mSPECS-IPA-CAIPIRINHA model exhibits the lowest average CNR . Moreover, models incorporating horizontal image shift exhibit a higher average CNR in the ROI compared to models without horizontal image shift. Moreover,

when the through-plane acceleration factor is high, the average *CNR* in the ROI from the GRAPPA-applied SMS image shift model incorporating the vertical image shift technique (Figure 6.21A) is higher than that from the mSPECS-IPA-CAIPIRINHA model in Figure 6.14. Figure 6.21B shows the average task activation detection map for the ROI of slice 3 across the four models with same in-plane acceleration factor and different through-plane acceleration factors. As the acceleration factor increases, the average z-score in the ROI decreases significantly for each model. Among these four models, the GRAPPA applied mSPECS-IPA-VAT model provides the highest average z-score in the ROI, while the GRAPPA applied mSPECS-IPA-CAIPIRINHA model exhibits the lowest with high through-plane acceleration factor. Furthermore, when the through-plane acceleration factor is high, the average z-score in the ROI from the GRAPPA applied SMS image shift model incorporating the vertical image shift technique (Figure 6.21A) is higher than that from the mSPECS-IPA-CAIPIRINHA model in Figure 6.14.

CHAPTER 7: DISCUSSION

7.1 mSPECS-CAIPIVAT

Since fMRI studies were first introduced by Ogawa et al. (1990), efforts have been made to enhance the efficiency of the signal acquisition procedure but still be able to achieve the goal of reconstructing brain images with high resolution, and improve the accuracy to capture the brain activation signal. Parallel imaging reconstruction methods, like SENSE, can be a potential solution to shorten the scan time with a through-plane subsampling technique. However, it is easily influenced by the high similarity of weighted coil sensitivity information of two aliased voxels, which leads to a singular matrix and a inter-slice signal leakage problem in the reconstruction process. In the interest of decreasing the similarity and increasing the independence of the weighted information of aliased voxels, slice-wise imaging shift techniques, CAIPIRINHA and CAIPIVAT, can increase the physical distance of the aliased voxels. Compared to techniques without the image-shifting method, like SENSE and mSPECS, mSPECS-VAT, mSPECS-CAIPIRINHA and mSPECS-CAIPIVAT methods provide reconstructed images with more anatomic details and reduced temporal variance.

We also compared the average SNR values for different tissue types and the average g -factor values of these four models with respect to the different through-plane acceleration factors (Table 2). Moreover, comparing the g -factor penalty among four models with respect to different acceleration factors, the mSPECS-CAIPIVAT model has the lowest value, which means that the mSPECS-CAIPIVAT model has a lower noise amplification level compared with other models. Thus, the image reconstruction method with slice-wise image shift techniques, mSPECS-VAT, mSPECS-CAIPIRINHA and mSPECS-CAIPIVAT, produce better results by increasing the SNR values and de-

creasing the variance of the reconstructed images. However, as shown in Figure 5.12, increasing the through-plane acceleration factor leads to a loss in the average CNR values and the mean activation values of the task block when comparing the mSPECS, mSPECS-VAT, mSPECS-CAIPIRINHA, and mSPECS-CAIPIVAT models. With TPA increasing from 2 to 8, the mSPECS model shows a 63% decrease in CNR and a 62% decrease in mean activation. For the mSPECS-VAT model, CNR decreases by 66% and mean activation by 66%, the mSPECS-CAIPIRINHA model, CNR decreases by 63% and mean activation by 58%, while the mSPECS-CAIPIVAT model shows decreases of 54% for both CNR and mean activation. Thus, when comparing these four models, the SENSE model yields the worst results with strong inter-slice signal leakage. Compared to the mSPECS model, the slice-wise image shift SMS models have higher SNR and CNR values with lower g -factor penalty under the circumstance with high acceleration factors. Similar conclusions can be made from Figure 6.7, compared with the mSPECS model, the slice-wise image shift techniques provide us higher SNR value for the ROI and lower g -factor penalty under the circumstance with high acceleration factor like TPA=8. However, we still need to face the situation where, with the high acceleration factor, the loss of the CNR value and the activation detection rate becomes significant. Therefore, by comparing the average CNR values for the ROI and activation detection maps among the four models, the mSPECS-CAIPIVAT model provides us the best CNR and activation detection map.

In this study, we discussed SMS models employing different slice-wise image shift techniques. Intuitively, the smaller the overlapping area between aliased slices, the easier it is to separate them. Therefore, we compared the completely overlapping case, mSPECS model, with slice-wise image shift techniques, including mSPECS-VAT (horizontal), mSPECS-CAIPIRINHA (vertical), and mSPECS-CAIPIVAT (horizontal and vertical). Compared to slice-wise image shift techniques that operate in only one direction, as in mSPECS-VAT and mSPECS-CAIPIRINHA, the mSPECS-

CAIPIVAT model utilizes shifts in both directions, resulting in a smaller overlapping area and consequently better reconstruction results. By comparing the results from the simulation reconstruction section and the experimental reconstruction section of the mSPECS-VAT, the mSPECS-CAIPIRINHA model and the mSPECS-CAIPIVAT model and to make a fair decision through a trade-off of the increment in the SNR and decrement of the CNR value and the activation detection with respect to different acceleration factors, we suggest the optimal through-plane acceleration factor to be $TPA=4$. Under this circumstance, the mSPECS-CAIPIVAT model can provide reconstructed images with high SNR information, but still be able to capture the activation signal. Our suggestion is consistent with the optimal multiband factor $MB = 4$ from previous work (Risk et al. (2021)).

7.2 mSPECS-IPA-CAIPIVAT

In traditional fMRI image acquisition techniques, images were collected slice-by-slice during the early development of fMRI studies. As imaging techniques advanced, researchers focused on improving the efficiency of the image acquisition process while maintaining the ability to reconstruct high-resolution brain images. Two primary techniques have been developed to achieve this goal: through-plane acceleration and in-plane acceleration. Parallel imaging is one of the through-plane acceleration techniques, allowing multiple brain images to be acquired at each time point in an fMRI time series. Previous studies suggest that an optimal multiband factor for resting-state fMRI is $MB = 4$ (Risk et al. (2021)). A widely used in-plane acceleration technique, GRAPPA, can also reduce scan time by acquiring a subsampled k -space. In this study, through-plane acceleration and in-plane acceleration were combined to further shorten image scan time. However, due to the high similarity of coil sensitivity information in aliased voxels, additional techniques such as 2D Hadamard phase encoding and image shift were incorporated to mitigate the influence of the g -factor.

As discussed in Chapter 3.1.2, the number of aliased brain images should be a power of 2 due to the constraints of the 2D Hadamard coefficient aliasing matrix. However, if an odd number of images are aliased, the orthogonal contrast aliasing matrix design can be incorporated into the model to maintain the orthogonality of the design matrix. In this study, we not only investigated the influence of net acceleration factors and image shift directions on model performance but also assessed the task activation detection ability of each model.

In this study, we first investigated the influence of high acceleration factors on the performance of the mSPECS-IPA, mSPECS-IPA-CAIPIRINHA, mSPECS-IPA-VAT, and mSPECS-IPA-CAIPIVAT models. Based on the simulated reconstructed results in Chapter 5.3 and the experimentally reconstructed results in Chapter 6.3, high acceleration factors had a positive impact on the *SNR* of the reconstructed images in the mSPECS-IPA and mSPECS-IPA-VAT models. As shown in Figure 5.17 and Figure 6.11, as the acceleration factor increased, the average *SNR* also increased. However, in models incorporating vertical image shift, the *SNR* of the reconstructed images decreased as the acceleration factor increased. This effect occurs because image shift in the same direction as the in-plane acceleration results in a more complex slice-overlapping pattern than in models without vertical image shift. A similar conclusion can be drawn from the *g*-factor plot. The *g*-factor penalty in the mSPECS-IPA and mSPECS-IPA-VAT models is more stable compared to the mSPECS-IPA-CAIPIRINHA and mSPECS-IPA-CAIPIVAT models. As shown in Figure 5.25 and Figure 6.14, a high acceleration factor negatively affects the average *CNR* in each model. As the acceleration factor increased, the average *CNR* in the ROI decreased significantly across all models. However, among the four models, the mSPECS-IPA-VAT model exhibited the highest average *CNR* across different acceleration factors. A similar trend was observed in the task activation detection maps for each model under different acceleration factors. As the acceleration factor increased, the average z-score

in the ROI decreased, indicating that capturing task activation signals became more difficult for all models at high acceleration factors. However, the mSPECS-IPA-VAT model maintained the highest average z-score in the ROI, making it the most sensitive model for detecting activation signals compared to the other models. Overall, increasing the acceleration factor has a positive effect on SNR in reconstructed brain images but a negative effect on CNR and activation detection rates. This presents a trade-off in fMRI image acquisition, where a lower acceleration factor is generally more desirable.

We also investigated the influence of the image shift direction on the performance of each model. There are four different directions: mSPECS-IPA has no image shift technique, mSPECS-IPA-CAIPIRINHA has vertical image shift technique, mSPECS-IPA-VAT has horizontal image shift technique and the mSPECS-IPA-CAIPIVAT has vertical and horizontal image shift technique. Comparing the SNR , average CNR plot, and task activation detection maps, models incorporating vertical image shift, mSPECS-IPA-CAIPIRINHA and mSPECS-IPA-CAIPIVAT exhibited worse results in the reconstructed brain images. This is due to the increased voxel aliasing complexity when image shift occurs in the same direction as the in-plane acceleration (i.e., the phase encoding direction). Therefore, to avoid degraded reconstruction performance, it is recommended that image shift be applied in a direction different from the in-plane acceleration direction. Moreover, other factors may also influence the performance of the novel image shift SMS technique, such as the location of the task activation signal and the size of the brain image. For example, if the task activation signal is generated in the posterior or anterior region of the brain, the mSPECS-IPA-VAT model is expected to perform better than the other models. In conclusion, the novel image-shifted SMS technique is recommended to be used with a lower acceleration factor, and the image shift direction should be different from the in-plane acceleration direction to achieve optimal performance.

7.3 The GRAPPA Approach for mSPECS-IPA-CAIPIVAT

In Chapter 4.2, we discussed the motivation for this study: to combine the advantages of the mSPECS-CAIPIVAT model, which does not require careful experimental design, while also benefiting from the mSPECS-IPA-CAIPIVAT model’s reduced image acquisition time. To evaluate the performance of our novel GRAPPA applied SMS image shift model, we first applied models incorporating different image shift directions to simulated fMRI data. Comparing the mean magnitude and mean phase of the reconstructed images across the three studies, all models generated high-resolution reconstructed brain images with detailed anatomical information, and no inter-slice signal leakage was observed. Comparing the variance of the task signal across the three studies, the variance from GRAPPA applied SMS image shift techniques was the lowest (Figure 5.28), whereas the second study exhibited the highest task signal variance (Figure 5.17), particularly in models incorporating vertical image shift techniques. Additionally, when comparing the average SNR and g -factor across the three studies, the GRAPPA-applied SMS image shift techniques exhibited the highest SNR value (Figure 5.29) and the lowest g -factor value. In contrast, the second study had the lowest SNR and the highest g -factor (Figure 5.22), especially in models incorporating vertical image shift techniques. A similar conclusion can be drawn when comparing the reconstructed results from the three studies after applying the models to the real-world right-handed finger tapping experimental fMRI data.

We also investigated the reconstructed results of the three studies by applying them to real-world fMRI time series data from a right-handed finger-tapping experiment. We analyzed the average CNR value in the ROI and the task activation detection (z-score) rate from each study. Similar to the conclusions drawn from the simulated reconstructed results, the reconstructed brain images from all models were high-resolution with detailed anatomical structures. No inter-slice signal leakage was

observed in any of the three models. Comparing the average *CNR* value in the ROI across the three studies, the mSPECS-CAIPIVAT model exhibited the highest average *CNR* value (Figure 6.7), whereas the second study had the lowest average *CNR* value (Figure 5.17), particularly in models incorporating vertical image shift techniques, such as the mSPECS-IPA-CAIPIRINHA and mSPECS-IPA-CAIPIVAT models. Furthermore, when comparing task activation detection across the three studies, the mSPECS-CAIPIVAT model incorporating image shift techniques exhibited the highest task activation detection value (Figure 6.7). In contrast, the second study had the lowest activation detection value (Figure 6.14), particularly when vertical image shift techniques were incorporated into the model.

7.4 Future Work

In this dissertation, we discussed novel SMS multi-directional image shift techniques incorporating in-plane and through-plane acceleration methods and presented them in a Bayesian manner. However, there is still more work to be done in the future to further develop our novel SMS models.

For the first two studies, mSPECS-CAIPIVAT and mSPECS-IPA-CAIPIVAT, we analyzed the reconstructed brain images and investigated the task activation detection ability of each model. However, due to the characteristics of the Hadamard phase encoding technique and the newly proposed 2D Hadamard phase encoding technique, the number of aliased slices per excitation must be a power of 2. If an experiment requires an odd number of aliased slices per excitation, the Hadamard phase encoding technique and the 2D Hadamard phase encoding technique would not be appropriate methods. Instead, an orthogonal contrast experiment design should be considered. Furthermore, to gain a better understanding of brain function, we also need to investigate the correlation between different brain regions. There are three traditional approaches for studying these correlations: the seed-based correlation technique, the

independent component analysis (ICA) technique, and graph theory. These techniques are commonly used to analyze brain connectivity. In future studies, we could also integrate these techniques to examine the correlation of the reconstructed brain images from our studies.

For the third study, the GRAPPA approach for the mSPECS-IPA-CAIPIVAT model, we presented our model in a sequential manner, where the mSPECS-IPA-CAIPIVAT, GRAPPA, and mSPECS-CAIPIVAT models need to be applied in order. However, to improve the methodology of the third study, a design matrix incorporating all voxel aliasing information needs to be considered. Moreover, similar to the first two projects, we could also incorporate the orthogonal contrast experiment design method to address the issue of aliased slices with an odd number and to investigate the correlation between different regions of the reconstructed brain image.

BIBLIOGRAPHY

- Barth, M., Breuer, F., Koopmans, P. J., Norris, D. G., and Poser, B. A. (2016). Simultaneous multislice (sms) imaging techniques. *Magnetic resonance in medicine*, 75(1):63–81.
- Breuer, F. A., Blaimer, M., Heidemann, R. M., Mueller, M. F., Griswold, M. A., and Jakob, P. M. (2005). Controlled aliasing in parallel imaging results in higher acceleration (caipirinha) for multi-slice imaging. *Magnetic Resonance in Medicine: An Official Journal of the International Society for Magnetic Resonance in Medicine*, 53(3):684–691.
- Cho, Z., Kim, D., and Kim, Y. (1988). Total inhomogeneity correction including chemical shifts and susceptibility by view angle tilting. *Medical physics*, 15(1):7–11.
- Feinberg, D. A., Hale, J. D., Watts, J. C., Kaufman, L., and Mark, A. (1986). Halving mr imaging time by conjugation: demonstration at 3.5 kg. *Radiology*, 161(2):527–531.
- Glover, G. H. (2011). Overview of functional magnetic resonance imaging. *Neurosurgery Clinics of North America*, 22(2):133.
- Griswold, M. A., Jakob, P. M., Heidemann, R. M., Nittka, M., Jellus, V., Wang, J., Kiefer, B., and Haase, A. (2002). Generalized autocalibrating partially parallel acquisitions (grappa). *Magnetic Resonance in Medicine: An Official Journal of the International Society for Magnetic Resonance in Medicine*, 47(6):1202–1210.
- Hyde, J. S., Jesmanowicz, A., Froncisz, W., Bruce Kneeland, J., Grist, T. M., and Campagna, N. F. (1986). Parallel image acquisition from noninteracting local coils. *Journal of Magnetic Resonance (1969)*, 70(3):512–517.

- Jesmanowicz, A., Nencka, A. S., Li, S.-J., and Hyde, J. S. (2011). Two-axis acceleration of functional connectivity magnetic resonance imaging by parallel excitation of phase-tagged slices and half k-space acceleration. *Brain Connectivity*, 1(1):81–90.
- Jungmann, P. M., Ganter, C., Schaeffeler, C. J., Bauer, J. S., Baum, T., Meier, R., Nittka, M., Pohlig, F., Rechl, H., von Eisenhart-Rothe, R., et al. (2015). View-angle tilting and slice-encoding metal artifact correction for artifact reduction in mri: experimental sequence optimization for orthopaedic tumor endoprotheses and clinical application. *PLoS One*, 10(4):e0124922.
- Kim, M.-O., Hong, T., and Kim, D.-H. (2016). Multislice caipirinha using view angle tilting technique (caipivat). *Tomography*, 2(1):43.
- Kim, M.-O., Zho, S.-Y., and Kim, D.-H. (2012). 3d imaging using magnetic resonance tomosynthesis (mrt) technique. *Medical physics*, 39(8):4733–4741.
- Kociuba, M. C. (2016). A fourier description of covariance, and separation of simultaneously encoded slices with in-plane acceleration in fmri.
- Kornak, J., Boylan, R., Young, K., Wolf, A., Cobigo, Y., and Rosen, H. (2020). Bayesian image analysis in fourier space using data-driven priors (dd-bifs). In *Information Processing and Management of Uncertainty in Knowledge-Based Systems: 18th International Conference, IPMU 2020, Lisbon, Portugal, June 15–19, 2020, Proceedings, Part III 18*, pages 380–390. Springer.
- Kornak, J., Young, K., Schuff, N., Du, A., Maudsley, A. A., and Weiner, M. W. (2010). K-bayes reconstruction for perfusion mri i: Concepts and application. *Journal of digital imaging*, 23:277–286.
- Lindquist, M. A., Zhang, C.-H., Glover, G., and Shepp, L. (2008). Rapid three-dimensional functional magnetic resonance imaging of the initial negative bold response. *Journal of Magnetic Resonance*, 191(1):100–111.

- Mansfield, P. (1977). Multi-planar image formation using nmr spin echoes. *Journal of Physics C: Solid State Physics*, 10(3):L55.
- Nencka, A. S. and Jesmanowicz, A. (2013). Moving window auto-calibrated multiband imaging for minimized residual correlation. In *ISMRM Workshop on Data Sampling and Image Reconstruction*, page 11, Sedona, AZ.
- Noll, D. C., Nishimura, D. G., and Macovski, A. (1991). Homodyne detection in magnetic resonance imaging. *IEEE transactions on medical imaging*, 10(2):154–163.
- Ogawa, S., Lee, T.-M., Kay, A. R., and Tank, D. W. (1990). Brain magnetic resonance imaging with contrast dependent on blood oxygenation. *proceedings of the National Academy of Sciences*, 87(24):9868–9872.
- Poustchi-Amin, M., Mirowitz, S. A., Brown, J. J., McKinstry, R. C., and Li, T. (2001). Principles and applications of echo-planar imaging: a review for the general radiologist. *Radiographics*, 21(3):767–779.
- Preibisch, C., Castrillón G, J. G., Bührer, M., and Riedl, V. (2015). Evaluation of multiband epi acquisitions for resting state fmri. *PloS one*, 10(9):e0136961.
- Pruessmann, K. P. (2004). Parallel imaging at high field strength: synergies and joint potential. *Topics in Magnetic Resonance Imaging*, 15(4):237–244.
- Pruessmann, K. P., Weiger, M., Scheidegger, M. B., and Boesiger, P. (1999). Sense: sensitivity encoding for fast mri. *Magnetic Resonance in Medicine: An Official Journal of the International Society for Magnetic Resonance in Medicine*, 42(5):952–962.
- Risk, B. B., Murden, R. J., Wu, J., Nebel, M. B., Venkataraman, A., Zhang, Z., and Qiu, D. (2021). Which multiband factor should you choose for your resting-state fmri study? *NeuroImage*, 234:117965.

- Rowe, D. B. and Logan, B. R. (2004). A complex way to compute fmri activation. *Neuroimage*, 23(3):1078–1092.
- Rowe, D. B., Nencka, A. S., Jesmanowicz, A., and Hyde, J. S. (2013). Separation of two simultaneously encoded slices with a single coil. In *Proc Intl Soc Magn Reson Med*, volume 21, page 0123.
- Rzedzian, R., Mansfield, P., Doyle, M., Guilfoyle, D., Chapman, B., Coupland, R., Chrispin, A., and Small, P. (1983). Real-time nuclear magnetic resonance clinical imaging in paediatrics. *The Lancet*, 322(8362):1281–1282.
- Setsompop, K., Gagoski, B. A., Polimeni, J. R., Witzel, T., Wedeen, V. J., and Wald, L. L. (2012). Blipped-controlled aliasing in parallel imaging for simultaneous multislice echo planar imaging with reduced g-factor penalty. *Magnetic resonance in medicine*, 67(5):1210–1224.
- Sodickson, D. K. and Manning, W. J. (1997). Simultaneous acquisition of spatial harmonics (smash): fast imaging with radiofrequency coil arrays. *Magnetic resonance in medicine*, 38(4):591–603.
- Souza, S., Szumowski, J., Dumoulin, C., Plewes, D., and Glover, G. (1988). Sima: simultaneous multislice acquisition of mr images by hadamard-encoded excitation. *J Comput Assist Tomogr*, 12(6):1026–1030.
- Stehling, M. K., Turner, R., and Mansfield, P. (1991). Echo-planar imaging: magnetic resonance imaging in a fraction of a second. *Science*, 254(5028):43–50.
- Welvaert, M. and Rosseel, Y. (2013). On the definition of signal-to-noise ratio and contrast-to-noise ratio for fmri data. *PloS one*, 8(11):e77089.